FEMTO AND PICOSECOND SPIN DYNAMICS OF LOW DIMENSIONAL MAGNETIC STRUCTURES

Thesis submitted for the degree of

Doctor of Philosophy (Science)

In

Physics (Experimental)

By

Koustuv Dutta

Department of Physics

University of Calcutta

2023

Dedicated to my mother...

Abstract

Ultrafast spin dynamics has emerged as one of the most important branches of modern nanomagnetism and has attracted huge attention for its tremendous application potential in energy-efficient information processing, high-density data storage and neuromorphic computing technologies. This doctoral thesis investigates spin dynamics ranging from nanosecond to femtosecond timescale in nano-patterned magnetic structures and thin film heterostructures. The role of external control parameters such as strength and orientation of applied magnetic field as well as the internal spin configuration of nanostructure and heterostructure interfaces has been extensively studied in modulating the ultrafast spin dynamics. A range of techniques such as scanning electron microscopy (SEM), atomic force microscopy (AFM), reflection high energy electron diffraction (RHEED), X-ray diffraction (XRD), X-ray reflectivity (XRR), vibrating sample magnetometry (VSM) etc. have been exploited to study the structural properties, surface topography and static magnetic properties of the structures under investigations. The experimental investigations of spin dynamics have been carried out employing a custom-built time-resolved magneto-optical Kerr effect (TRMOKE) magnetometer. The experimental results have been analysed by using various analytical models and micromagnetic simulations for in-depth insight.

The precessional magnetization dynamics of diamond-shaped permalloy ($Ni_{80}Fe_{20}$) antidot lattice with different configurations have been studied with the variation of magnitude and orientation of the applied magnetic field. The spin-wave spectra demonstrated rich variation with the variation in the strength of the applied magnetic field. The variation of the spin-wave spectra were analysed with the help of harmonic functions to reveal the nature of the overall dynamic configurational anisotropy. The nature and origin of the spin-wave modes have been underpinned using various micromagnetic simulations. The precessional magnetization dynamics in the nanosecond regime have also been exploited to investigate the spin pumping phenomenon at the technologically important Heusler compound and platinum interface via measuring the modulation of damping as harnessing pure spin current is crucial in ferromagnet/nonmagnet heterostructures. In this study, it has been demonstrated that a suitable heterostructure interface with a cobalt-based Heusler compound ($Co_2Fe_{0.4}Mn_{0.6}Si$) and platinum, a heavy metal, can be efficient to reduce spin current absorption at the interface and other mechanisms such as two-magnon scattering and to enhance spin current transport across the interface thereby achieving a giant value of interfacial spin transparency. We have then

explored the laser-induced ultrafast demagnetization in $Co_2Fe_{0.4}Mn_{0.6}Si$/Pt heterostructure. Interestingly, we have observed strong modulation of ultrafast demagnetization time with the ferromagnetic layer thickness. This has also been analysed using microscopic three-temperature modelling. An inverse relation between the ultrafast demagnetization time and the effective Gilbert damping has been observed experimentally. A significant enhancement of the speed of ultrafast demagnetization has been obtained in these heterostructures and has been attributed to the additional channel of spin current transport across the interface under the action of strong spin chemical potential. The findings presented in this thesis on precessional dynamics and ultrafast demagnetization contribute to the fundamental scientific understanding imperative for technological implementation in energy-efficient device applications.

List of Publications

Included in the thesis:

1. *"Dynamic Configurational Anisotropy in $Ni_{80}Fe_{20}$ Antidot Lattice with Complex Geometry"* **Koustuv Dutta**, Anulekha De, Sucheta Mondal, Saswati Barman, Yoshichika Otani and Anjan Barman; *Journal of Alloys and Compounds* **884**, 161105 (2021)**.**

2. *"All-Optical Detection of Spin Pumping and Giant Interfacial Spin Transparency in $Co_2Fe_{0.4}Mn_{0.6}Si$/Pt Heterostructure"* **Koustuv Dutta**, Surya N. Panda, Takeshi Seki, Santanu Pan, Koki Takanashi, and Anjan Barman; *Advanced Quantum Technologies*, **5**, 2200033 (2022).

3. *"Controlled Evolution of Ultrafast Demagnetization in Heusler Compound and Heavy Metal Interface"* **Koustuv Dutta** *et al*. (Manuscript under preparation)

Not Included in the thesis:

4. *"Hybrid Magnetodynamical Modes in a Single Magnetostrictive Nanomagnet on a Piezoelectric Substrate Arising from Magnetoelastic Modulation of Precessional Dynamics".* Sucheta Mondal, Md Ahsanul Abeed, **Koustuv Dutta**, Anulekha De, Sourav Sahoo, Anjan Barman and Supriyo Bandyopadhyay; *ACS Appl. Mater. Interfaces* **10**, 43970 (2018).

5. *"Observation of Angle Dependent Mode Conversion and Mode Hopping in 2D Annular Antidot Lattice"*. Nikita Porwal, Anulekha De, Sucheta Mondal, **Koustuv Dutta**, Samiran Choudhury, Jaivardhan Sinha, Anjan Barman and P K Datta; *Scientific Reports* **9**, 12138 (2019).

6. *"Observation of Spectral Narrowing and Mode Conversion in Two-dimensional Binary Magnonic Crystal".* Nikita Porwal, **Koustuv Dutta**, Sucheta Mondal, Samiran Choudhury, Jaivardhan Sinha, Anjan Barman and P. K. Datta; *Journal of Magnetism & Magnetic Materials* **501**, 166378 (2020).

7. *"Extreme Subwavelength Magnetoelastic Electromagnetic Antenna Implemented with Multiferroic Nanomagnets".* Justine Lynn Drobitch, Anulekha De, **Koustuv Dutta**, Pratap

Kumar Pal, Arundhati Adhikari, Anjan Barman, and Supriyo Bandyopadhyay; *Advanced Materials Technologies*, **5**, 2000316 (2020).

8. *"Magnonic Crystals with Complex Geometry"*. Anulekha De, **Koustuv Dutta**, Sucheta Mondal, Saswati Barman, Yoshichika Otani and Anjan Barman; *Physical Review B* **103**, 064402 (2021).

9. *"Thickness Dependent Reconfigurable Spin-Wave Dynamics in $Ni_{80}Fe_{20}$ Nanostripe Arrays"*. Pratap Kumar Pal, Sourav Sahoo, **Koustuv Dutta**, Saswati Barman, Yoshichika Otani and Anjan Barman; *Advanced Materials Interfaces*, **9**,2201333 (2022).

10. "*All-optical Study of Spin-Wave Dynamics of Slotted-Nanocross Lattice"*. Nikita Porwal, Koustuv Dutta, Sucheta Mondal, Samiran Choudhury, Jaivardhan Sinha, Anjan Barman and P. K. Datta; (manuscript under preparation)

Acknowledgements

Finally, my doctoral journey of more than five years comes to its destination. I have been fortunate enough to receive support and encouragement from many people during the long path. First and foremost, I would like to take this opportunity to express my deepest gratitude to my supervisor Prof. (Dr.) Anjan Barman for giving me an opportunity to work in his world-class laboratory as a part of his esteemed research group and for guiding me throughout this academic journey. I greatly acknowledge his guidance in developing a scientific temperament in me including planning and conducting challenging experiments, rigorous analysis of acquired data and discussing the findings in a simple yet formal way. His tireless efforts towards maintaining state-of-the-art research facilities, meticulous attitude while analyzing and communicating the research outputs and amazing multitasking ability inspired me profoundly.

I would like to extend my sincere thanks to our collaborators Prof. Yoshichika Otani (RIKEN, Japan), Dr. Takeshi Seki, Prof. Koki Takanashi (Tohoku University, Japan), Dr. P. K. Dutta (IIT Kgp) for sending us interesting samples to explore exciting spin dynamics. It was an amazing and enriching experience to work with Prof. Supriyo Bandyopadhyay (Virginia Commonwealth University, USA). I am also grateful to Dr. Saswati Barman for her support in LLG micromagnetic simulator. My special thanks to Dr. Jaivardhan Sinha (SRMIST, Chennai) for sharing kind pieces of advice and valuable insights during the initial days of the doctoral journey. I am extremely thankful to all of our present and past group members. I received the opportunity to actively work with some of my amazing seniors (Dr. Sucheta Mondal, Dr. Anulekha De and Dr. Sourav Sahoo) and learned various things from them starting from rigorous optical alignment procedures to micromagnetic simulations. I also convey thanks to my other senior colleagues Dr. Chandrima Banerjee, Dr. Samiran Chaudhury, Dr. Santanu Pan, Dr. Avinash Kr. Chaurasia, Dr. Kartik Adhikari, Dr. Arpan Bhattacharya and Dr. Ajit Sahoo for their help, suggestions and valuable discussions. I would like to acknowledge Dr. Dheeraj Kumar for the development of the MATLAB-based Dotmag codes. I also thank my juniors: Mr. Pratap Kr. Pal, Ms. Sreya Pal, Ms. Soma Dutta, Ms. Suchetana Mukhopadhyay, Mr. Chandan Kumar and Mr. Bikram Baghira for maintaining a friendly lab environment. I am especially thankful for sharing the same timeline with my amazing batchmates: Mr. Surya Narayan Panda, Ms. Arundhati Adhikari, Mr. Amrit Kr. Mondal,Mr. Sudip Mazumder and Mr. Sayantan Adak. Apart from sharing lab space, working together on projects and having

numerous professional discussions, we also shared some joyful moments. I had the opportunity to discuss many academic or non-academic issues with them in a very healthy and friendly atmosphere.

I wish to take the opportunity to convey my sincere thanks to the Department of Science & Technology, Govt. of India for supporting my doctoral journey through INSPIRE fellowship and also for providing me with an opportunity to participate in the prestigious 13th HOPE meeting. I thank S N Bose National Centre for Basic Sciences for providing great research facilities and financial support to attend various national and international conferences. I also acknowledge the academic section, accounts section and technical cell staff for their assistance.

I convey my heartfelt gratitude to all the colleagues who served as an integral part of the SNB Musical Band (formerly, SNB Khaja Band) for being exceedingly supportive to me. I am extremely grateful to Purushottam for encouraging me to perform on the stage for the first time and to Sarwar Hossain (Goba Da) for introducing me to the band. I can never thank enough the Covid19 volunteers who immensely helped me during my quarantine days. I am also thankful to the cooking, cleaning and gardening staff members who not only ensured a beautiful campus environment but also made our day-to-day life easier.

I would like to extend my gratitude towards my family and friends who provided me with a great support system. I could not have undertaken this journey without the unconditional love and sacrifices of my mother, Mrs. Mahamaya Dutta. She always supported my career decisions despite all adversities. I convey my deepest gratitude and sincere respect to her. I also express my gratitude to my maternal uncles, Mr. Sambhunath Das and Mr. Nayan Ranjan Das for their support and genuine encouragement. I also received lots of love and care from my brothers and sister, Koushik, Kalpita and Somtirtha. Besides my family, many of my close friends were strongly supportive during this journey. I express my sincere thanks to Sayandip, Debjyoti, Debyani, Sayan and Abyaya. I will be grateful forever for being able to know some awesome people here as well with perfect blends of sharp minds and kind hearts and will always cherish my friendship with Sayantan, Arundhati, Pratap and Subhajit. Last but not the least, I am greatly indebted to my school teachers and professors during my graduation and post-graduation studies (Mr. Swarup Das, Mr. Utpal Kanti Paul, Mr. Satyabrata Das, Dr. Achintya Kr. Chatterjee, Dr. Uttam Kr. Sarkar, Dr. Muktish Acharyya and Dr. Rabindranath Gayen) who inspired me to become an avid learner of physics and moreover, a good human being.

Koustuv Dutta.
S N Bose National Centre for Basic Sciences,
Salt Lake, Kolkata 700106,
India.

List of Abbreviations

AFM: Atomic force microscope

AHE: Anomalous Hall effect

AOS: All optical switching

AO-HDS: All optical helicity dependent switching

BBO: Barium Beta-borate

BLS: Brillouin light scattering

CPA: Chirped pulse amplification

CW: Continuous wave

DC: Direct current

DE: Damon–Eshbach

DMI: Dzyaloshinskii Moriya interaction

DPSS: Diode pumped solid state

DW: Domain wall

EBL: Electron beam lithography

EDX: Energy dispersive X-ray spectroscopy

FDM: Finite difference method

FEM: Finite element method

FM: Ferromagnetic

FMR: Ferromagnetic resonance

fs: Femtosecond

FWHM: Full width at half maxima

GMR: Giant magnetoresistance

GVD: Group velocity dispersion

HAMR: Heat assisted magnetic recording

HDD: Hard disc drive

HM: Heavy metal

IR: Infra-red

ISHE: Inverse spin Hall effect

LBO: Lithium tri-Borate

LCP: Left circularly polarized

LLG: Landau-Lifshitz-Gilbert

MC: Magnonic crystal

MFM: Magnetic force microscope

MO: Microscope objective

MOD: Modulation of damping

MOKE: Magneto-optical Kerr effect

MRAM: Magnetoresistive random access memory

MSBVW: Magnetostatic backward volume wave

MSFVM: Magnetostatic forward volume mode

MSSW: Magnetostatic surface wave

MTJ: Magnetic tunnel junction

NA: Numerical aperture

NM: Nonmagnetic

OBD: Optical bridge detector

OISTR: Optical inter-site spin transfer

OOMMF: Object oriented micromagnetic framework

PBS: Polarizing beam splitter

ps: Picosecond

PSSW: Perpendicular standing spin waves

RCP: Right circularly polarized

rf : Radio frequency

RGA: Regenerative amplifier

RR: Retro-reflector

RT: Room temperature

SEM: Scanning electron microscope

SDG: Synchronized delay generator

SHA: Spin Hall angle

SHE: Spin Hall effect

SHG: Second harmonic generation

SHM: Spin Hall magnetoresistance

SML: Spin memory loss

SOC: Spin orbit coupling

ST_FMR: Spin torque ferromagnetic resonance

STNO: Spin-torque nano oscillator

STT: Spin transfer torque

SW: Spin wave

TMR: Tunnel magnetoresistance

TMS: Two magnon scattering

TR-MOKE: Time-resolved magneto-optical Kerr effect

TEM: Transmission electron microscope

UV: Ultraviolet

VSM: Vibrating sample magnetometer

VPUF: Verdi pumped ultrafast laser

XRD: X-ray diffraction

XRR: X-ray reflectivity

Contents

List of Figures

Chapter 1
1. Introduction

Magnetism, despite being one of the oldest branches of science known to humanity, has never really ceased to be amazing. Although phenomenal works by Curie(1985), and Langevin (1905)[1] followed by mean field theoretical approach by Weiss (1906)[2] provided the magnetism community with a solid classical backbone, the first connection to its quantum mechanical origin was established in 1925 when Uhlenbeck and Goudsmit proposed the idea of spin angular momentum of electron[3]. Very soon, Bloch put forwarded the concept of spin-waves (1930)[4] and Landau and Lifshitz developed the semi-classical governing equation of spin precession (1935)[5] later modified by Gilbert (1955)[6] to form the Landau-Lifshitz-Gilbert (LLG) equation. The potential of this additional degree of freedom was first unlocked by the discovery of Giant Magnetoresistance (GMR) much later (1988)[7] which gave birth to a novel branch of science and technology, known as "spintronics"[8] today.

The discovery of GMR led to a paradigm shift in the conventional electronics and information processing industry. Prior to this, conventional electronics evolved a lot from using valve-based larger circuit elements to transforming completely into transistor-based circuitry. The rapid progress and praiseworthy success enjoyed by transistor-based electronics till today mostly came from the celebrated Moore's law[9] which predicted that the number of transistors integrated within a single chip will become double every two years. The tremendous downscaling of the circuit components as predicted by Moore continued over several decades[10] facilitated by the advent of high-end micro- and nanofabrication techniques making affordable high-density logic and memory devices a feasible reality.

This exponential growth in charge-based electronics, despite being celebrated for years, suffers from several physical and technological bottlenecks at the current time[11]. Considering the high-frequency switching of the bits, heat management has been a serious challenge for the high-density chips as the contemporary integrated transistor scaling has nearly approached the atomic dimensions[12]. In addition to that, the next-generation worldwide developments in artificial intelligence, cloud computing and other data-driven emerging services require a tremendous amount of energy to store and operate with the exponentially increasing data per capita. All these situations strongly suggest that a solid technology which may provide logic

and high-density storage solutions with energy efficiency is the need of the hour.

Under this circumstance, spintronics can be regarded as one of the most promising branches to look forward to. Unlike conventional electronics, here a single electron might be able to serve as the smallest unit of data storage with its spin up and down states representing two bits, 1 and 0. This indicates an enormous possibility of a complete revolution in storage technology[8]. Moreover, it can also offer energy-efficient information processing at the GHz and sub-THz regimes facilitated with much smaller on-chip integration[13]. This might greatly contribute to various other emerging technologies such as quantum computation and information processing through artificial synaptic networks as well [14-16].

However, the realization of such advanced technological developments calls for an in-depth understanding of the basic scientific phenomena occurring at the edge of the length and timescales. Aiming to actively manipulate the spins inside a magnetic system, scientists have rigorously investigated various fundamental scientific aspects, which involve a thorough examination of the fundamental static and dynamic magnetic properties of the spins. A growing technological demand has motivated scientists to pursue these efforts. Additionally, numerous experimental and theoretical efforts have been made in achieving control over several spin-based phenomena in different types of low-dimensional artificial structures that can cater to the needs of next-generation spintronics devices[17].

In the following sections, we shall provide highlights of the advancements in the spin dynamics in various low-dimensional magnetic structures that have inspired us to formulate the research hypothesis and driven us to execute the research works under this thesis.

1.1 Magnetic Nanostructures and Magnonics

The scientific community has been exploring new paradigms of patterning materials into nanoscale due to the desire to create miniaturized and energy-efficient devices[18]. The emergence of state-of-the-art nanofabrication facilities motivated researchers to test new horizons of physics in the reduced dimensionalities. Research in the past few decades has proved that artificially patterned magnetic nanostructures can cope with the requirement of high-density storage media [17,19]. The creation of artificial nanostructures and metamaterials, which are typically absent from nature is an intriguing idea as they can offer several novel functionalities in comparison to their bulk counterparts. Magnetic materials may be patterned

in different ways forming nanostripe, nanodot, antidot structure, nanoring etc[20]. These types of structures can be arranged in one, two and even three-dimensional periodic arrays as well. These kinds of artificially patterned periodic structures are called magnonic crystals (MCs)[21] in analogy to their photonic[22] and phononic[23,24] counterparts. MCs serve as the basic building block for the understanding of a span of scientific phenomena dealing with nanomagnetism and spin-wave manipulation at the nanoscale[25]. Nevertheless, in the current research much attention is being paid to the range of potential spintronic applications[26] that periodic magnetic nanostructures and MCs may offer, including bit-patterned magnetic storage media, spin Hall and spin torque nano-oscillators (STNO), reconfigurable waveguides for low-energy signal transmission etc. Such periodic nanostructures can also play a significant role in emerging technologies like neuromorphic[16] and quantum computing as they demonstrated their prospective applications as spin-wave-based transisitor[27], filter[28], directional coupler, splitter[29], multiplexers [30], demultiplexer[31], phase shifter[32], interferometers[33] and many other logic processing elements[34]. In addition, MCs have outperformed electromagnetic wave-based devices in the nanomagnetism family in terms of their high speed of data processing at a much lower energy cost. Furthermore, because of the easier on-chip integration possibility, they are strong contenders for spin-wave based on chip communication devices in the GHz and sub-THz regime.

The tremendous application potential has upsurged a flurry of research on the quasistatic and dynamic magnetic properties of nanostructures[35]. Modification of the magnetic potential landscape in one dimension has initially been studied mostly with nanostripes[36], nanowires [37] and waveguide[38] like structures revealing interesting band structure modification. A further extension of the dimension provided the opportunity to study nanodot[39], antidot[40], nanoring[41], bi-component MCs[42-44], artificial spin-ice[45,46] etc. which showed much-improved reconfigurability of the magnonic band structure[47,48]. It has also been revealed that bias field strength and orientation[49] as well as the geometric configuration of the MCs including shape[50], size[39], and periodic symmetry[51-53] can be altered to achieve efficient band tunability[54] leading to tailored spin-wave dynamics. Recent advances in this area have successfully amalgamated a span of fascinating quantum mechanical effects such as spin-orbit coupling (SOC) [55], spin current[56], Dzyaloshinskii-Moriya interaction[57], topological effects[58-60] etc. Moreover, the co-existence and complex interaction between magnons and other forms of physical excitations such as phonons[61], polarons[62] and photons[63,64] have been studied extensively in recent times that has given rise to the field of hybrid

magnonics[65,66]. Out of various types of MCs, antidot lattices (ADLs) can be regarded as one of the best classes of structure as they offer faster spin-wave propagation under strong dipole-exchange control and a steeper magnon dispersion[51]. In addition, miniaturization in ADLs is not limited by the superparamagnetic limit, unlike its dot counterparts. In recent times, complex ADLs have attracted a lot of attention[67-69] for richer spin-wave dynamics and short wavelength applications[70]. However, to achieve a better control over the spin-wave propagation through such media which could realize a logic application in future, an in-depth systematic understanding of dynamic configurational anisotropy is imperative for an ADL with geometrical complexity with insight to its quasistatic internal magnetic field landscape. Although MCs have been extensively studied using frequency domain electrical techniques like VNA-FMR[71] and directly in the wave vector domain employing Brillouin light scattering (BLS)[72], direct determination of spin-wave spectra at the time domain provides much reliable information about the configurational anisotropy. Additionally, local measurement of magnetization dynamics with higher spatio-temporal resolution can be obtained from time-resolved magneto-optical Kerr effect (TRMOKE)[73] technique which will be implemented in the present works.

1.2 Importance of Ferromagnetic/Nonmagnetic Thin Film Heterostructures

Contemporary spintronic memory architectures are primarily based on magnetoresistive properties of ferromagnetic/nonmagnetic (FM/NM) heterostructures. The ever-increasing need for larger and faster storage architecture forced the then-existing technology to evolve at a rapid pace. As already discussed, the discovery of GMR and tunnel magnetoresistance (TMR)[7,74] and subsequent research focusing on industrial implementation of these novel properties of the FM/NM/FM heterostructures[75,76] has made the journey of the hard disc from a few kB/inch^2 to TB/inch^2 a feasible reality[77]. Below we discuss the importance of such heterostructures both from the technological and fundamental points of view.

1.2.1 FM/NM Heterostructure in MRAM

To comprehend the technological importance of FM/NM heterostructures, it is imperative to understand the unit cell memory structure of an MRAM[78]. An MRAM unit cell usually contains a magnetic tunnel junction (MTJ)[79] which is manipulated in real-time to carry out the read-write process of binary digital data. It is a bistable magnetic structure consisting of two magnetic thin film layers separated by a thin spacer layer. These two layers are known as

the hard (fixed) layer and soft (free) layer depending upon the strength of their magnetic anisotropy. Because of the elliptical shape of the layers, only parallel and anti-parallel orientations are possible between these two magnetic layers producing low and high resistive states of the structure representing the bit as 0 and 1. These resistances are measured to 'read' the binary bit from the unit cell of MRAM. On the other hand, MTJ is also a classic device for spin-charge conversion. During the writing process, the spin-orbit torque (SOT) or spin transfer torque (STT) may be employed to alter the magnetization of the soft layer to encode the desired bit. For SOT-MRAM, a current is injected through another non-magnetic layer which is in contact with the soft layer whereas the current is passed through the MTJ cell of STT-MRAM during the writing process. Therefore, MTJ can serve as an analogue of the FET[80]. However, the advantage of MRAM cells over FET is that the resistance state in MTJs is non-volatile in nature. Nevertheless, extensive research in the FM/NM interface is required to reduce the switching current (write current) and improve other parameters for enhanced device efficiency.

1.2.2 Multilayered Heterostructure with PMA

To fulfil the increasing demands of a denser storage media, the MRAM unit cells are further miniaturized. When the cells attempted to reduce to sub-100 nm dimension, they approached the superparamagnetic limit and struggled significantly in retaining the thermal stability against the thermal fluctuations at room temperature[81]. To overcome the limitation, perpendicular magnetic recording media is put forward as opposed to longitudinal recording systems typically used in MTJ structure[82,83]. In this type, the heterostructure is constructed so as to incorporate a strong perpendicular magnetic anisotropy (PMA)[84]. SOC plays a vital role in determining the PMA properties of such structures. Additionally, it has been found that PMA strength heavily depends on both the thickness of the constituting FM and NM layers as well as the growth conditions and interface properties[85,86]. This establishes the importance of a thorough investigation of FM/NM structures with a special emphasis on the effect of their interface on the spin current transport across the structure.

1.2.3 Heterostructures in Analog Microwave Devices

FM/NM based heterostructures are strong contenders too for spin-torque nano oscillators (STNO)[87] and various other radio-frequency applications such as signal mixers, amplifiers[88,89], nanoscale signal transmitters[90] and tunable microwave resonators[91]. In contrary to the memory devices, FM/NM structures are employed here as analog applications. For the MTJ structure to be used as STNO, it is driven with a constant current source which

generates large spin angular momentum. The spin transfer torque induces precession of spins in the soft FM layer resulting in a time-varying magnetoresistance of the whole structure. This produces a time-varying voltage and an oscillating electric field across the device causing microwave emission from it[90]. Researches have shown that this principle may be employed for the microwave-assisted magnetic recording process, widely known as MAMR and a reliable synchronized coupling[92,93] between such microwave emitters can find potential implementations in neuromorphic computing[94].

1.3 Scope of Fundamental and Applied Research

The ever-growing demands of FM/NM heterostructures in both the existing and emerging technologies make the research on novel fundamental properties and spintronic application possibilities crucial. Here, we will discuss primarily two aspects of fundamental and applied research in the following segments: i) the generation and manipulation of pure spin current and ii) achieving superior control over the ultrafast spin manipulation in such heterostructures. Both of these fields are attractive as the growing contemporary research playgrounds and are known for their laser-sharp focus on the high speed and energy efficiency of the spin dynamic processes.

1.3.1 Harnessing Pure Spin Current with curated FM/NM Interfaces

In addition to the enormous technological application potential, FM/NM based heterostructures are extremely attractive systems from a fundamental perspective as well. In presence of a suitable non-magnetic or heavy metal system adjacent to the FM layer, they offer a vast playground for a span of exotic phenomena such as spin-Hall effect (SHE)[95], inverse SHE[96], Rashba-Edelstein effect[97], interfacial Dzyaloshinskii-Moriya interaction (iDMI)[98,99], spin Seebeck effect[100], spin Nernst effect[101], non-local injection of spin etc. The most intriguing part is, all of these phenomena can be utilized to efficiently generate and control the pure spin current. As the name suggests, pure spin current[102] refers to the flow of spin angular momentum in a system without a net charge current flow and associated energy loss caused by Joule heating[103]. As the prime focus of modern spintronics has been the energy-efficient operation of high-speed devices, the practical realization of such goals relies heavily on active manipulation over pure spin current.

In an FM/NM heterostructure, spin-current-induced magnetization precession was known for a long[104]. However, in 2002, Tserkovnyak *et al.*[105] proposed a physical mechanism which is quite inverse in nature. They showed that in an FM/NM/FM ‘spin-valve’ structure,

precessing magnetization in either of the FM layer can inject a spin current into the adjacent NM layer under the difference of spin-chemical potential and as a consequence of the non-local flow of spins, the precessing magnetic moments experience additional extrinsic damping[105,106]. This mechanism is known as spin pumping and it is one of the most popular and widely accepted mechanisms to harness pure spin current in FM/NM structures[103].

Several *3d* ferromagnetic materials like Fe, Ni, Co and their alloys (such as $Ni_{80}Fe_{20}$, CoFeB etc.)[107,108] have been chosen along with heavy metals[109,110], semiconductors[111], 2D layered materials[112], oxide insulator materials[113], topological insulators[114] etc. as the adjacent NM layer to investigate the spin pumping in FM/NM heterostructure. Among the various NM materials, heavy metals are the natural choice as because of their strong SOC strength they are able to generate very large spin currents. However, the choice of FM material becomes non-trivial and a large number of factors need to be taken care of while constructing an FM/HM interface[56,115]. Co-based Heusler alloys are one of the best classes of materials that can be chosen for such an interface[116]. They are half-metallic materials with high spin polarization[117,118], stable spin-split band structure and low intrinsic Gilbert damping and thus find considerable application potential in TMR-based devices and STNO[119,120] with low switching current. Therefore, a Heusler compound/HM interface is an attractive system both from fundamental and application perspectives[121] and calls for an in-depth study regarding the generation, manipulation and absorption of pure spin current for a comprehensive understanding. One of the key parameters that significantly controls the efficient spin current transport in an FM/HM heterostructure is interfacial spin transparency[122]. At the interface, the spin transport may face hindrance due to the presence of defects via two-magnon scattering[123-125] or may get absorbed at the interface causing a spin memory loss[126] resulting in poor spin current transport. Additionally, the mismatch between the band structure between the two components of the heterostructure can further reduce the transport. The cumulative effects of all the controlling factors can be quantitatively measured in terms of the interfacial spin transparency[127]. This demands that rigorous efforts are essential in the careful engineering of the interface with a wise choice of materials for achieving significant control over the spin transport and enhancing its potential as a spin-orbitronic device application in future.

1.3.2 Manipulation of Magnetic Order at the Ultrafast Timescale

As a result of continuous innovation through several decades most modern-day computers are

equipped with logic processors with 2-4 GHz of clock speed. However, reaping all the benefits of such a tremendous speed has been limited by the speed of data manipulation offered by memory architectures. As already discussed, in a typical memory unit the geometric configuration coupled with energy minimization usually allows the magnetic orientation to access a bistable configuration representing two separate bits by each of the configurations[80]. However, the writing process that is storing a new bit to the unit requires a 'switching' of the state which is achieved via magnetic reversal. Therefore, it is quite evident that the speed of writing or recording in a unit cell will depend on the fundamental mechanism behind the magnetization reversal. Considerable efforts have been made to explore different mechanisms of magnetic switching such as thermally assisted switching[128,129] leading to HAMR[130], microwave-assisted switching (MAS)[131,132], spin-polarized current (STT) controlled switching, voltage (electric field)-controlled[133-136] and even strain-controlled switching[137]. Despite the rigorous research and optimization, the timescales associated with these processes are found to lie in the order of picoseconds to nanoseconds[138] thus creating an "ultrafast technology gap"[139] between the class of information processing and storage architectures.

This had fueled intense research to further explore different avenues to control the magnetic order which can potentially offer higher operational speed and efficiency. In this context, laser-induced ultrafast demagnetization as discovered by Beurepaire *et al.*[140] provided a novel route. As the all-optical process demonstrated a characteristic demagnetization timescale of the order of 280 fs, it attracted a lot of subsequent investigations over various classes of materials such as metals[141], semiconductors [142,143], rare earth alloys[144,145], half-metallic materials[146], 2d materials etc. devoted to controlling the speed and efficiency of the mechanism. One of the most intriguing parts of the process is that even after two decades of theoretical and experimental investigations, the fundamental physical microscopic picture of the process is still elusive. Although various possible mechanisms have been proposed mostly based on the spin-flip scattering process such as phonon-mediated scattering[147], Coulomb scattering[148], electron magnon scattering[149,150], relativistic electromagnetic process[151] etc., several literature reports also claim that the process may completely be expressed in terms of spin-dependent super-diffusive transport and thermal current transport in the FM/NM heterostructure devoid of any spin flips at all[152-154]. Thus FM/NM heterostructure may serve as one of the ideal systems to gain deeper fundamental insights as well as achieve better control over the ultrafast manipulation of magnetization. A wide range

of FM/NM heterostructures has also been investigated in recent times in all-optical techniques deriving some of the key insights about the process demonstrating the role of various control parameters such as film thickness[155], composition[156], laser fluence etc. In addition, ultrafast demagnetization can also play a significant role in the all-optical helicity-dependent switching (AO-HDS) of magnetization. This clearly suggests a huge opportunity to investigate the mechanism of this non-equilibrium femtosecond spin dynamics in the technologically important Heusler compound and heavy metal heterostructure interface in presence of a strong spin transport phenomenon facilitated by the SOC of the heavy metal.

1.4 The objective of the thesis

The sole objective of this thesis is to explore the whole range of spin dynamics ranging from the ultrafast demagnetization happening within the hundreds of femtoseconds to the precessional dynamics taking place over nanosecond timescale in different low-dimensional magnetic nanostructures and thin-film heterostructures which can be potentially advantageous in the spintronic and spin-orbitronic applications. It focuses on some exciting and long-standing problems of spintronics and magnonics. It aims to explore the role of configurational anisotropy in GHz spin-wave response from magnetic nanostructures particularly, antidot lattices favourable for their strong dipole-exchange interaction. In the case of the FM/HM type of heterostructure, it thoroughly investigates the fundamental correlation between the ultrafast demagnetization time and the effective Gilbert damping, corresponding to the ultrafast demagnetization and precessional magnetization dynamics which span over different timescales of spin dynamics. The thesis also puts rigorous efforts to elucidate the spin pumping and allied phenomena at the interface and extraction of interfacial spin transparency using an all-optical techniques which can be technologically imperative.

Therefore, the underlying scope of the doctoral work can be more specifically described as the understanding of the role of bias field orientation, complex lattice geometry, effects of film thickness, engineered interface and structural details in modulating the femtosecond to nanosecond spin dynamics for nanostructures and heterostructures of technological significance. The thesis is organized as follows: Chapter 2 provides the basic theoretical background of ultrafast magnetization dynamics with different possible underlying mechanisms. Also, it discusses various intrinsic and extrinsic origins of magnetic damping. Chapter 3 covers the detailed principles of all the experimental and numerical techniques employed for the studies presented in the thesis. The subsequent three chapters (Chapter 4, 5 and 6) covers the findings of the experimental and numerical investigations as discussed below in detail:

1.4.1 Dynamic configurational anisotropy in permalloy ($Ni_{80}Fe_{20}$) antidot lattice with complex geometry

Chapter 4 describes the investigation of precessional magnetization dynamics of $Ni_{80}Fe_{20}$ antidot lattice with geometrical complexity. The effect of configurational anisotropy on different dynamical quantities is comprehensively studied from the bias-field strength and orientation modulation of spin-wave spectra with an insight into the alteration in the spin-wave mode profile origin with the variation in magnetic field landscape.

1.4.2 All-optical detection of giant interfacial spin transparency in CFMS-Pt heterostructure

In chapter 5, we have investigated spin pumping phenomena in CFMS/Pt/Al heterostructure using all-optical excitation and detection technique. We have been able to extract giant spin transparency for this interface as a function of the spin-mixing conductance and spin diffusion length which have been calculated employing two separate theoretical models. Apart from the spin-pumping phenomenon, the role of other interface mechanisms in the modulation of Gilbert damping such as spin memory loss and two-magnon scattering have also been studied comprehensively.

1.4.3 Controlled evolution of ultrafast demagnetization in Heusler compound and heavy metal interface

Chapter 6 deals with the controlled manipulation of magnetic order in CFMS/Pt/Al heterostructure to explore the potential of ferromagnetic/heavy metal heterostructures in high-speed spintronic architectures. Here, we have demonstrated strong thickness-dependent modulation of ultrafast demagnetization time and found a strong inverse linear correlation of it with the effective Gilbert damping. The modelling of the electron and lattice temperatures along with the normalized magnetization in microscopic three-temperature framework unraveled the strong role of phonon-mediated spin-flip scattering in this process. Additionally, the role of spin-current transport via the interface in manipulating the magnetization in femtosecond timescale has been thoroughly investigated.

1.5 References

[1]P. Langevin, Ann. chim. et phys, 203 (1905).
[2]P. Weiss, Journal de Physique Théorique et Appliquée **6**, 661 (1907).
[3]G. E. Uhlenbeck and S. Goudsmit, Naturwissenschaften **13**, 953 (1925).

[4]F. Bloch, Z. Phys. **74**, 295 (1932).
[5]L. Landau and E. Lifshitz, in *Perspectives in Theoretical Physics*, edited by L. P. Pitaevski (Pergamon, Amsterdam, 1992), pp. 51.
[6]T. L. Gilbert, IEEE Trans. Magn. **40**, 3443 (2004).
[7]M. N. Baibich, J. M. Broto, A. Fert, F. N. Van Dau, F. Petroff, P. Etienne, G. Creuzet, A. Friederich, and J. Chazelas, Phys. Rev. Lett **61**, 2472 (1988).
[8]S. D. Bader and S. S. P. Parkin, Annu. Rev. Condens. Matter Phys **1**, 71 (2010).
[9]G. E. Moore, Proc. IEEE **86**, 82 (1998).
[10]R. R. Schaller, IEEE Spectrum **34**, 52 (1997).
[11]Editorial, Nat. Nanotechnol **12**, 1105 (2017).
[12]F. Peper, New Generation Computing **35**, 253 (2017).
[13]I. Žutić, J. Fabian, and S. Das Sarma, Rev. Mod. Phys **76**, 323 (2004).
[14]D. Awschalom, D. Loss, and N. Samarth, *Semiconductor spintronics and quantum computation* (Springer Science & Business Media, 2002).
[15]J. Grollier, D. Querlioz, K. Y. Camsari, K. Everschor-Sitte, S. Fukami, and M. D. Stiles, Nature Electronics **3**, 360 (2020).
[16]A. Sengupta and K. Roy, Appl. Phys. Exp. **11**, 030101 (2018).
[17]J. Puebla, J. Kim, K. Kondou, and Y. Otani, Communications Materials **1**, 24 (2020).
[18]A. Bland, J. A. C. Bland, B. Heinrich, and B. Heinrich, *Ultrathin Magnetic Structures I: An Introduction to the Electronic, Magnetic and Structural Properties* (Springer Science & Business Media, 2005), Vol. 1.
[19]C. Chappert, A. Fert, and F. N. Van Dau, Nat Mater **6**, 813 (2007).
[20]A. Barman, S. Mondal, S. Sahoo, and A. De, J Appl. Phys. **128** (2020).
[21]Y. V. Gulyaev and A. A. Nikitov, Doklady Physics **46**, 687 (2001).
[22]H. Puszkarski and M. Krawczyk, in *Solid State Phenomena* (Trans Tech Publ, 2003), pp. 125.
[23]M.-H. Lu, L. Feng, and Y.-F. Chen, Mater. Today **12**, 34 (2009).
[24]A. L. Chen, Y.-S. Wang, Y.-F. Guo, and Z.-D. Wang, Solid State Commun. **145**, 103 (2008).
[25]B. Lenk, H. Ulrichs, F. Garbs, and M. Münzenberg, Physics Reports **507**, 107 (2011).
[26]A. Hirohata, K. Yamada, Y. Nakatani, I. L. Prejbeanu, B. Dieny, P. Pirro, and B. Hillebrands, J Magn. Magn. Mater. **509**, 166711 (2020).
[27]A. V. Chumak, A. A. Serga, and B. Hillebrands, Nat. Commun. **5**, 4700 (2014).
[28]A. V. Sadovnikov, V. A. Gubanov, S. E. Sheshukova, Y. P. Sharaevskii, and S. A. Nikitov, Phys. Rev. Appl. **9**, 051002 (2018).
[29]F. Heussner, A. A. Serga, T. Brächer, B. Hillebrands, and P. Pirro, Appl. Phys. Lett. **111**, 122401 (2017).
[30]Z. Zhang *et al.*, Appl. Phys. Lett. **115**, 232402 (2019).
[31]F. Heussner *et al.*, physica status solidi (RRL) – Rapid Research Letters **14**, 1900695 (2020).
[32]M. P. Kostylev, A. A. Serga, T. Schneider, B. Leven, and B. Hillebrands, Appl. Phys. Lett. **87**, 153501 (2005).
[33]A. A. Grachev, A. V. Sadovnikov, and S. A. Nikitov, Nanomaterials **12**, 1520 (2022).
[34]T. Schneider, A. A. Serga, B. Leven, B. Hillebrands, R. L. Stamps, and M. P. Kostylev, Appl. Phys. Lett. **92**, 022505 (2008).
[35]A. Barman and J. Sinha, *Spin Dynamics and Damping in Ferromagnetic Thin Films and Nanostructures* (Springer International Publishing, 2018).
[36]M. P. Kostylev, A. A. Stashkevich, and N. A. Sergeeva, Phys. Rev. B **69**, 064408 (2004).
[37]J. D. Holmes, K. P. Johnston, R. C. Doty, and B. A. Korgel, Science **287**, 1471 (2000).
[38]A. V. Sadovnikov, A. Grachev, S. Sheshukova, Y. Sharaevsky, A. Serdobintsev, and S. Nikitov, in *2018 IEEE International Magnetics Conference (INTERMAG)*2018), pp. 1.

[39]B. Rana, S. Pal, S. Barman, Y. Fukuma, Y. Otani, and A. Barman, Appl. Phys. Exp. **4** (2011).
[40]A. De, S. Mondal, S. Sahoo, S. Barman, Y. Otani, R. K. Mitra, and A. Barman, Beilstein J. Nanotechnol. **9**, 1123 (2018).
[41]C. Banerjee, S. Saha, S. Barman, O. Rousseau, Y. Otani, and A. Barman, J Appl. Phys. **116** (2014).
[42]S. Tacchi, G. Duerr, J. W. Klos, M. Madami, S. Neusser, G. Gubbiotti, G. Carlotti, M. Krawczyk, and D. Grundler, Phys. Rev. Lett **109**, 137202 (2012).
[43]S. Choudhury, S. Saha, R. Mandal, S. Barman, Y. Otani, and A. Barman, ACS Appl. Mater. Inter. **8**, 18339 (2016).
[44]M. Krawczyk, S. Mamica, M. Mruczkiewicz, J. W. Klos, S. Tacchi, M. Madami, G. Gubbiotti, G. Duerr, and D. Grundler, J Phys. D:Appl. Phys **46**, 495003 (2013).
[45]S. H. Skjærvø, C. H. Marrows, R. L. Stamps, and L. J. Heyderman, Nature Reviews Physics **2**, 13 (2020).
[46]A. K. Chaurasiya, A. K. Mondal, J. C. Gartside, K. D. Stenning, A. Vanstone, S. Barman, W. R. Branford, and A. Barman, ACS Nano **15**, 11734 (2021).
[47]J. W. Kłos, D. Kumar, J. Romero-Vivas, H. Fangohr, M. Franchin, M. Krawczyk, and A. Barman, Phys. Rev. B **86**, 184433 (2012).
[48]S. Neusser, G. Duerr, S. Tacchi, M. Madami, M. L. Sokolovskyy, G. Gubbiotti, M. Krawczyk, and D. Grundler, Phys. Rev. B **84**, 094454 (2011).
[49]S. Choudhury, S. Majumder, S. Barman, Y. Otani, and A. Barman, Phys. Rev. Appl. **10** (2018).
[50]A. De, S. Mondal, S. Choudhury, S. Sahoo, S. Majumder, S. Barman, Y. Otani, and A. Barman, J Magn. Magn. Mater. **487** (2019).
[51]R. Mandal, S. Barman, S. Saha, Y. Otani, and A. Barman, J Appl. Phys. **118** (2015).
[52]S. Tacchi, M. Madami, G. Gubbiotti, G. Carlotti, A. O. Adeyeye, S. Neusser, B. Botters, and D. Grundler, IEEE Trans. Magn. **46**, 1440 (2010).
[53]A. Manzin and O. Bottauscio, J Phys. D:Appl. Phys **45** (2012).
[54]M. Krawczyk and D. Grundler, J Phys. Cond. Mater. **26**, 123202 (2014).
[55]F. Hellman *et al.*, Rev. Mod. Phys **89**, 025006 (2017).
[56]S. Panda, S. Mondal, J. Sinha, S. Choudhury, and A. Barman, Sci. Adv. **5**, eaav7200 (2019).
[57]V. E. Dmitrienko, E. N. Ovchinnikova, S. P. Collins, G. Nisbet, G. Beutier, Y. O. Kvashnin, V. V. Mazurenko, A. I. Lichtenstein, and M. I. Katsnelson, Nat. Phys **10**, 202 (2014).
[58]X. S. Wang, H. W. Zhang, and X. R. Wang, Phys. Rev. Appl. **9**, 024029 (2018).
[59]R. Chisnell, J. S. Helton, D. E. Freedman, D. K. Singh, R. I. Bewley, D. G. Nocera, and Y. S. Lee, Phys. Rev. Lett. **115**, 147201 (2015).
[60]K. Nakata, S. K. Kim, J. Klinovaja, and D. Loss, Phys. Rev. B **96**, 224414 (2017).
[61]C. Berk, M. Jaris, W. Yang, S. Dhuey, S. Cabrini, and H. Schmidt, Nat. Commun. **10**, 2652 (2019).
[62]F. Godejohann *et al.*, Phys. Rev. B **102**, 144438 (2020).
[63]Y. Tabuchi, S. Ishino, T. Ishikawa, R. Yamazaki, K. Usami, and Y. Nakamura, Phys. Rev. Lett **113**, 083603 (2014).
[64]Y. Tabuchi, S. Ishino, A. Noguchi, T. Ishikawa, R. Yamazaki, K. Usami, and Y. Nakamura, Science **349**, 405 (2015).
[65]Y. Li, W. Zhang, V. Tyberkevych, W.-K. Kwok, A. Hoffmann, and V. Novosad, J Appl. Phys. **128**, 130902 (2020).
[66]D. Lachance-Quirion, Y. Tabuchi, A. Gloppe, K. Usami, and Y. Nakamura, Appl. Phys. Exp. **12**, 070101 (2019).
[67]S. Choudhury, S. Barman, Y. Otani, and A. Barman, ACS Nano **11**, 8814 (2017).
[68]D. Shi, Z. Budrikis, A. Stein, S. A. Morley, P. D. Olmsted, G. Burnell, and C. H. Marrows,

Nat. Phys **14**, 309 (2018).
[69]A. De, K. Dutta, S. Mondal, S. Barman, Y. Otani, and A. Barman, Phys. Rev. B **103** (2021).
[70]C. Liu *et al.*, Nat. Commun. **9**, 738 (2018).
[71]K. Adhikari, S. Sahoo, A. K. Mondal, Y. Otani, and A. Barman, Phys. Rev. B **101** (2020).
[72]C. Banerjee, S. Choudhury, J. Sinha, and A. Barman, Phys. Rev. Appl. **8**, 014036 (2017).
[73]A. Barman, T. Kimura, Y. Otani, Y. Fukuma, K. Akahane, and S. Meguro, Rev Sci Instrum **79**, 123905 (2008).
[74]J. S. Moodera, L. R. Kinder, T. M. Wong, and R. Meservey, Phys. Rev. Lett **74**, 3273 (1995).
[75]G. Binasch, P. Grünberg, F. Saurenbach, and W. Zinn, Phys. Rev. B **39**, 4828 (1989).
[76]S. S. P. Parkin *et al.*, J Appl. Phys. **85**, 5828 (1999).
[77]J. J. M. Ruigrok, R. Coehoorn, S. R. Cumpson, and H. W. Kesteren, J Appl. Phys. **87**, 5398 (2000).
[78]S. Bhatti, R. Sbiaa, A. Hirohata, H. Ohno, S. Fukami, and S. N. Piramanayagam, Mater. Today **20**, 530 (2017).
[79]T. Miyazaki and N. Tezuka, J Magn. Magn. Mater. **139**, L231 (1995).
[80]B. Rana, A. K. Mondal, S. Bandyopadhyay, and A. Barman, Nanotechnology **33**, 062007 (2022).
[81]Y. Shiratsuchi, M. Yamamoto, Y. Endo, D. Li, and S. D. Bader, **94**, 7675 (2003).
[82]R. Sbiaa, H. Meng, and S. N. Piramanayagam, physica status solidi (RRL) – Rapid Research Letters **5**, 413 (2011).
[83]S. Kanai, M. Yamanouchi, S. Ikeda, Y. Nakatani, F. Matsukura, and H. Ohno, Appl. Phys. Lett. **101**, 122403 (2012).
[84]P. F. Carcia, A. D. Meinhaldt, and A. Suna, Appl. Phys. Lett. **47**, 178 (1985).
[85]F. J. A. den Broeder, D. Kuiper, A. P. van de Mosselaer, and W. Hoving, Phys. Rev. Lett **60**, 2769 (1988).
[86]M. Zelent, P. Gruszecki, M. Moalic, O. Hellwig, A. Barman, and M. Krawczyk, in *Solid State Phys.*, edited by R. Macedo (Academic Press, 2022), pp. 1.
[87]M. Tarequzzaman *et al.*, Communications Physics **2**, 20 (2019).
[88]E. Padrón-Hernández, A. Azevedo, and S. M. Rezende, Appl. Phys. Lett. **99**, 192511 (2011).
[89]O. Gladii *et al.*, Appl. Phys. Lett. **108**, 202407 (2016).
[90]D. Houssameddine *et al.*, Appl. Phys. Lett. **93**, 022505 (2008).
[91]H. Qin, R. B. Holländer, L. Flajšman, F. Hermann, R. Dreyer, G. Woltersdorf, and S. van Dijken, Nat. Commun. **12**, 2293 (2021).
[92]S. Sani *et al.*, Nat. Commun. **4**, 2731 (2013).
[93]S. Kaka, M. R. Pufall, W. H. Rippard, T. J. Silva, S. E. Russek, and J. A. Katine, Nature **437**, 389 (2005).
[94]J. Torrejon *et al.*, Nature **547**, 428 (2017).
[95]J. Sinova, S. O. Valenzuela, J. Wunderlich, C. H. Back, and T. Jungwirth, Rev. Mod. Phys **87**, 1213 (2015).
[96]E. Saitoh, M. Ueda, H. Miyajima, and G. Tatara, Appl. Phys. Lett. **88**, 182509 (2006).
[97]G. Dresselhaus, Phys. Rev. **100**, 580 (1955).
[98]H. Yang, A. Thiaville, S. Rohart, A. Fert, and M. Chshiev, Phys. Rev. Lett. **115**, 267210 (2015).
[99]J. Cho *et al.*, Nat. Commun. **6**, 7635 (2015).
[100]K. Uchida, S. Takahashi, K. Harii, J. Ieda, W. Koshibae, K. Ando, S. Maekawa, and E. Saitoh, Nature **455**, 778 (2008).
[101]P. Sheng, Y. Sakuraba, Y. C. Lau, S. Takahashi, S. Mitani, and M. Hayashi, Sci. Adv. **3**, e1701503 (2017).

[102]A. Hoffmann, physica status solidi c **4**, 4236 (2007).
[103]S. Maekawa, S. O. Valenzula, E. Saitoh, and T. Kimura, *Spin current* (Oxford University Press, Oxford, 2017), 2nd edn., Series on Semiconductor Science and Technology.
[104]A. D. Kent, B. Özyilmaz, and E. del Barco, Appl. Phys. Lett. **84**, 3897 (2004).
[105]Y. Tserkovnyak, A. Brataas, and G. E. Bauer, Phys. Rev. Lett **88**, 117601 (2002).
[106]Y. Tserkovnyak, A. Brataas, and G. E. W. Bauer, Phys. Rev. B **66**, 224403 (2002).
[107]E. T. Papaioannou, P. Fuhrmann, M. B. Jungfleisch, T. Brächer, P. Pirro, V. Lauer, J. Lösch, and B. Hillebrands, Appl. Phys. Lett. **103**, 162401 (2013).
[108]Z. Feng *et al.*, Phys. Rev. B **85**, 214423 (2012).
[109]K. Dolui and B. K. Nikolić, Phys. Rev. B **96**, 220403 (2017).
[110]M. Haertinger, C. H. Back, J. Lotze, M. Weiler, S. Geprägs, H. Huebl, S. T. B. Goennenwein, and G. Woltersdorf, Phys. Rev. B **92**, 054437 (2015).
[111]R. Adhikari, M. Matzer, A. T. Martín-Luengo, M. C. Scharber, and A. Bonanni, Phys. Rev. B **94**, 085205 (2016).
[112]S. N. Panda, S. Majumder, S. Choudhury, A. Bhattacharya, S. Sinha, and A. Barman, Nanoscale **13**, 13709 (2021).
[113]K. Roy, A. Mishra, P. Gupta, S. Mohanty, B. B. Singh, and S. Bedanta, J Phys. D:Appl. Phys **54**, 425001 (2021).
[114]M. Jamali *et al.*, Nano Lett. **15**, 7126 (2015).
[115]F. Hellman *et al.*, Rev. Mod. Phys **89**, 025006 (2017).
[116]S. Pan, T. Seki, K. Takanashi, and A. Barman, Phys. Rev. Appl. **7**, 064012 (2017).
[117]L. Bainsla, A. I. Mallick, A. A. Coelho, A. K. Nigam, B. S. D. C. S. Varaprasad, Y. K. Takahashi, A. Alam, K. G. Suresh, and K. Hono, J Magn. Magn. Mater. **394**, 82 (2015).
[118]I. Galanakis and P. Mavropoulos, J Phys. Condens. Mater. **19**, 315213 (2007).
[119]T. Kubota, S. Tsunegi, M. Oogane, S. Mizukami, T. Miyazaki, H. Naganuma, and Y. Ando, Appl. Phys. Lett. **94**, 122504 (2009).
[120]A. L. Kwilu, M. Oogane, H. Naganuma, M. Sahashi, and Y. Ando, J Appl. Phys. **117**, 17D140 (2015).
[121]K. Elphick, W. Frost, M. Samiepour, T. Kubota, K. Takanashi, H. Sukegawa, S. Mitani, and A. Hirohata, Sci. Technol. Adv. Mater. **22**, 235 (2021).
[122]H. Chudo, K. Ando, K. Saito, S. Okayasu, R. Haruki, Y. Sakuraba, H. Yasuoka, K. Takanashi, and E. Saitoh, J Appl. Phys. **109**, 073915 (2011).
[123]M. J. Hurben and C. E. Patton, J Appl. Phys. **83**, 4344 (1998).
[124]K. Lenz, H. Wende, W. Kuch, K. Baberschke, K. Nagy, and A. Jánossy, Phys. Rev. B **73**, 144424 (2006).
[125]P. Krivosik, N. Mo, S. Kalarickal, and C. E. Patton, J Appl. Phys. **101**, 083901 (2007).
[126]J. C. Rojas-Sanchez *et al.*, Phys. Rev. Lett **112**, 106602 (2014).
[127]W. Zhang, W. Han, X. Jiang, S.-H. Yang, and S. S. P. Parkin, Nat. Phys **11**, 496 (2015).
[128]I. L. Prejbeanu, W. Kula, K. Ounadjela, R. C. Sousa, O. Redon, B. Dieny, and J. P. Nozieres, IEEE Trans. Magn. **40**, 2625 (2004).
[129]A. Pushp, T. Phung, C. Rettner, B. P. Hughes, S.-H. Yang, and S. S. P. Parkin, Proceedings of the National Academy of Sciences **112**, 6585 (2015).
[130]R. E. Rottmayer *et al.*, IEEE Trans. Magn. **42**, 2417 (2006).
[131]H. T. Nembach, P. Martín Pimentel, S. J. Hermsdoerfer, B. Leven, B. Hillebrands, and S. O. Demokritov, Appl. Phys. Lett. **90**, 062503 (2007).
[132]T. Moriyama, R. Cao, J. Q. Xiao, J. Lu, X. R. Wang, Q. Wen, and H. W. Zhang, Appl. Phys. Lett. **90**, 152503 (2007).
[133]D. Chiba, M. Yamanouchi, F. Matsukura, and H. Ohno, Science **301**, 943 (2003).
[134]J. T. Heron *et al.*, Phys. Rev. Lett **107**, 217202 (2011).
[135]T. Maruyama *et al.*, Nat. Nanotechnol **4**, 158 (2009).

[136]N. Tiercelin, Y. Dusch, V. Preobrazhensky, and P. Pernod, J Appl. Phys. **109**, 07D726 (2011).
[137]A. K. Biswas, S. Bandyopadhyay, and J. Atulasimha, Appl. Phys. Lett. **105**, 072408 (2014).
[138]J. Matsuzaki, T. Tanaka, H. Kurisu, and S. Yamamoto, Transactions of the Materials Research Society of Japan **34**, 415 (2009).
[139]A. Kirilyuk, A. V. Kimel, and T. Rasing, Rev. Mod. Phys **82**, 2731 (2010).
[140]E. Beaurepaire, J. C. Merle, A. Daunois, and J. Y. Bigot, Phys. Rev. Lett **76**, 4250 (1996).
[141]F. Dalla Longa, J. T. Kohlhepp, W. J. M. de Jonge, and B. Koopmans, Phys. Rev. B **75** (2007).
[142]J. Wang, Ł. Cywiński, C. Sun, J. Kono, H. Munekata, and L. J. Sham, Phys. Rev. B **77**, 235308 (2008).
[143]J. Wang, I. Cotoros, K. M. Dani, X. Liu, J. K. Furdyna, and D. S. Chemla, Phys. Rev. Lett **98**, 217401 (2007).
[144]V. López-Flores, N. Bergeard, V. Halté, C. Stamm, N. Pontius, M. Hehn, E. Otero, E. Beaurepaire, and C. Boeglin, Phys. Rev. B **87**, 214412 (2013).
[145]G. Ju, J. Hohlfeld, B. Bergman, R. J. van de Veerdonk, O. N. Mryasov, J. Y. Kim, X. Wu, D. Weller, and B. Koopmans, Phys. Rev. Lett. **93**, 197403 (2004).
[146]A. Mann *et al.*, Physical Review X **2**, 041008 (2012).
[147]B. Koopmans, J. J. Ruigrok, F. D. Longa, and W. J. de Jonge, Phys. Rev. Lett. **95**, 267207 (2005).
[148]M. Krauß, T. Roth, S. Alebrand, D. Steil, M. Cinchetti, M. Aeschlimann, and H. C. Schneider, Phys. Rev. B **80**, 180407 (2009).
[149]S. Zhang and Z. Li, Phys. Rev. Lett. **93**, 127204 (2004).
[150]M. Haag, C. Illg, and M. Fähnle, Phys. Rev. B **90** (2014).
[151]J. Y. Bigot, M. Vomir, and E. Beaurepaire, Nat. Phys **5**, 515 (2009).
[152]M. Battiato, K. Carva, and P. M. Oppeneer, Phys. Rev. Lett. **105**, 027203 (2010).
[153]A. Eschenlohr *et al.*, Nat Mater **12**, 332 (2013).
[154]U. Atxitia, O. Chubykalo-Fesenko, J. Walowski, A. Mann, and M. Münzenberg, Phys. Rev. B **81** (2010).
[155]S. Pan, S. Mondal, T. Seki, K. Takanashi, and A. Barman, Phys. Rev. B **94**, 184417 (2016).
[156]S. Pan, T. Seki, K. Takanashi, and A. Barman, Phys. Rev. B **101** (2020).

Chapter 2
2. Theoretical Background

2.1 Introduction

In the initial days of magnetism, it was regarded as a separate branch of science. In 1820, the famous experiment by Oersted with a current-carrying wire and a magnetic needle established that magnetism can hardly be separated from electricity. Subsequently, the development of Heisenberg's exchange model[1] and Curie-Weiss molecular field theory[2] are probably two great milestones in the theoretical foundations of magnetism. However, with the rapid developments in the quantum theories in the early twentieth century and technological developments such as high precession nanofabrication facilities in late 1900, spintronics has emerged as one of the pioneer branches of modern magnetism which demands a solid theoretical framework to extend the thorough understanding to a large number of newer phenomena. Many of these phenomena are manifestations of the quantum confinement effect offered by exclusively low-dimension of materials. In addition to that, exotic physical processes are revealed in the absolute short time window of observation especially in the sub-nanosecond to femtosecond regimes such as spin precessional motion and ultrafast demagnetization[3]. Furthermore, it is observed that strong light-matter interaction at the ultrashort timescale often plays a crucial role to control the mechanism behind these processes. Therefore, in this chapter, we shall briefly present the theoretical elements crucial for the understanding of the spin wave and its dynamics for low-dimensional magnetic structures. We shall begin with an overview of the different free energy components in a magnetic system followed by the basic theory behind the magneto-optical Kerr effect (MOKE) which has been exploited to understand the magnetization dynamics presented in the thesis. Subsequently, we shall describe the ultrafast demagnetization and possible theories attempting to provide a microscopic mechanism of the process. Finally, we will discuss the precessional spin dynamics occurring in the sub-nanosecond regime, spin wave dispersion along with the different intrinsic and extrinsic origins of the magnetic damping[3].

2.2 Free Energies in a Magnetic System

The free energy for a magnetic system under an external bias field can be written as the sum of several free energy components such as i) Zeeman energy, ii) dipolar energy, iii) exchange

energy, and iv) anisotropy energy which are discussed below[4].

2.2.1 Zeeman Energy

The Zeeman interaction energy of a magnetic specimen with total magnetization $\boldsymbol{M}$ subjected to an external field $\boldsymbol{H}$ can be represented by the expression $E_z = -\int \boldsymbol{M}.\boldsymbol{H}dV$. The magnetization tends to align itself towards the external field to minimize the Zeeman interaction energy.

2.2.2 Dipolar Energy

Dipolar energy is a direct consequence of the interactions between the magnetic dipoles in a system. This is often referred to as the magnetostatic self-energy or demagnetizing energy. In a 3d transition metal system which may be consisting of a large number of dipoles, the total dipolar interaction energy can be expressed as

$$E_d = \frac{\mu_B^2}{2}\sum_{i\neq j}\left[\frac{\boldsymbol{m_i}.\boldsymbol{m_j}}{r^3} - 3\frac{(\boldsymbol{m_i}.\boldsymbol{m_j})(\boldsymbol{m_i}.\boldsymbol{m_j})}{r^5}\right] \tag{2.1}$$

The dipolar energy distribution is known to have crucial effects in domain formation, spin wave propagation and various other phenomena.

2.2.3 Exchange Energy

The exchange interaction is purely quantum mechanical in origin. The exchange energy is usually expressed by the Heisenberg Hamiltonian:

$$H_{ex} = -2J\sum_{i,j}\boldsymbol{S_i}.\boldsymbol{S_j} \tag{2.2}$$

Where J is the exchange integral taking care of the Coulomb interaction and $\boldsymbol{S_i}$ and $\boldsymbol{S_j}$ represent the electron spins at two discrete atomic sites. However, an extension of the above expression in the continuum model approximation would be:

$$H_{ex} = A\int(\boldsymbol{\nabla}m)^2 dV \tag{2.3}$$

Where A, the exchange stiffness constant for specimen with lattice constant a is given by:

$$A = \frac{2JS^2}{a} \tag{2.4}$$

2.2.4 Energy due to Magnetic Anisotropy

Although the exchange energy is isotropic, very often the magnetic systems possess preferential directions of magnetization, known as the 'easy axis'[5]. This directional dependence is referred to as magnetic anisotropy which gives rise to another energy term in the

total energy consideration.

The primary contributors to this type of anisotropies are as follows.

2.2.4.1 Magnetocrystalline Anisotropy

The samples having strong epitaxial nature tend to show one or more specific directions of preferred directions irrespective of the macroscopic shape of the specimen. This is strongly influenced by the crystallographic axes of the material and is therefore known as magnetocrystalline anisotropy. This is a direct manifestation of the spin-orbit coupling (SOC) and therefore is a material property. The crystal field affects the spins and the total magnetic energy via the SOC and thereby plays a pivotal role in the spatial distribution of the spins with respect to the crystallographic axes associated with the symmetry of the crystal. The energy is generally expressed in terms of power series of harmonic functions of the angle between the principal axis and the magnetization vector. For example, the anisotropy energy for a cubic crystal can be written as[4]:

$$E_a = K_1(\alpha_1^2\alpha_2^2 + \alpha_2^2\alpha_3^2 + \alpha_3^2\alpha_1^2) + K_2\alpha_1^2\alpha_2^2\alpha_3^2 \quad (2.5)$$

With K_1 and K_2 being the anisotropy constants and α_1, α_2 and α_3 are the direction cosines along the Cartesian axes. However, for an hcp structure, the expression modifies to:

$$E_a = K_1 \sin^2\theta + K_2 \sin^4\theta \quad (2.6)$$

Where θ is the angle magnetization makes with the c-axis of the hcp crystal.

2.2.4.2 Shape Anisotropy

Shape anisotropy is a consequence of the demagnetizing effect due to the dipolar interaction in a magnetic system. The demagnetizing fields and the unsaturated magnetic charges near the edges of the specimen become quite significant, especially in the nanostructures. The shape anisotropic energy has the form:

$$E_{di} = -\int \boldsymbol{M}.\boldsymbol{H_d}dV \quad (2.7)$$

Where the demagnetizing field is related to the magnetization via demagnetizing tensor N

$$\boldsymbol{H_d} = -N\boldsymbol{M} \quad (2.8)$$

2.2.4.3 Surface and Interface Anisotropy

In the case of magnetic thin films and multilayered systems, the breaking of inversion symmetry gives rise to additional anisotropy. In such a case the effective anisotropy energy is usually written as a sum of a volume and a surface term[6]:

$$E_{ani} = \left[K_v^{eff} + \frac{K_s^{eff}}{d}\right] \sin^2\theta \tag{2.9}$$

Here, the volume term takes care of the magnetocrystalline energy and shape anisotropy contribution. The broken symmetry at the surface and interfaces changes the magnetocrystalline anisotropy which scales inversely with the layer thickness and becomes dominant in the ultrathin regime.

Apart from the anisotropy contributors discussed here, there can be other kinds of anisotropies such as perpendicular magnetic anisotropy (PMA) or strain-induced anisotropy which are also manifestations of broken symmetry, modification in the electronic band structure, competition between different free energies etc.

2.3 Magneto-Optic Kerr Effect

When a plane-polarized light faces reflection from the surface of a magnetic sample, the light gets converted to an elliptically polarized light with a finite rotation in the plane of polarization. This phenomenon is known as the magneto-optic Kerr effect (MOKE) and the angle is called the Kerr rotation[7]. As Kerr rotation is proportional to the magnetization of the reflector specimen, this principle has been widely accepted for the investigation of magnetic material employing optical techniques. Kerr rotation and Kerr ellipticity depend on circular dichroism and circular birefringence respectively and are connected by the following relation:

$$\theta_k + i\epsilon_k = \frac{k}{r} \tag{2.10}$$

Where r and k denote the parallel and perpendicular components of the electric field of the reflected light with respect to that of incident one.

2.3.1 Origin of MOKE

The electric field associated with light passing through a material medium exerts a force on the electron cloud causing a motion. Electrons move in a left-circular fashion when exposed to left circularly polarized (LCP) light. Similar to this, right-circular motion is produced by right circularly polarized (RCP) light. The radii of these two circular motions are equivalent in the absence of a magnetic field. The dielectric constants become identical. The external magnetic field, however, causes the electrons to experience an extra Lorentz force when there is a magnetic field present. The radii of the circular paths to the right and left will change and as a result, the dielectric constants of the two polarized modes will differ by a finite amount. Reflection changes each component's amplitude and phase. This causes the incident linearly polarized light to convert to an elliptically polarized light[8].

In a quantum mechanical depiction, spin-orbit interaction is held accountable for the Kerr effect. The movement of the electrons under the action of the electric field of light is represented as a magnetic vector potential

$$\boldsymbol{A} \sim \boldsymbol{S} \times \boldsymbol{\nabla} V$$

Where V denotes the potential of the electric field of the light. Although this effect exists in all materials, it is less noticeable in NM materials because the effect is cancelled out by an equal number of up and down spins. The impact for FM materials appears as a result of the imbalanced population of electrons.

2.3.2 MOKE Geometries

The Kerr effect can be classified into three groups according to how the magnetization vector is positioned with respect to the sample surface and the plane of light incidence. The geometry is a polar one when the magnetization lies parallel to the plane of incidence of light and perpendicular to the sample surface. This configuration is extensively used in the measurement of thin films and microstructured systems. The geometry is longitudinal if the magnetization is parallel to the plane of incidence of light and in the sample plane. Both p- and s-polarized light can have these two geometries. On the other hand, if magnetization is perpendicular to the plane of incidence yet lies in the plane of the sample, this is known as transverse MOKE geometry and it only applies to p-polarized light.

2.4 Time Scales in Magnetization Dynamics

Magnetization dynamics covers a wide variety of exotic physical phenomena spanning its timescale from fs to μs order. While the characteristic timescale of exchange interaction is fs, making it the fastest magnetic interaction, the motion of the domain wall happens to be the slowest having a timescale of a few μs. The timescales are inversely correlated with the corresponding interaction energies. The laser-induced ultrafast demagnetization occurs in a few hundred fs followed by the fast remagnetization which takes place in a few ps timescale. The magnetization precessional motion takes place in a tens ps to several ns time and the Gilbert damping associated with the precessional motion is observed in the ns timescale. Magnetic spin reversal, which is used for writing the data state in memory devices shares an almost similar timescale with the spin precession. The spin waves are associated with almost 100 ps to 10 ns of timescale. In the following sections, we will primarily discuss a theoretical framework for laser-induced ultrafast demagnetization, fast remagnetization, precessional dynamics and spin waves for a better understanding of the results presented later in the thesis.

2.5 Ultrafast Demagnetization

Laser-induced ultrafast demagnetization was first reported in 1996 by Beurepaire *et al*. The authors observed a drastic drop in the magnetization after shining an ultrashort laser pulse upon a Ni foil[9]. The demagnetization was exponential in nature with an associated time constant of ~270 fs known as ultrafast demagnetization time. This phenomenon is also supported by experiments carried out on other 3d transition metals, semiconductors and alloys. Ever since this breakthrough, the phenomena received not only widespread attention but also intense debate regarding the theoretical interpretation of its origin and mechanism[10]. There are many proposed mechanisms to explain the phenomena some of which we discuss below in detail.

2.5.1 Three Temperature Model

This was the first theoretical model used to understand the ultrafast demagnetization process which is an extension of the already existing two-temperature model. Bearepaire et al.[9] employed this simple model to explain their findings and to portray a physical description of the process as well. In this model, they considered interaction and energy exchange among three different heat reservoirs namely electron, spin and lattice heat baths with respective specific heat capacities and equilibrium temperatures. According to the model, the laser photon first interacts with the electron bath and creates non-equilibrium hot electrons above the Fermi level. The photons can not transfer their energy directly to the spins as it is discarded by the dipolar transition selection rule. The non-thermal electrons then equilibrate and interact with the spin and elevate the spin temperature and the spin phase memory is lost causing a rapid drop in net magnetization of the system. Following the process where the spin reservoir interacts with both the electron and lattice reservoirs, a redistribution of energy takes place lowering the spin and electron temperature but causing an increase in the lattice temperature which is further dissipated in a longer timescale via interaction with the surroundings (substrate etc.). This model solves three coupled differential rate equations given below to understand the dynamics of the absolute temperatures of each of the heat baths in a separate manner.

$$C_e(T_e)\frac{dT_e}{dt} = -G_{es}(T_e - T_s) - G_{el}(T_e - T_l) + P(t) \tag{2.11}$$

$$C_s\frac{dT_s}{dt} = -G_{es}(T_s - T_e) - G_{sl}(T_s - T_l) \tag{2.12}$$

$$C_l\frac{dT_l}{dt} = -G_{el}(T_l - T_e) - G_{sl}(T_l - T_s) \tag{2.13}$$

Here, C_e, C_l, and C_s are respective specific heat capacities of the electron, spin and lattice heat baths with absolute temperatures T_e, T_l and T_s. G_{es}, G_{el} and G_{sl} express the electron-spin,

electron-lattice and spin-lattice coupling parameters. $P(t)$ is the source term representing the laser photon energy which only has a direct effect on the dynamics of the electronic heat bath. It is usually represented by a Gaussian profile and the strength varies depending on the laser fluence. Solving these three equations gives fairly accurate reproduction of the experimental ultrafast demagnetization and fast remagnetization data as demonstrated by Beaurepaire et al. Subsequently, an analytical solution of the model applicable to the lower laser fluence regime has been proposed by Dalla longa et al.[11] and the formalism is widely accepted for its robustness. Although this model was successful to understand the dynamics of various magnetic systems nevertheless, it received criticism for being a 'phenomenological' one as it does not provide any microscopic insight into the system.

2.5.2 Demagnetization via Spin-Orbit Interaction

The first laser-induced ultrafast demagnetization puts a lot of questions in front of the community. However, one of the most important conclusions that came out was that since the demagnetization is taking place within 50-100 fs, the speed limit is no longer decided by the timescales associated with Zeeman, dipolar or spin-lattice interaction. Zhang and Hubner[12] proposed a model based on the cooperative action of the laser and the spin-orbit interaction (SOI). In their paper, they showed that, in the absence of the SOI, the electromagnetic field of the laser is not enough to drive the demagnetization process in a truly ultrafast timescale as there is no spin relaxation without SOC. On the other hand, SOI alone is not capable of a significant drop in magnetization in absence of a laser field. Their model demonstrates that in presence of the SOI, many of the singlet and triplet states get mixed up in a multi-level model system and as a consequence, many of the transitions which were initially forbidden emerge as allowed. This becomes the new pathway for the laser field to manipulate the dynamics in ultrashort time. Therefore laser-induced demagnetization can be interpreted as a cooperative effect of the external laser field and internal SOI of the system.

2.5.3 Phonon Mediated Spin Flip Scattering

Most of the theoretical interpretations that immediately followed the discovery of ultrafast demagnetization fall short to provide a clear picture to understand the dissipation of the spin angular momentum in this timeframe. Based on the existing theory of Elliott-Yafet (EY)[13,14] where spin flip occurs via the interaction with the impurity or phonon in a system, Koopmans et al attempted to model the ultrafast demagnetization phenomena. This model predicts that the probability of a majority or minority spin having its state changes due to the phono-mediated

scattering and during the scattering the spin momentum is transferred to the lattice phonon. This scattering causes the mixing of majority and minority spin bands having similar energy near the Fermi level which leads to a drop in magnetization. They derived a rate equation to reproduce the ultrafast demagnetization which is given by[10]:

$$\frac{dm}{dt} = Rm\frac{T_p}{T_c}\left[1 - coth\left(\frac{mT_c}{T_e}\right)\right] \tag{2.14}$$

Where m is the normalized magnetization to its saturated value and T_e, T_p and T_c are the electron, phonon (lattice) and Curie temperature. R is a material-dependent scaling factor and is given by:

$$R = \frac{8a_{sf}T_c^2 G_{ep}}{K_B T_D^2 D_s} \tag{2.15}$$

Here, G_{ep}, T_D and D_s are the electron-phonon coupling parameter, Debeye temperature and atomic moment relative to the Bohr magneton. The term a_{sf} represents the spin-flip probability. As the scaling factor directly correlates to the spin-flip probability, a higher value of a_{sf} would result in a faster demagnetization time. The model also can be extended to demonstrate a possible inverse correlation of the demagnetization time with the Gilbert damping of the system which is associated with the precessional dynamics in the ns regime.

2.5.4 Electron-Electron Coulomb Scattering

This model as proposed by M. Krauβ et al.[15] relies also on the spin-flip scattering process. However, the model considers the electron-electron scattering under strong Coulomb force as the underlying mechanism and does not require an impurity-mediated scattering. Depending upon the band structure and the lattice temperature, the electrons are assumed to have a standard Fermi-Diac distribution prior to interaction with the laser phonon. At this time there exists a gap in the majority and minority spin bands giving rise to a non-zero finite magnetization. Due to the ultrafast optical excitation, a non-equilibrium electron distribution is created leading to strong intraband as well as interband scattering. Although the matrix elements suggest that the photon can not directly impact the magnetization for a dipolar-type transition, ultrafast demagnetization takes place as a consequence of the strong interband scattering which alters the electron population in both the majority and minority bands. A further energy transfer to the lattice bath gives rise to the process of fast remagnetization.

2.5.5 Relativistic Quantum Electrodynamic Mechanism

Another mechanism based on quantum electrodynamics has been put forward by Bigot *et al*[16] which describes ultrafast demagnetization as a sequence of coherent and incoherent

interactions. According to this model, as the laser pulse shines upon the magnetic system it undergoes a coherent interaction first. In this phase, the angular momentum of the photon is modified within the first 50 fs via interaction with the spin and electronic charges. Whereas the SOI considers the ionic potential in a material, this coherent interaction has a relativistic quantum electrodynamic origin beyond the SOI. Subsequently, the thermalization of spin and charge starts which is an incoherent interaction in nature. In this phase, the electronic wavefunction loses its initial phase memory that results in a sudden loss of magnetic order i.e. ultrafast demagnetization.

2.5.6 Superdiffusive Spin Current Transport

As we have stated earlier that the most intriguing part that attracted the community's attention was finding a channel that can offer dissipation of spin angular momentum in an ultrashort timescale. Most of the proposed mechanisms were based on spin-flip scattering events so far to explain the loss of magnetic order. In 2010, Battiato et al.[17] adopted a completely novel physical mechanism to answer the long-standing question. They attempted to explain the event purely on the basis of the spin-dependent transport of hot electrons devoid of any spin-flip channels. They construct an equation of motion for the laser-excited spin-polarized electrons in the superdiffusive regime. Although the model takes multiple collisions into account, all of those are assumed to be spin-conserving. According to this model, a *d*-band electron on receiving excitation from the laser photon reaches the *sp*-like band which is above the Fermi level. The *sp*-like electrons have significantly higher mobility so *d*-electrons may be treated quasi-statically and as localized. Assuming the emission of hot electrons isotropic and uniform through a solid angle the model first calculates the 'first generation' (before having any collisions) electron flux as:

$$\phi(z,t,z_0,t_0) = \frac{[\widetilde{\Delta t}]}{2(t-t_0)^2}\left(exp\left[-\left[\frac{\widetilde{\Delta t}}{\tau}\right]\Big/_{[\widetilde{\Delta t}]}\right]\right)^{(t-t_0)} \times \Theta\left[(t-t_0)-\left|[\widetilde{\Delta t}]\right|\right] \qquad (2.16)$$

Where z_0 refers to the starting position of the hot electron at time t_0. The flux (number of electrons per unit time) is calculated at z=z at time t while electron flow is through the plane perpendicular to the z-axis. Considering an average over the distribution of hot electron sources S^{ext}, the first generation flux becomes:

$$\Phi(z,t) = \int_{-\infty}^{+\infty} dz_0 \int_{-\infty}^{+t} dt_0 S^{ext}(z_0,t_0)\phi(z,t,z_0,t_0) \qquad (2.17)$$

After that, a continuity equation is written for the number density of the same electrons:

$$\frac{\partial n^{[1]}}{\partial t} + \frac{n^{[1]}}{\tau} = -\frac{\partial \hat{\phi}\, S^{ext}}{\partial z} + S^{ext} \tag{2.18}$$

The process is extended with a suitable approximation of multiple collisions to write the equation for the number density of the 2nd, 3rd etc. generation of electrons. Finally, a set of transport equations are unified as follows:

$$\frac{\partial n^{tot}}{\partial t} + \frac{n^{tot}}{\tau} = \left(-\frac{\partial \hat{\phi}}{\partial z} + \hat{I}\right)\left(\hat{S} n^{tot} + S^{ext}\right) \tag{2.19}$$

These sets of equations are numerically solved to arrive at the time-dependent density profile of the excited carriers as well as the magnetization profile. One of the interesting parts of the theory is that it represents the electron cascade motion in the superdiffusive regime i.e., the electronic motion is ballistic like ($\sigma^2 \sim \gamma^2$) in the small time and diffusive like (($\sigma^2 \sim \gamma$)) in the longer times. The main essence of this model is that majority and minority carriers have different mobility and lifetimes which causes a rapid depletion of the majority spins in the ferromagnetic material resulting in ultrafast demagnetization. Additionally, this model well explains the faster and slower and two-step demagnetization observed for the *3d* ferromagnets like Ni and *4f* ferromagnets like Gd.

2.5.7 Thermal Macrospin Model

In this model, the fluctuation in the spin sub-system is represented by a thermal macrospin[18]. This model also considers that the electron receives the thermal energy from the laser photon first and creates the non-equilibrium electron population which is then redistributed in the spin and lattice subsystems. According to the model, the angular momentum is dissipated via the spin-flip process which is stochastic in nature. The stochastic process is accelerated by elevated electron temperature and the spin fluctuations at high energy are statistically averaged to extract temperature-dependent parameters. The actual ultrafast dynamics is governed by Landau-Lifshitz Bloch (LLB) equation and the microscopic spin-flips are understood in terms of coupling between the spin and electron sub-systems. The model can explain the phenomena from a thermal origin and it also reduces the standalone atomistic computational time.

2.5.8 Optical Intersite Spin Transfer

A recently suggested method called optical inter-site spin transfer (OISTR)[19] can manage the spins of a magnetic specimen by effectively redistributing spin angular momentum between multiple sublattices. It has been demonstrated that this OISTR effect drives the full ultrafast spin dynamics within 10-20 fs of the laser pulse excitation. This effect has also been demonstrated in NM/FM heterostructures, where the majority of spins at the interface flow

towards the NM and the minority to an FM. Later, spin-orbit-induced spin-flip scattering results in the demagnetization of their minority spins. The OISTR effect dominates the first spin dynamics in multi-sublattice materials and causes an ultrafast demagnetization that is both faster and more efficient[20].

2.6 Precessional Magnetization Dynamics

When a magnetic material is subjected to an external magnetic field, all the spins are then aligned along the direction of an effective field comprised of the magnetic fields representing the competing energies such as Zeeman, dipolar and anisotropy energies along with the exchange energy. This takes place as the system attempts to minimize the total energy and the resultant spin configuration may be regarded as the ground state. In this state, the system can be excited by an rf field or a femtosecond laser pulse. In the case where the system is subjected to laser photon, within the first few hundred femtoseconds it shows a rapid magnetization quenching known as ultrafast demagnetization. As we have discussed in the earlier sections, this is followed by a relaxation mechanism of electrons and spins. However, the relaxation is usually associated with two different timescales. The energy dissipation of electrons and spins to the lattice taking place via the electron-phonon interaction, known as fast relaxation has a characteristic time of a few ps. The heat exchange causes a significant elevation in lattice temperature which in turn, causes an ultrafast alteration in the magnetocrystalline anisotropy of the specimen. As a result, the effective field attempts to revert back to its equilibrium value and exerts a torque. This serves as the triggering to set a damped spiral motion of the spins around the effective magnetic field. For the case of the rf field being used as the excitation instead of an ultrashort laser pulse, it acts as the trigger for precessional motion. The slow relaxation is primarily a manifestation of the energy dissipation from the lattice to the surroundings. It usually occurs in the few hundreds of ps time regime. In this timescale, the precessional motion starts slowing down and a Gilbert damping comes into play. Investigation of precessional magnetization dynamics is imperative for the achievement of a thorough understanding of a material system to unlock its potential in spin-based device applications. The precessional dynamics contains two important pieces of information about the system: spin wave mode frequencies and the associated damping parameter. Here we first describe the theoretical foundations of the precessional frequency along with spin wave dispersion relation followed by a theoretical understanding of different origins of damping.

2.6.1 Landau-Lifshitz-Gilbert Equation

This precessional dynamical motion is completely governed by Landau-Lifshitz-Gilbert (LLG) equation on a semi-classical approach[21,22]. Here we briefly describe the formalism.

The torque ($\boldsymbol{\tau}$) experienced by a magnetic dipole with moment $\boldsymbol{\mu}$ placed in a magnetic field $\boldsymbol{H}$ is given by:

$$\boldsymbol{\tau} = \boldsymbol{\mu} \times \boldsymbol{H} \tag{2.20}$$

Also, torque refers to the rate of change of angular momentum ($\mathbf{L}$) which is also connected to the magnetic moment $\boldsymbol{\mu}$ via the gyromagnetic ratio i.e.

$$\boldsymbol{\tau} = \frac{d\boldsymbol{L}}{dt} = -\frac{1}{\gamma}\frac{d\boldsymbol{\mu}}{dt} \tag{2.21}$$

Substituting this in the previous equation results in the following equation:

$$\frac{d\boldsymbol{\mu}}{dt} = -\gamma(\boldsymbol{\mu} \times \boldsymbol{H}) \tag{2.22}$$

When represented for a magnetization $\boldsymbol{M}$, the equation takes the form

$$\frac{d\boldsymbol{M}}{dt} = -\gamma\left(\boldsymbol{M} \times \boldsymbol{H_{eff}}\right) \tag{2.23}$$

Here, the effective field considers all the contributions from Zeeman, exchange, demagnetizing and anisotropic contributions as well as any time-dependent modulation taking place.

$$\boldsymbol{H} = \boldsymbol{H_{eff}} = \boldsymbol{H_z} + \boldsymbol{H_{ex}} + \boldsymbol{H_{demag}} + \boldsymbol{H_{ani}} + \boldsymbol{H}(t) \tag{2.24}$$

However, as the equation represents a dissipationless motion of moments, Landau and Lifshitz came up with an additive term to represent the rotational motion correctly:

$$\frac{d\boldsymbol{M}}{dt} = -\gamma\left(\boldsymbol{M} \times \boldsymbol{H_{eff}}\right) + \frac{\lambda}{M_s^2}\boldsymbol{M} \times \left(\boldsymbol{M} \times \boldsymbol{H_{eff}}\right) \tag{2.25}$$

Later Gilbert introduced[22] the damping term $\alpha = \frac{\lambda}{M_s}$ and arrived at the LLG equation:

$$\frac{d\boldsymbol{M}}{dt} = -\gamma\left(\boldsymbol{M} \times \boldsymbol{H_{eff}}\right) + \frac{\alpha}{M_s}\left(\boldsymbol{M} \times \frac{d\boldsymbol{M}}{dt}\right) \tag{2.26}$$

2.6.2 Ferromagnetic Resonance

The electron spins in a ferromagnetic specimen subjected to a steady magnetic field continue to precess and the frequency of the precessional motion is given by Larmor's formula:

$$\omega = \gamma H_{eff} \tag{2.27}$$

However, with an alternating magnetic field ($\boldsymbol{B}$) applied perpendicular to the direction of the steady field, the magnetic system absorbs energy from the electromagnetic field resulting in a resonance which is known as the ferromagnetic resonance (FMR). Under this condition, the

frequency enhances from the Larmor frequency and is obtained from the following relation[23]:

$$\omega = \gamma\sqrt{BH_{eff}} \tag{2.28}$$

2.6.3 Uniform Precession (Kittel Formula) and Macrospin Approximation

If magnetization within a material becomes completely uniform then its behaviour can be studied, in principle, from the understanding of the behaviour of a single, giant magnetic moment representing all the tiny moments. This formalism is known as the macrospin model. Under macrospin approximation, Kittel[24] considered the demagnetizing field contributions and theoretically derived the formula for FMR frequencies when the specimen has certain regular geometry. The generalized Kitel formula of mode frequency for an ellipsoidal specimen is given by:

$$\omega = 2\pi f = \gamma\sqrt{\left[H_z + \left(N_y - N_z\right)M_z\right]\left[H_z + (N_x - N_z)M_z\right]} \tag{2.29}$$

For a thin film, $N_x = 4\pi$ and $N_y = N_z = 0$; Kittel formula modifies to:

$$\omega = 2\pi f = \gamma\sqrt{H_z[H_z + 4\pi M_z]} \tag{2.30}$$

2.6.4 Spin Waves and Magnon Dispersion relation

In the case of uniform precession, all the spins precess in the same manner. However, when the assembly of spins are subjected to some local excitation, then the phase of the energy propagates through the medium as a wave. This is called spin wave or magnon in a quantum formalism[24]. Depending on the nature of interactions and the wavelength regime, the SWs can be of exchange-dominated, dipolar dominated and dipole-exchange dominated type.

2.6.4.1 Exchange Spin Wave

When the wavelength of the SW is small enough, the exchange interaction predominantly defines the nature of the spin waves. The dispersion relation for a one-dimensional system can be worked out analytically as[24]:

$$\hbar\omega = 4JS(1 - coska) \tag{2.31}$$

Where J is the exchange integral and a is the lattice periodicity. In the long wavelength approximation, this relation modifies to a quadratic function of k signifying an isotropic dispersion:

$$\hbar\omega = 2JSa^2k^2 \tag{2.32}$$

2.6.4.2 Dipolar Spin Wave

Magnetostatic or dipolar SW modes are reported by Damon and Eshbach. If the spin wave propagation is in sample plane and the magnetization is perpendicular to the sample plane, the dispersion is known as magnetostatic forward volume mode (MSFVM). The dispersion relation for a MSFVM mode can be expressed as[25]:

$$\omega = \gamma \sqrt{(H - 4\pi M_s)\left[H - 4\pi M_s \left(\frac{1 - e^{-kd}}{kd}\right)\right]} \tag{2.35}$$

When the magnetization lies in the sample plane and the propagation of the SW lies along the magnetization vector, magnetostatic backward volume mode (MSBVM) is observed with the dispersion relation given by:

$$\omega_{BV} = \gamma \sqrt{H\left[H + 4\pi M_s \left(\frac{1 - e^{-2kd}}{kd}\right)\right]} \tag{2.34}$$

When the magnetization and propagation vector both lie in the same plane but they are perpendicular to each other, it gives surface wave mode (MSSWM) of Damon-Eshbach mode with dispersion relation:

$$\omega_{DE} = \gamma \sqrt{[H(H + 4\pi M_s) + (2\pi M_s)^2(1 - e^{-2kd})]} \tag{2.33}$$

Interestingly, MSSWM show positive whereas MSBVM shows negative dispersion relation.

2.6.4.3 Dipole Exchange Dominated Modes

There can be other kinds of SWs originated by a strong influence from both the dipolar and exchange interactions. The dispersion of such a wave can be obtained from the Kittel-Herring formula[26]:

$$\omega = \gamma \sqrt{\left(H + \frac{2A}{M_s^2}k^2\right)\left[H + \frac{2A}{M_s^2}k^2 + 4\pi M_s \sin^2\theta_k\right]} \tag{2.36}$$

SWs can propagate along the finite thickness (d) of the medium and in the exchange-dominated regime create perpendicular standing spin wave (PSSW) modes with dispersion given by (p) being the quantization number giving the dispersion relation as follows:

$$\omega_{pssw} = \gamma \sqrt{\left(H + \frac{2A}{M_s^2}\left(\frac{p\pi}{d}\right)^2\right)\left[H + \frac{2A}{M_s^2}\left(\frac{p\pi}{d}\right)^2 + 4\pi M_s\right]} \tag{2.37}$$

2.7 Magnetic Damping

The constant dissipation of spin angular momentum across the lattice during precessional spin

dynamics causes the precessional amplitude to continuously diminish over time, which is referred to as magnetic damping. Understanding the theoretical foundation of the magnetic damping parameter is critical since the achievement of external control over magnetic damping is a crucial element in the construction of sophisticated spintronic devices. Since Landau and Lifshitz's original (1935)[21] theory of magnetic relaxation and subsequent modification by T. Gilbert's (1955)[22], different theoretical perspectives have been investigated to gain insight into its underlying mechanisms. Depending on where it originated from, magnetic damping may have two crucial components: intrinsic and extrinsic[27,28].

2.7.1 Intrinsic Origins

As the name suggests Intrinsic damping is a material property and thus can not be altered externally. The main intrinsic origins for dampings are spin-orbit coupling, eddy current, phonon drag etc. Below we provide a brief description of these mechanisms:

2.7.1.1 Spin-Orbit Coupling

Spin magnetic moments in a magnetic specimen are coupled with the orbital moments via spin-orbit interaction. Despite that what makes it difficult for the orbital magnetic moments to follow the spin motions is the fact that they are extremely vulnerable to fluctuations produced by lattice deformations. As a result, the phonon, which carries the uniform magnon energy and maintains the crystal momentum, destroys the spin angular momentum. Magnetic damping is a result of this energy loss. In 1970 V. Kambersky[29] first established this process' microscopic details and explicit description of the damping coefficient, and in 1976[30] he developed the Torque Correlation Model, which is a more illustrative theory. Based on the SOC there can be two different physical processes behind the damping: a) phonon mediated spin-flip scattering and b) ordinary scattering.

a) Phonon Mediated Spin Flip Scattering

This model is based on the earlier scattering theory proposed by Elliott and Yafet[13,14] and the s-d relaxation mechanism as put forward by Kittel[31]. First, the spin momentum from the quasi-static *d*-electrons is transferred to the *s*-electrons which are itinerant in nature. This causes coupling between the interband electrons via *s-d* interaction. The itinerant s-electrons may suffer scattering with the lattice phonons and faces a spin flip. Subsequently, this also affects the *d*-electrons and modifies their spin state. According to this model, the Gilbert damping directly correlates to the density of states at the Fermi level and is inversely related to the electron-phonon collision time period [29]. It can be expressed as:

$$\alpha = D_F \frac{\gamma \hbar^2 (\delta g)^2}{4\tau M_s} \tag{2.38}$$

As τ^{-1} refers to the collision frequency, it explains that a higher rate of electron-phonon collision would result in a higher value of intrinsic damping.

b) Ordinary Scattering

This type of scattering takes place within the same energy sub-band but with different wave vectors because of the Fermi surface deformations related to the SOC. Due to the SOC, the energy levels of spins are changed during the precessional motion, energy levels lying below the Fermi level may rise above it and vice versa and the spin population redistribution continues resulting in an oscillation in the Fermi surface, known as Fermi surface breathing[29]. In this process magnon mode breaks in an electron-hole pair which gets further diminished via scattering with the lattice[32]. This model calculates damping as:

$$\alpha = D_F \frac{\gamma \tau \xi^2 (\delta g)^2}{4M_s} \tag{2.39}$$

Later it has been found that the electron-hole pair may generate in the same sub-band or different subbands leading to intraband and interband pair generation. It will also be interesting to note that the damping is conductivity-like in the case of intraband scattering which is more appropriate at low temperatures. For interband scattering, the damping is resistivity-like and this mechanism is valid in the higher temperature regime. The intrinsic damping is proportional to ξ^3 and τ (ξ^2 and τ^{-1}) in the case of intraband (interband) scattering processes[33].

2.7.1.2 Eddy Current

The idea of eddy current originates from Lenz's law in electromagnetism and it opposes the very cause of it. In the magnetic material, the precessing magnetic moment produces a time-varying magnetic field that drives an emf and generates eddy current in ferromagnetic metals. This works against the spin precession and induces damping. The value of the damping for a thin film having complete penetration by an rf driving field can be obtained from[34]:

$$\alpha_{eddy} = \frac{\gamma M_s}{6} \left(\frac{4\pi}{c}\right)^2 \sigma d^2 \tag{2.40}$$

Where d is the thickness of the film and other signifies their usual meaning.

2.7.1.3 Phonon Drag

This mechanism is proposed by H. Suhl and is based on magnon-phonon scattering. According to the model, magnon energy may directly dissipate from its uniform motion to the lattice.

Alternatively, the energy dissipation may be associated with the excitation of a non-uniform spin wave. The former method is called the phonon drag and seems stronger in the magnetostrictive samples. This formalism gives the following contribution to Gilbert damping[34] :

$$\alpha_{phonon} = \frac{2\eta\gamma}{M_s}\left[\frac{B_2(1+\sigma)}{Y}\right]^2 \tag{2.41}$$

2.7.2 Extrinsic Origins

There are plenty of physical processes that externally contribute to damping. They are not specific to the material and often offer great external tunability of the damping parameter.

2.7.2.1 Spin Pumping

When a ferromagnetic (FM) material is allowed to share an interface with a non-magnetic (NM) material, spin pumping can take place ensuring significant enhancement of magnetic damping. In spin pumping, the magnetization precession induced by the ultrashort laser pulse or an rf field acts as the source of spin angular momentum. The precessing spins then transfer the spin momentum to the adjacent NM material. This causes the spins to lose a part of the driving torque which leads to slowing down their precessional motion thereby introducing an additional source of damping. The NM layer serves as a spin reservoir. Although several pioneering works by Hurdequint et al. (1988) and L. Berger et al. (1996)[35] proposed a mechanism where non-equilibrium spins can accumulate at the FM/NM interface which may further dissipate through the NM layer, the first theoretical framework to comprehend the spin pumping was put forwarded by Tserkovnyak et al (2002)[36]. The authors considered time-dependent adiabatic scattering as the sole underlying mechanism and correlated the quantum mechanical reflection and transmission coefficients to the spin mixing conductance and the spin diffusion lengths, which are imperative to parameterize the spin pumping. Below we briefly describe the formalism :

The formalism proposes the 2×2 spin current matrix as:

$$\hat{I} = \hat{1}\frac{I_c}{2} - \frac{e}{\hbar}\boldsymbol{\sigma}.\boldsymbol{I_s} \tag{2.42}$$

Now, under no applied charge current, I_c vanishes. The term I_s consists of a spin pumping and a spin backflow contribution. If the spin pumping from the magnetization precession becomes fast enough and so that the pumped spin leaves the interface faster, the NM may be regarded as the perfect spin sink. This consideration results backflow to be negligible and the current matrix takes the form[36]:

$$\hat{I} = -\frac{e}{\hbar}\boldsymbol{\sigma}.\boldsymbol{I}_s^{pump} \tag{2.43}$$

Where the pumped spin current is related to the real (g_r) and imaginary part (g_i) (which are again functions of quantum mechanical reflection and transmission coefficients) of the spin mixing conductance as follows:

$$\boldsymbol{I}_s^{pump} = \frac{\hbar}{4\pi}\left[g_r\boldsymbol{m}\times\frac{d\boldsymbol{m}}{dt} - g_i\frac{d\boldsymbol{m}}{dt}\right] \tag{2.44}$$

With each complete precessional motion of the spin, the amount of the spin angular momentum that is pumped to the adjacent NM layer is directly proportional to the real part of the spin mixing conductance. This introduces additional damping in the LLG equation. In this theory, the backflow has been considered to be negligible which can be significant if the thickness of the NM layer is shorter than the spin diffusion length and the spin flow from FM to NM is not ballistic in nature. In this case, it alters the spin accumulation at the interface and reduces the amount of enhancement of damping which would have been observed otherwise. The condition for a negligible backflow is given by[36]:

$$\beta \gg \frac{1}{g_r} \tag{2.45}$$

It is important to note that the spin pumping effect greatly depends on the SOC strength of the NM material in the junction. As the SOC scales with Z^4 where Z is the atomic number; heavy metals such as Pt, Pd, W and Ta can perform better as a spin reservoir and show better enhancement in damping through spin pumping in comparison to the materials with low SOC strength like Cu, Zn, Al etc. Spin pumping serves as a major extrinsic source for damping in suitable FM/NM heterostructures.

2.7.2.2 Spin Memory Loss

The physical process of spin memory loss was proposed by T. Valet et al. in 1993[37]. It is another important extrinsic source of damping in the case of FM/NM heterostructures. It arises mostly when the interface itself acts as a perfect spin sink. In this case, a spin current generated in the FM layer can not enter the adjacent NM layer completely. Instead, The interface serves as the sink and the spin current faces a partial depolarization[38] at the interface before even entering the NM layer[39]. The current density at the NM layer can be expressed as:

$$J_S^{NM} = (1-\delta)J_S^{FM} \tag{2.46}$$

Where δ represents the coefficient of spin memory loss. The process significantly hinders spin transport across the interface and reduces interface transparency. Therefore, the reduction of spin memory loss by efficiently engineering sharp interfaces is favourable for technological

applications of the heterostructure.

2.7.2.3 Two Magnon Scattering

It is considered that the initial argument of magnetic relaxation stemming from spin-orbit coupling via interband and intraband scattering is independent of the spin precession frequency. Later experimental findings, however, defy this notion and show a damping parameter that is frequency sensitive. In order to resolve this contradiction, the presence of a further frequency-dependent contribution to damping is suggested. According to the theory, a uniform precessional mode ($k= 0$) may be scattered to form non-uniform modes ($k\neq0$) in magnetic thin films and heterostructures if there are magnetic defects and inhomogeneities present[40]. The procedure is described as two-magnon scattering (TMS)[41]. It is an inelastic scattering process where the momentum of the magnons is not conserved but the energy is. The TMS contribution to precessional dynamics is primarily influenced by three variables: the precessional frequency, the angle between the sample's easy axis and the applied magnetic field, and the thickness of the magnetic film. With rising precessional frequency, there are more degenerate magnons available for scattering which in turn rises the magnon-magnon scattering probability as well. Magnon degeneracy rapidly reduces as the angle between the sample's easy axis and the external magnetic field increases. When the sample magnetization is completely oriented along the out-of-plane direction, the degeneracy finally disappears. The FM layer thickness exhibits an inverse square dependence on the TMS contribution to the[42].

2.7.2.4 Non-Local Spin Injection

Non-local ‘injection’ of spin can significantly contribute to the damping of the specimen in the case of FM/NM type of heterostructure especially when the NM has a considerable SOC. In principle, this mechanism may be regarded as the converse mechanism of spin-pumping. Here, in general, the spin current is generated in the NM layer and on entering the FM layer they exert a torque acting against the precessional motion of the spin, resulting in the enhancement of damping. There are many physical processes that can lead to such non-local injection of spin angular momentum. One of the most widely used examples of the mechanism can be the spin Hall effect (SHE)[43]. In SHE, charge current applied across an NM layer with high SOC causes spin-dependent scattering, which leads to the development of spin polarization along the transverse path of the NM material. Through the NM/FM interface, this spin polarization is transmitted to the adjoining FM layer and exerts torque on its precessing magnetization. This torque can either raise (damping-like torque) or lower (anti-damping-like torque) the damping

of the combined FM/NM heterostructure. The STT generated via other possible mechanisms such as the Rashba-Edelstein effect and various spin-caloric effects can also contribute to the magnetic damping via non-local spin injection[44].

2.7.2.5 Inhomogeneous Magnetic Anisotropy

The presence of strong magnetic anisotropy creates a directional preference for the spin alignment within the system. If the external bias field is much weaker in comparison to the magnetic anisotropy of the system, this damping might enhance. In this case, the ground state spin configuration is poorly aligned with the direction of the applied bias field. As the bias field has a weaker contribution to the total effective magnetic field, the precessional motion is controlled by the effective anisotropy field[45]. This causes enhancement in damping.

2.7.2.6 Magnetic Defects

Any impurity present in the ferromagnetic specimen may give rise to scattering events and might add an additional contribution to the damping. The uniformly precessing spin might suffer an elastic scattering with the impurity scattering centres resulting in a greater rate of energy loss by the spin and faster relaxation via dephasing of the precessional motion. This can enhance the observed damping from the specimen significantly. A specimen with reduced defect density can efficiently lower this contribution to the damping.

2.8 Interfacial Spin Transparency

The spin transparency (T) of an FM/NM interface controls the transfer of spin angular momentum through the interface and accounts for all potential implications that could cause the electrons to be back-reflected from the interface rather than transmitted. T is impacted by both intrinsic and extrinsic interfacial variables, including the thickness of both the layers, the resistivity of the NM layer, interfacial spin mixing conductance, Fermi velocity, band-structure mismatch, interface imperfections, etc[46]. A high and configurable T-value is preferred for interfaces in spin current-based applications, making the study of interfacial transparency in NM/FM heterostructures a crucial area of research in contemporary spintronics. There are two models that can be used to determine the T-value of such an interface. These are a) the spin-Hall magnetoresistance (SHM) model[47] and b) the spin transfer torque model (STT). The former model considers the spin current flow to be a ballistic one and also considers a finite backflow from the NM layer. In STT formalism, the drift-diffusive approach is adopted and T is extracted considering the action of a field and damping like spin torque. Under the approximation that the thickness of the NM layer is much larger than its spin diffusion length,

the STT model neglects the spin backflow and often results in a higher estimation of T[48].

2.9 References

[1]W. Heisenberg, Z. Phys. **49**, 619 (1928).
[2]P. Weiss, Journal de Physique Théorique et Appliquée **6**, 661 (1907).
[3]A. Barman and J. Sinha, *Spin dynamics and damping in ferromagnetic thin films and nanostructures* (SPRINGER INTERNATIONAL PUBLISHING, 2019).
[4]A. H. Morrish, in *The Physical Principles of Magnetism*2001), pp. 332.
[5]J. M. D. Coey, *Magnetism and Magnetic Materials* (Cambridge University Press, Cambridge, 2010).
[6]P. Bruno and J. P. Renard, Appl. Phys. A **49**, 499 (1989).
[7]J. Kerr, The London, Edinburgh, and Dublin Philosophical Magazine and Journal of Science **3**, 321 (1877).
[8]Z. Q. Qiu and S. D. Bader, Rev. Sci. Instrum. **71**, 1243 (2000).
[9]E. Beaurepaire, J. C. Merle, A. Daunois, and J. Y. Bigot, Phys. Rev. Lett **76**, 4250 (1996).
[10]B. Koopmans, J. J. Ruigrok, F. D. Longa, and W. J. de Jonge, Phys. Rev. Lett. **95**, 267207 (2005).
[11]F. Dalla Longa, J. T. Kohlhepp, W. J. M. de Jonge, and B. Koopmans, Phys. Rev. B **75** (2007).
[12]G. P. Zhang and W. Hübner, Phys. Rev. Lett **85**, 3025 (2000).
[13]R. J. Elliott, Phys. Rev. **96**, 266 (1954).
[14]Y. Yafet, in *Solid State Phys.*, edited by F. Seitz, and D. Turnbull (Academic Press, 1963), pp. 1.
[15]M. Krauß, T. Roth, S. Alebrand, D. Steil, M. Cinchetti, M. Aeschlimann, and H. C. Schneider, Phys. Rev. B **80**, 180407 (2009).
[16]J.-Y. Bigot, M. Vomir, and E. Beaurepaire, Nat. Phys **5**, 515 (2009).
[17]M. Battiato, K. Carva, and P. M. Oppeneer, Phys. Rev. Lett. **105**, 027203 (2010).
[18]U. Atxitia, O. Chubykalo-Fesenko, J. Walowski, A. Mann, and M. Münzenberg, Phys. Rev. B **81** (2010).
[19]F. Willems, C. von Korff Schmising, C. Strüber, D. Schick, D. W. Engel, J. K. Dewhurst, P. Elliott, S. Sharma, and S. Eisebitt, Nat. Commun. **11**, 871 (2020).
[20]D. Steil *et al.*, Physical Review Research **2**, 023199 (2020).
[21]L. Landau and E. Lifshitz, in *Perspectives in Theoretical Physics*, edited by L. P. Pitaevski (Pergamon, Amsterdam, 1992), pp. 51.
[22]T. L. Gilbert, IEEE Trans. Magn. **40**, 3443 (2004).
[23]C. Kittel and P. McEuen, *Introduction to solid state physics* (Wiley New York, 1996), Vol. 8.
[24]C. Kittel, Phys. Rev. **73**, 155 (1948).
[25]R. W. Damon and J. R. Eshbach, J. Phys. Chem. Solids **19**, 308 (1961).
[26]C. Herring and C. Kittel, Phys. Rev. **81**, 869 (1951).
[27]U. M. S. I. F. o. Nanomagnetism, 143 (2005).
[28]A. Barman and J. Sinha, *Spin Dynamics and Damping in Ferromagnetic Thin Films and Nanostructures* (Springer International Publishing, 2018).
[29]V. Kamberský, Can. J. Phys. **48**, 2906 (1970).
[30]V. Kamberský, Czechoslovak Journal of Physics B **26**, 1366 (1976).
[31]C. Kittel and A. H. Mitchell, Phys. Rev. **101**, 1611 (1956).
[32]J. Kuneš and V. Kamberský, Phys. Rev. B **65**, 212411 (2002).

[33]M. Fähnle, J. Seib, and C. Illg, Phys. Rev. B **82**, 144405 (2010).
[34]B. Heinrich, R. Urban, and G. Woltersdorf, IEEE Trans. Magn. **38**, 2496 (2002).
[35]L. Berger, Phys. Rev. B **54**, 9353 (1996).
[36]Y. Tserkovnyak, A. Brataas, and G. E. Bauer, Phys. Rev. Lett **88**, 117601 (2002).
[37]T. Valet and A. Fert, Phys. Rev. B **48**, 7099 (1993).
[38]K. Dolui and B. K. Nikolić, Phys. Rev. B **96**, 220403 (2017).
[39]J. C. Rojas-Sanchez *et al.*, Phys. Rev. Lett **112**, 106602 (2014).
[40]J. Lindner, K. Lenz, E. Kosubek, K. Baberschke, D. Spoddig, R. Meckenstock, J. Pelzl, Z. Frait, and D. L. Mills, Phys. Rev. B **68**, 060102 (2003).
[41]M. J. Hurben and C. E. Patton, J Appl. Phys. **83**, 4344 (1998).
[42]K. Lenz, H. Wende, W. Kuch, K. Baberschke, K. Nagy, and A. Jánossy, Phys. Rev. B **73**, 144424 (2006).
[43]J. E. Hirsch, Phys. Rev. Lett **83**, 1834 (1999).
[44]J. Sinova, S. O. Valenzuela, J. Wunderlich, C. H. Back, and T. Jungwirth, Rev. Mod. Phys **87**, 1213 (2015).
[45]S. Qiao, W. Yan, S. Nie, J. Zhao, and X. Zhang, Aip Adv **5**, 087170 (2015).
[46]W. Zhang, W. Han, X. Jiang, S.-H. Yang, and S. S. P. Parkin, Nat. Phys **11**, 496 (2015).
[47]Y. T. Chen, S. Takahashi, H. Nakayama, M. Althammer, S. T. B. Goennenwein, E. Saitoh, and G. E. W. Bauer, Phys. Rev. B **87**, 144411 (2013).
[48]C.-F. Pai, Y. Ou, L. H. Vilela-Leão, D. C. Ralph, and R. A. Buhrman, Phys. Rev. B **92**, 064426 (2015).

Chapter 3
3. Experimental and Numerical Techniques

3.1 Introduction

Fabrication of samples in the microscopic length scales forms an indispensable part of spintronics and other allied branches of nanoscience and technology. For fundamental studies, it is desirable to implement the nanofabrication process which is simple, cost-effective and able to produce high-quality samples. One can chemically synthesize the sample using the so-called bottom-up approach as well as employing lithography and other physical processes usually categorized as the top-down approach, to obtain the desired nanostructures. Both approaches have their own merits and demerits as well. However, it is worth noting that as one prefers a good quality nano-device devoid of surface defects and chemical impurities, presence of which might greatly alter the electric, magnetic and other important physical properties, the top-down approaches are found to be more reliable techniques despite being slow and often, expensive. In this context, lithographic techniques with proper optimization can serve as one of the best choices for the precise fabrication of high-quality ordered arrays of nanostructures. In this chapter, we shall briefly discuss the deposition techniques for thin films such as magnetron sputtering and electron beam evaporation along with techniques for growing patterned nanostructures such as optical and electron beam lithography which has been employed to fabricate the ferromagnetic thin films, heterostructures and nanostructure studied in the thesis. The next important part of the study is to rigorously characterize the samples before proceeding towards the measurements of static and dynamic magnetic properties. X-ray diffraction (XRD), Energy dispersive X-ray (EDX), and X-ray reflectivity (XRR) are powerful techniques to characterize the elemental composition, structural phase and many other crystalline properties. On the other hand, scanning electron microscopy (SEM), atomic force microscopy (AFM) and magnetic force microscopy (MFM) are widely used for the reliable imaging of the topographical character and magnetic nature of the sample. Also, vibrating sample magnetometer (VSM) and static magneto-optical Kerr effect magnetometer (MOKE) have regularly been used to extract the static and quasi-static magnetic parameters. To probe the magnetization dynamics with a high spatio-temporal resolution, a time-resolved magneto-optical Kerr effect (TRMOKE) magnetometer, Brillouin light scattering (BLS) and Ferromagnetic resonance (FMR) spectroscopy techniques are very useful in time, wave-vector

and frequency domain, respectively. In the works described in this thesis, collinear and non-collinear TRMOKE have been extensively employed to excite and detect the spin dynamics directly in the time domain. Additionally, simulation in the micromagnetic framework can be extremely efficient to understand a real physical system well in advance. Several finite difference method (FDM) and finite element method (FEM) based micromagnetic simulation packages are available such as object-oriented micromagnetic framework (OOMMF), MuMax3, Boris, Ubermag, Nmag, VAMPIRE, LLG micromagnetic simulator etc. Most of these softwares come at no cost and can offer several advanced functionalities and helpful user support to simulate complex magnetic behaviour of a plethora of complicated nanostructured devices. Further post-processing and visualization of the data have been aided by a custom-built Matlab-based code called 'Dotmag' in our group. We would like to present the working principles of these techniques here in brief.

3.2 Fabrication Techniques of Thin Films and Heterostructures

There are quite a few useful techniques for the deposition of thin films in the nanoscale dimensions such as a) thermal evaporation, b) electron-beam (e-beam) evaporation, c) sputtering, d) molecular beam epitaxy (MBE) etc. In this section, we will briefly discuss two of the most important physical vapour deposition techniques- namely sputtering and e-beam evaporation.

3.2.1 E-beam evaporation

EBE[1] is a simple and robust technique for the deposition of metallic and dielectric or insulating materials in the form of a thin film, especially with a high melting point. Here the target material is placed in a water-cooled graphite crucible. An intense electron beam with high kinetic energy is generated via thermionic emission and the beam is guided employing several steering electric and magnetic fields to finally strike the target surface. This collision effectively converts the kinetic energy of the electrons to thermal energy (typically of the order of 1 eV) and vaporizes the target material. Now the atoms from the target usually travel to the substrate placed above at a reasonable distance (300nm to 1m). To ensure the perfect collision the mean free path of the vaporized atoms is enhanced by maintaining the pressure in the chamber at around 3×10^{-4} torr or lower. This makes the mean free path longer than the distance between the target surface and the substrate which allows the line of sight arrival of the target material on the substrate. This becomes particularly useful when a mask is involved to fabricate patterned structure. Usually, the sample holder is attached to a rotation motor to achieve

uniformity in the deposition.

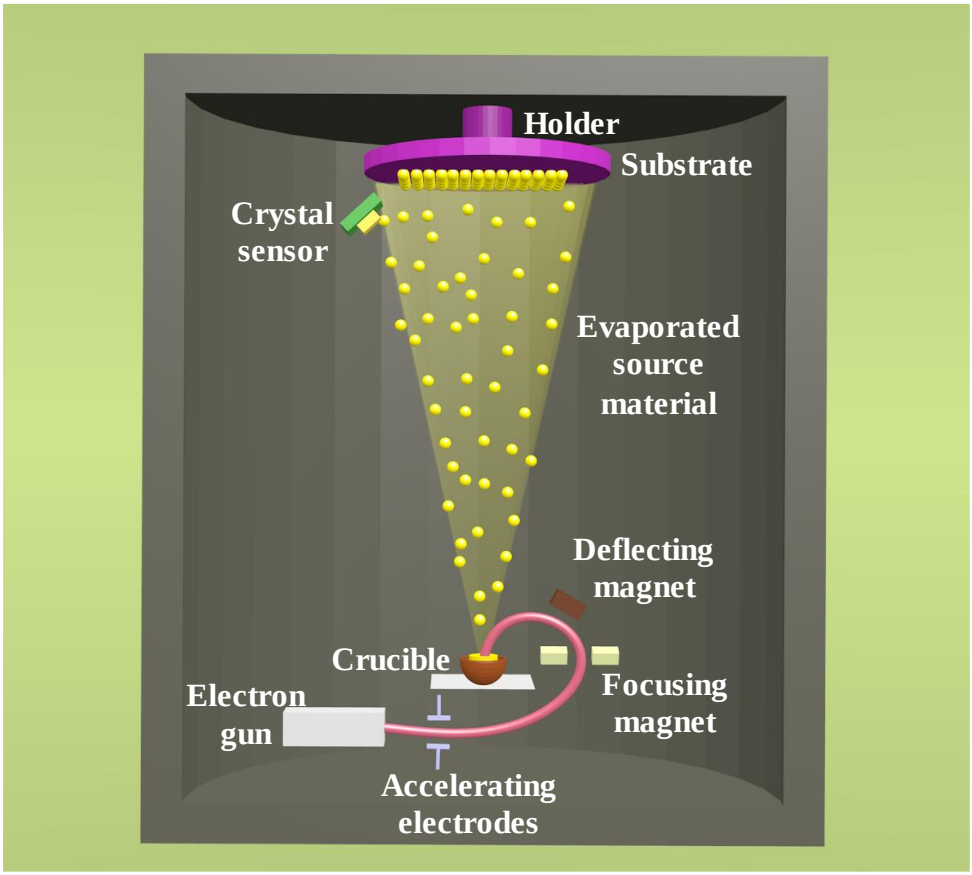

Figure 3.1: Schematic diagram of electron beam evaporation technique

A schematic of the EBE system is shown in fig. 3.1. It is robust enough to deposit ferromagnetic transition metals like Ni, Fe, Co and alloys such as NiFe, CoFe as well as nonmagnetic metals (like Au, Ti etc) and various oxide materials (such as TiO_2, SiO_2, Al_2O_3). The main chamber is often associated with a load-locked chamber to facilitate the seamless transfer of substrate or samples between the chambers.

3.2.2 Sputtering

Sputtering is a physical vapour deposition technique widely used for the deposition of nano and sub-nanometer scale thin film systems with very high quality[2]. Unlike thermal evaporation of EBE, sputtering is carried out under the presence of an inert gas atmosphere, usually Ar. Here target material serves as the cathode and the substrate is placed above the cathode and acts as an anode. The growth chamber is pumped out using a combination of rotary and turbo-molecular pumps to create a very high vacuum (of the order of 1×10^{-8} torr) and Ar gas is allowed to fill the chamber (around 05 to 0.1 mTorr). On application of a high voltage between the electrodes, the plasma is created where the neutral atoms, ions electrons and

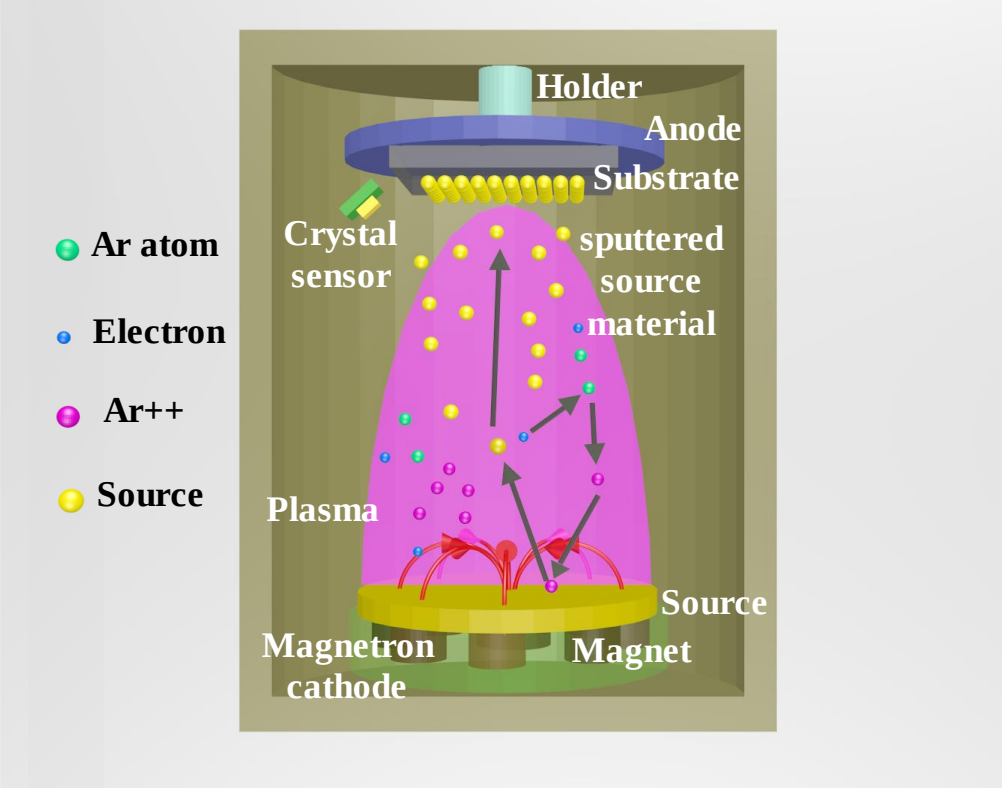

Figure 3.2: Schematic diagram of thin film deposition in magnetron sputtering technique

photons remain in a dynamic equilibrium. Now the free electrons present in the plasma experience a repulsive force from the negatively charged cathode and they become accelerated away from it. On colliding with the neutral Ar atoms multiple times in the plasma medium primary electrons knock off the outer shell electrons from Ar atoms and create a flow of Ar+ ions with secondary electrons. These Ar+ ions are accelerated towards the negatively charged cathode and upon striking the cathode they eject the target atoms and electrons. Target atoms then travel straight to the substrate, having the mean free path longer than the working distance. On the other hand, free electrons flow to the valence shell of the Ar+ ions and create neutral Ar atoms again along with high-energy photons and the dynamic stability of the plasma is maintained throughout. However, the diode sputtering techniques apart from being quite slow suffers from another serious drawback which is the overheating of the substrate and the possibility of structural damage caused by the repeated electron bombardment. This hurdle is overcome by the magnetron sputtering technique[3], Here, the back of the cathode is integrated with a special arrangement of the magnets to create the semicircular lines of force which is employed to efficiently trap the incoming electrons in a circular path and to reduce the velocity as well as to increase the probability of creating of more Ar+ ions.

Magnetron sputtering can be executed in both dc and rf potentials. While dc offers a cost-

effective method of deposition of conducting materials such as metals, it might cause serious problems like polarized charge accumulation, non-uniform film deposition etc. RF sputtering can be used to bypass the problem of charge building up for the deposition of electrically insulating material. RF plasma is more uniform than its dc counterpart and is sustainable at a comparatively lower pressure ensuring more efficient deposition. Nevertheless, it suffers from the issue that the growth rate becomes considerably slower because of the lack of secondary electrons near the target surface.

3.3 Fabrication Techniques of Patterned Nanostructures

Lithography is a widely used process to precisely fabricate any 2D or even 3D structures in micro to nano-dimension on a substrate. It is essentially scanning an electron-sensitive material with high-power radiation. Depending upon the nature of radiation there are several choices for the lithography process such as: 1) photolithography, 2) electron beam lithography (EBL), 3) x-ray and 4) ion-beam lithography etc. Here we shall present the working principles for EBL in short.

3.3.1 E-beam lithography

EBL[4] is an extremely powerful technique to grow submicron to nanoscale feature patterns extensively used for controlled fabrication of long-range periodic arrays on top of a suitable substrate. The EBL works on a similar principle to that of a photolithography technique, nevertheless, the much shorter wavelength of high-energy electrons is useful to achieve a shorter feature size. Moreover, the thinner resist pattern aids this process[5]. In this process, a specially cleaned substrate is spin coated with EBL resist such as PMMA and MMA polymer. The coating parameters are wisely chosen keeping the required thickness of the resist in mind. The pattern is first drawn with the help of Auto CAD (or, any other similar designing software available). Afterwards, the focused electron beam is used to scan the system with the pre-defined writing parameters (electron energy in keV, beam current and dose). After ‘writing’, the system is then allowed for development using a suitable solvent according to the resist type followed by cleaning in IPA and distilled water. For PMMA/MMA bilayer resist MIBK (methyl isobutyl ketone): IPA (isopropyl alcohol)=1:3 mixture can serve as a good solvent and ma-D developer can be the best choice for ma-N 2405 resist. Finally, the target material is deposited as per the requirement using sputtering of EBE and unexposed resist is lifted off using ultra-sonication in acetone solvent. Despite being an expensive and time-consuming top-down technique, the higher resolution is what gives EBL an edge over the other techniques in

fabricating fine-quality nanostructures over a long range.

3.3.2 Etching

In nanofabrication, the process of removal of the unmasked area of the sample is referred to as etching. Depending on the phase of the etchant, etching can be done in wet or dry mode. The wet etching or liquid phase etching which mostly uses HF acid or KOH as an etchant chemical can give isotropic removal of resist. However, with the invention of VLSI technology, dry etching is preferred such as focused ion beam (FIB) milling[6], ion milling[7], plasma etching etc. Whereas physical etching depends on the high kinetic energy of the ions or electrons to knock off the surface atoms, gaseous phase etching depends on the chemical reaction between the target surface and etchant material offering high material selectivity but comparatively poor unidirectional etching. Therefore, a physio-chemical combined process such as plasma reactive ion etching (RIE) offers great material selectivity and highly anisotropic vertical etching.

3.4 Characterization Techniques

Even after deploying state-of-the-art nanofabrication techniques, the structures can vary a lot from their targeted physical properties such as shape, size, thickness, and elemental chemical composition because of various factors ranging from the ambient condition to the lithography, film deposition and lift-off parameters. These can enormously alter the physical and chemical properties of the system under study. Moreover, poor preservation and mishandling can cause quality degradation of the samples to an extent. Therefore, characterization plays a vital role to achieve greater and deeper insights into a system. The working principles of the characterization techniques used in this thesis are presented here.

3.4.1 Optical Microscopy

Optical microscopy is one of the most basic yet useful tools which is used to observe systems with dimensions ranging from a few μm to hundreds of nm. The powerful magnification (10-100X) of the object under observation is achieved by the combined arrangement of objective and eyepiece lens systems. A visible lamp serves as the light source for the microscope. The sample is placed on an *x-y-z* scanning stage to conveniently scan through the different areas under interest. During the works performed in the thesis, Olympus MX51 has been used.

3.4.2 Scanning Electron Microscopy (SEM)

SEM is the most commonly used technique for visualizing nanoscale objects and pattern morphology based on the interaction of high-energy electron beams with matter.[8] Because of

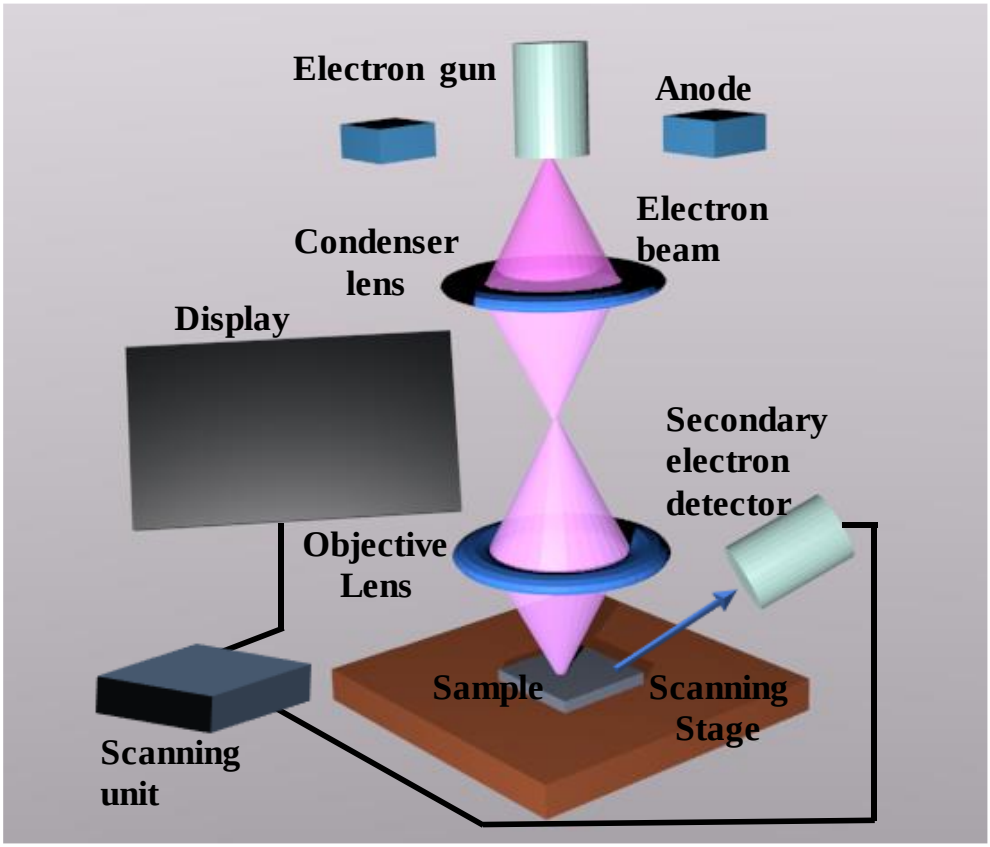

Figure 3.3: Schematic diagram of scanning electron microscopy (SEM) technique

a shorter de Broglie wavelength of electron waves in comparison to light waves (typically 550 nm) SEM can offer tremendous resolving power coupled with a magnification of 300000 times. A typical SEM consists of an electron source, a couple of condenser electromagnetic lenses, a scanning coil or deflector plates, an electron detector and a sample chamber with vacuum arrangements. Electron beams are generated from the cathode using the standard thermionic emission technique by passing a large current through the W coil or using the field emission method where W wires are placed under a high electrical potential gradient. The beam is then allowed through multiple sets of electromagnetic condenser systems equivalent to lenses in optical analogue. Afterwards, scanning coils or deflecting plates are used to guide the sharp beam to incident on the sample surface and the raster scanning method is adopted to create a 2D image of the object. On striking the sample and penetrating to a few micrometres, the primary electrons lose their kinetic energy and generate secondary electrons, Auger electrons, and backscattered electrons along with continuous and characteristic X-rays. In SEM, the density of the secondary electrons with respect to the incident electrons is probed by the detectors to create a 2D image of the selected area of the sample. It is important to note that to avoid any image artefacts or distortion caused by the surface charge accumulation the sample

under SEM must have a conducting surface. For nano-devices or patterns made up of non-conducting material, a layer of conducting material (such as Au) is applied on top of it before allowing it for SEM.

3.4.3 Atomic and Magnetic Force Microscopy (AFM & MFM)

AFM is a type of scanning probe microscopy which is a very effective technique to study the surface topography and morphology of nanofabricated samples[9,10]. Here, the various types of forces such as the van der Waals force, adhesion, cohesion, electrostatic force etc. working between the probe and the sample are measured to produce a high-resolution image. The probe consists of two parts; one cantilever and a sharp probing tip with strong coating materials such as Co-Cr, Pt-Ir or diamond. The sample is placed on the sample plate which is connected to high precession piezoelectric actuators qualified to produce small oscillatory movements. During the movements, the forces acting on the tip vary in magnitude causing the vertical as well as horizontal deflections of the cantilever. A laser beam is made to get reflected from the top of the cantilever falling on a sensitive photodetector. The differences between the signals

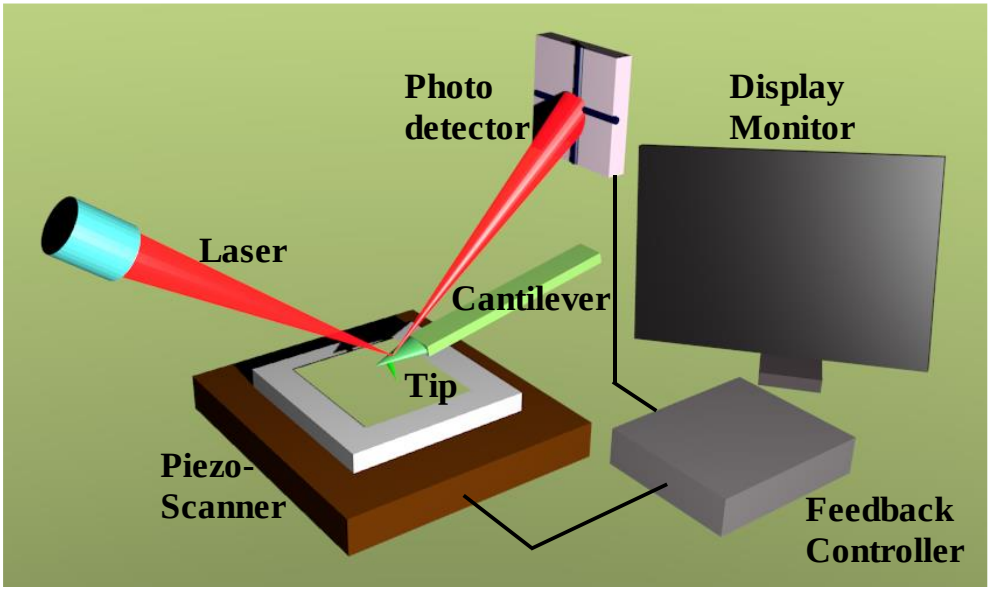

Figure 3.4: Schematic diagram of atomic force microscopy (AFM) technique

of different segments of the photodetector provides an estimation of the angular deflections of the cantilever. A raster scanning over the sample of a few μm^2 gives the 2D topography for the sample under characterization. For a magnetic sample, MFM[11] characterization can give significant insights into the static magnetic states and can often predict possibilities of intriguing spin configurations like skyrmions. Here, a magnetic tip with high coercivity is used and the magnetic interaction is measured between the probe and the sample to produce a phase

image. Both static and dynamic modes of operation can be utilized for the procurement of MFM images. In characterizing the surface topography of the samples discussed in this thesis, Veeco (diInnova) AFM system has been used.

3.4.4 X-ray Diffraction (XRD)

XRD is often regarded as the most powerful technique for material characterization[12,13]. X-rays having wavelengths comparable to the lattice parameters of most solid-state materials, suffer diffraction by the periodic atomic arrangement in a crystal lattice. When an X-ray beam having wavelength λ is incident on a plane of atoms, usually known as the "Bragg plane" the reflected beam is collected by a detector showing constructive interference at a suitable angle and this reflection is parameterized by the famous Bragg's law given by:

$$2d_{hkl}sin\theta = n\lambda \tag{3.1}$$

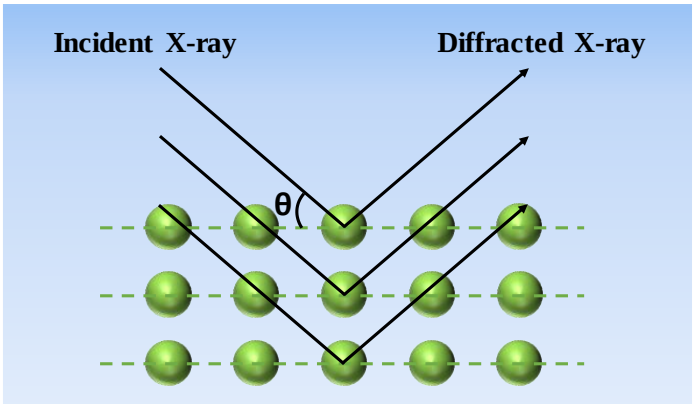

Figure 3.5: Schematic diagram of X-ray diffraction (XRD) technique

From the initial knowledge of incident wavelength (λ) setting an nth order diffraction pattern for glancing angle θ, the distance between the plane having identical Miller indices (d_{hkl}) can be known and thereby lattice spacing of a particular compound can be calculated. In usual $\theta - 2\theta$ geometry, the beam source is kept fixed and the detector is moved twice the angle as compared to the sample. Finally, the intensities of the diffracted X-ray are plotted as a function of 2θ and the pattern is compared with standard d_{hkl} values for different elements and compounds from the ICSD database to identify the structural phases. Several other methods of scanning such as rocking curve, $\theta - \omega$ are also very useful for XRD scanning depending upon the requirement of the characterization. Apart from the phase and lattice spacing, various other crucial crystalline parameters like crystallite size, lattice strain, lattice imperfections etc. can be extracted from the XRD scans. In the experiments described in the dissertation, both "Rigaku Smartlab" and "PANALYTICAL EXPERT PRO" X-ray diffractometers have been

utilized.

3.4.5 X-ray Reflectivity (XRR)

XRR provides another powerful characterization tool especially useful for any nanoscale thin film and multilayer system[14]. It is a completely non-invasive technique and can give a fairly accurate estimate for individual thickness, electron density and interfacial roughness for the constituent layers of a multilayered heterostructure system. Unlike XRD, a specular reflection condition that is grazing angle = detector angle is used and the grazing angle is usually kept very small (approximately up to 4°) to expose more surface of the sample. Here, the sample is kept fixed and the glancing angle, as well as the detector angle, is varied at the same pace to obtain specular reflectivity.

The working principles of XRR is strongly dependent on the electron density of the material which primarily determines the refractive index of the sample for a particular wavelength of incident radiation. For X-rays, the refractive index of the sample is slightly less than 1, i.e., a solid continuous medium behaves as a rarer medium to X-rays with respect to the air. As a consequence, the X-ray having an angle of incidence smaller than the critical angle suffers total internal reflection. However, on increasing the angle slowly X-ray becomes able to penetrate through the surface of the sample and from each of the constituent layer interfaces, it suffers multiple reflections. With an increasing angle, the intensity of the reflection decreases as θ^4. The reflected beam of X-rays from each layer again merges to create constructive and destructive interference patterns widely known as Kiessig fringes of Kiessig oscillations. The amplitude and period of Kiessig fringes are directly correlated to the interlayer electron density contrast and layer thickness. Also, the intensity decay rate at a higher angles is caused mainly by the surface roughness whereas both the surface and interface roughness contribute to the decay of reflectivity intensity at the lower angles.

The quantitative interpretation of an experimental XRR requires a bit more analysis. Firstly, a layer structure model is proposed and using recursive Parratt formalism or distorted wave Born approximation (DWBA) a theoretical XRR curve is calculated. Afterwards, a nonlinear least square fitting method is adopted to obtain the optimal value for film thickness, interfacial roughness and electron density. There are a number of open-source fitting programs available for XRR analysis. We have used “Reflex 44”[15], a Matlab environment-based code for the analysis of XRR data presented in this thesis.

3.4.6 Energy Dispersive X-ray Spectroscopy (EDX)

EDX is an indispensable tool to characterize the chemical elemental composition in a sample. It is usually attached to a FESEM system for convenience. The working principles of EDX essentially rely on the characteristic X-ray generation from a particular element. As high-energy X-rays from sources knock off some of the inner shell electrons from the element, electrons from the nearest and next nearest shells fill the vacancy and the difference in energy is emitted as characteristic X-ray radiation. This gets absorbed by Li or Si crystal in the detector to produce equivalent electrical voltage via ionization. The elements are identified from the peak energy values and the relative intensities of the peaks provide the atomic percentage of individual elements. In this thesis, an EDX system from EDAX attached with FEI QUANTA 200 SEM has been utilized.

3.4.7 Reflection High Density Electron Diffraction (RHEED)

RHEED is one of the unique techniques to carry out investigation of structural order of thin films heterostructures[16,17]. It is surface sensitive and can provide real time measurement of surface topography of the film, grain size, epitaxial nature etc. during the growth. Principle of RHEED essentially relies on imaging of the electron scattered from the sample surface. First, a beam of high energy electrons is passed through an aperture and is approximately focused to 0.1 mm spot by electromagnetic lensing. A number of deflection coils are used to steer the beam to incident on sample surface at a small grazing angle (0.5-6°). This makes the spot very large on the sample and allows it to capture more surface information. The high energy electron beam suffers diffraction at the atomic planes of the material and are finally arrive at a fluorescent screen which serves as the detector inside the deposition chamber. The RHEED pattern recorded in such a screen can be captured employing a CCD camera placed outside the chamber. Depending upon the nature of the surface under investigation, one may obtain spots, clear streaks, modulated streaks etc. as RHEED pattern. The spatial resolution of the image is dependent on coherence length of the electron beam in longitudinal and transverse direction which are given by $l_L = \lambda E / \Delta E$ and $l_T = \lambda / (\sqrt{2}\Delta\theta)$, where ΔE and $\Delta\theta$ represent energy spreading and divergence angle of the beam.

3.4.8 Vibrating Sample Magnetometry (VSM)

VSM is a popular technique to study the static magnetic properties of a solid specimen[18]. It essentially uses Faraday-Lenz's principle which states that the changing magnetic flux associated with a loop generates electrical voltages. That is,

$$e = -n\frac{d}{dt}\left(\vec{B}.\vec{A}\right) = -n\mu_0 A\frac{dM}{dt} \tag{3.2}$$

Where, $B = \mu_0(H + M)$ gives the magnetic induction vector and A is the area of the coil.

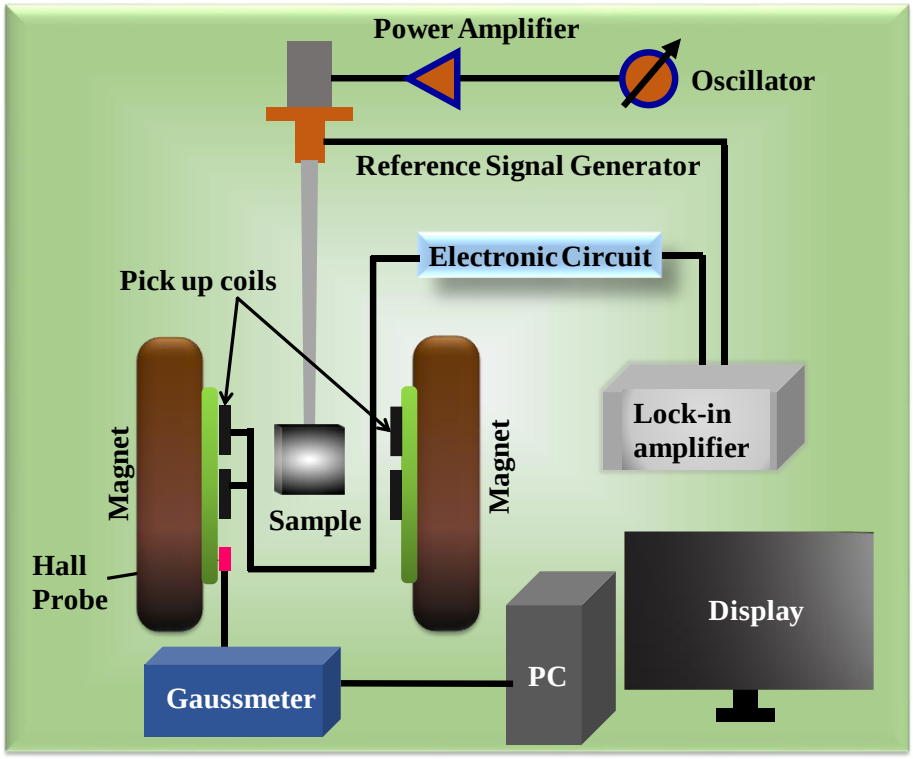

Figure 3.6: Schematic diagram of vibrating sample magnetometry (VSM) technique

In VSM, the sample is attached to a piezoelectric transducer stage connected to a vertical quartz/ plastic rod placed in a uniform magnetic field of constant magnitude. A pick-up coil is placed in the vicinity of the sample. A sinusoidal current passing through the piezoelectric transducer creates a vertical oscillation in the sample and as a result, there exists a finite rate of change of stray field of the magnetic specimen which in turn, generates the electrical voltages in the pick-up coil. This voltage is amplified and detected in a lock-in amplifier where the output from the piezoelectric signal is used as the reference. Using a standard reference specimen, magnetization is calculated from the lock-in voltage and this technique is sensitive up to 10^{-5} emu. VSM is typically employed to measure the hysteresis behaviour of sample magnetization. Sometimes it comes with the set-up attachments to carry out the characterization at elevated and reduced temperatures as per the requirements. Our works described in the thesis have been carried out in the "Lake Shore" VSM system.

3.4.9 Static Magneto-Optical Kerr Effect (S-MOKE)

The static MOKE employs the magneto-optical Kerr effect to understand the magnetic

behaviour of a specimen. It is particularly very useful for a tiny and delicate sample having a very low magnetic moment confined in a localized space. From static MOKE, Kerr rotation as a function of the applied external magnetic field is probed which can be used to measure the hysteresis nature of various types of nanofabricated samples. Here we provide a description of the custom-built static MOKE set-up used for our measurements. The integral components of a static MOKE set-up include: i) A continuous wave (CW) laser, ii) an attenuator, iii) a Glan-Thompson polarizer, iv) two highly reflecting mirrors, v) two plano-convex lenses for collimating system, vi) two convex lenses or two long working distance microscope objective (20X), vii) an optical chopper/ a photo-elastic modulator, viii) an optical bridge detector (OBD), ix) a white light source, x) a CCD camera, xi) an electromagnet, xii) a lock-in amplifier and xiii) a computer for data acquisition and visualization.

In our set-up, a He-Ne CW laser with a wavelength of 632 nm is used as a source. After passing

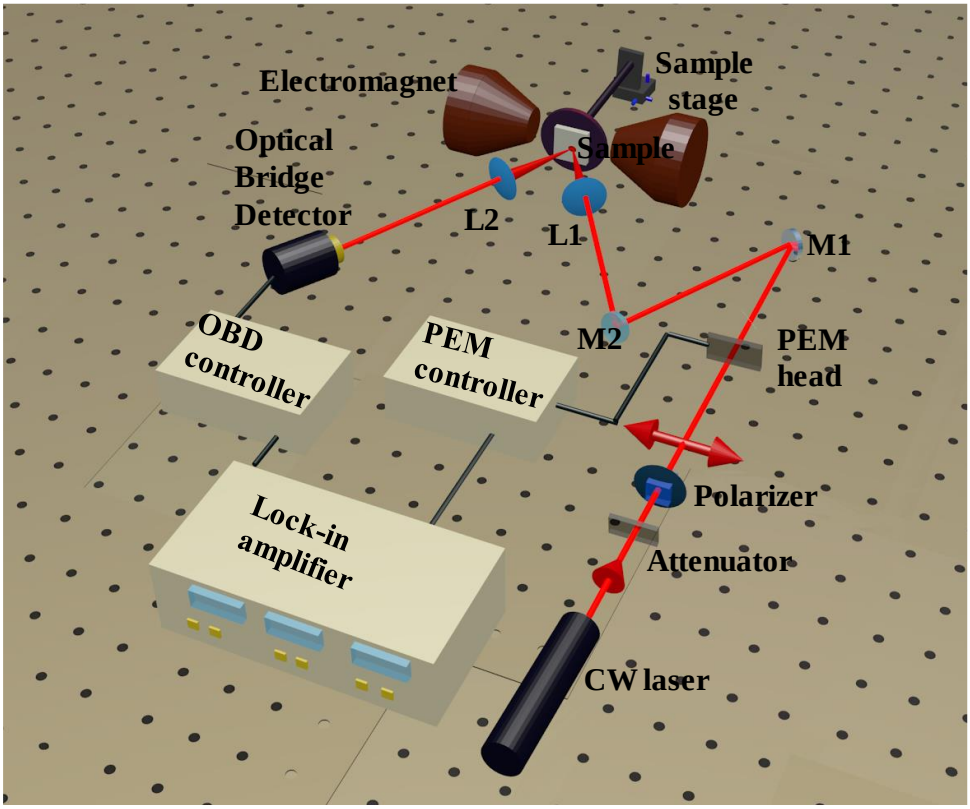

Figure 3.7: Schematic diagram of static magneto-optic Kerr effect measurement (MOKE) setup

through the Glan-Thompson polarizer, the ray becomes s-polarized which then faces two highly reflecting mirrors used for the alignment of the beam. Afterwards, the beam passes through a convex lens (L1) and finally falls on the sample. The magnetization of the sample interacts with the light and via MOKE, it alters the polarization angle of the reflected light. The reflected beam from the sample surface is again passed through another lens (L2) and is

collected at the centre of the OBD connected to the lock-in amplifier. Before collecting the beam in the detector, a PEM head is placed in the path of the ray, which modulates the intensity of the beam and provides the reference signal to the lock-in amplifier for phase-sensitive signal detection to be possible under a noisy environment. In this arrangement, an optical chopper can also serve as an alternative to PEM and can be used for the intensity modulation. The sample is usually placed on a movable x-y-z stage in between the pole pieces of a powerful electromagnet.

Although the abovementioned arrangement is capable enough to perform static MOKE characterization of thin films and magnetic multilayer heterostructures, the set-up requires slight modification when the measurement of a nano-patterned sample is concerned. In this case, a collimating lens system becomes necessary and the parallel beam falls on the sample after passing through a 20X microscope objective instead of the lens L1. Similarly, the lens L2 is also replaced by another identical microscope objective. Moreover, a white light source and a CCD camera are installed in the beam path for viewing different areas of the patterned structure which makes the measurement system extremely powerful and convenient for the user.

3.5 Experimental Techniques for Ultrafast Magnetization Dynamics

Magnetization dynamics can take place from femtosecond to nanosecond timescale. Different experimental tools have been developed over the years in order to achieve a sound fundamental understanding of the topic. The way these techniques tend to explore the dynamics differ strikingly from one another. For example, the conventional ferromagnetic resonance (FMR) spectroscopy or the modern vector network analyzer (VNA) based broadband FMR (VNA-FMR) serves as a convenient all-electrical technique to explore the magnetization dynamics in the frequency domain. On the other hand, Brillouin light scattering (BLS) is another popular optical detection technique based on the interaction of spin waves and photons and is extensively used to determine the spin wave dispersion relation and the corresponding magnon band structure. However, time-resolved magneto-optical Kerr effect (TRMOKE) is probably one of the best experimental tools to probe the ultrafast magnetization dynamics directly in the time domain[19]. The combination of sub-micron spatial resolution and ultralow temporal resolution (40-100 fs, depending upon the laser source cross-correlation) made this technique extremely powerful for the investigation of magnetic nanostructures. The modern, all-electrical variant of this technique being completely non-invasive in nature, eliminates the multistep lithographic process in the fabrication of waveguide structures required for electrical

measurements. Moreover, the advent of attosecond lasers offers the TRMOKE system higher temporal resolution suggesting enormous possibilities for exploring novel phenomena. In the works described in this thesis, we have employed two types of custom-built TRMOKE set up:

i) TRMOKE microscope set up in collinear geometry: based on femtosecond oscillator.
ii) TRMOKE set up in non-collinear geometry: based on the amplified femtosecond laser.

Below, we describe the important components as well as the working principles for these two techniques.

3.5.1 Time-Resolved Magneto-Optical Kerr Effect Microscope

The custom-made TRMOKE microscope that has been employed to measure the magnetization dynamics works present in this thesis, is an extremely complex and unique measurement set-up[20,21]. Before describing the working principle of the set-up, we are going to provide a brief idea about the crucial optical components of the set-up with their basic functions for the convenience of the reader. In a nutshell, the femtosecond oscillator-based TRMOKE microscope is comprised of the following prime segments:

i) **Laser Unit**: Containing an integrated diode laser and a diode pumped solid state (DPSS) unit called "Millennia eV" (Spectra-Physics), Ti: Sapphire Femtosecond oscillator unit called "Tsunami" (Spectra-Physics) and a second harmonic generator (SHG) (Spectra-Physics).
ii) **Temporal Delay generator**: A retroreflector panel mounted on a mechanical delay stage and the corresponding motion controller unit
iii) **Steering Optics**: This part contains several highly reflecting dielectric mirrors, a Glan-Thompson polarizer, neutral density filters (or attenuators), collimating lens duo, beam splitters and a microscope objective.
iv) **Movement stages**: A linear stage for the microscope objective, a manual x-y stage, and a piezoelectric x-y-z scanning stage for the sample with a controller unit.
v) **Visualization arrangement**: A CCD camera, a white light and a glass filter
vi) **Detection Assembly**: Comprising an OBD, an optical chopper with a chopper controller, two spectral filters and two lock-in amplifier units connected to a desktop.

We present here a short description of working principle of Millennia eV, Tsunami and SHG.

3.5.1.1 Millennia eV

"Millennia eV" (brand: Spectra-Physics; Company: Newport Corporation)[22] is a diode-

pumped continuous-wave visible laser system. It is an upgraded version of earlier available Millennia and Millennia pro series DPSS lasers which required external diode lasers and a power head. Here, the diodes and the high-quality fiber optic cables are integrated with the laser X-cavity of the DPSS laser and the controlling microprocessor with associated electronic components in a sealed box making the system rugged, compact and reliable for long-term stable performances. In Millennia eV, the diode module ('FCbar") produces the initial output laser which is then used to pump the vanadate crystal (Neodymium doped Yttrium ortho-vanadate Nd: YVO_4) serving as the gain medium for the laser, placed in a folded optical cavity resonator. The gain medium is a four-level laser system and the lasing at a wavelength of 1064 nm is achieved when an electron transition takes place from $4F_{3/2}$ to $4I_{1/2}$ levels. The 1064 nm radiation is confined and allowed to resonate within the optical cavity by a telescopic arrangement. It focuses the beam on the active medium through a specially chosen dichroic mirror which is highly transmissive for a diode pump laser but highly reflective at 1064 nm.
For the purpose of frequency doubling a non-linear crystal of lithium triborate (LBO) is employed within the cavity of Millennia. It accepts the intra-cavity radiation of 1064 nm and converts it to 532 nm. The large acceptance angle of LBO makes it capable of withstanding a slight misalignment in the X-cavity. However, for stable performance at 532 nm, a compact regulating oven is used for maintaining the crystal temperature. The frequency-doubled radiation is then allowed to pass through another dichroic output coupler to a feedback arrangement consisting of a beam splitter and a photodiode which collects the beam and sends a part of it back to the pump laser driver. The dichroic mirror allows the 532 nm beam to exit the cavity while reflecting the 1064 nm back to it. Outside the cavity resonator, a programmable shutter is there to ensure beam blocking or opening on demand. Millennia eV is connected to a PC and the user can operate it via a simple graphical-user-interface based proprietary software.

3.5.1.2 Tsunami

"Tsunami" (brand: Spectra-Physics; Company: Newport corp.)[23] is a mode-locked Ti: Sapphire (Ti: Al_2O_3) laser system which employs the output 532 nm CW laser from Millennia eV as the input radiation and is able to produce near-infrared (690-1080 nm) variable pulsed laser as an output beam. The Tsunami laser head contains titanium doped sapphire rod as the active medium for lasing and a very complex cavity resonator. The requirement of a long cavity in order to achieve the optimal repetition rate (80 MHz) is met by designing a space-efficient 10-mirror folded cavity. Nevertheless, this complicated design might suffer from astigmatism

which is virtually eliminated by choosing the length of the active medium and the angle of incidence accurately. For long-term stable performance, the laser head is purged with ultrapure nitrogen gas removing the vapour and dust particles. Moreover, a chiller unit is employed to keep the temperature of the gain medium maintained.

In Tsunami, active mode locking is ensured by passing the laser through an acoustic-optic modulator (AOM). AOM is a quartz crystal with two highly polished surfaces parallel to the direction of laser propagation. Either of these two surfaces is driven at an rf frequency by a piezoelectric transducer generating an acoustic wave, which on reflecting from the other surface interferes and eventually creates a standing acoustic wave serving as a time-dependent acoustic diffraction grating. There is a possibility of a mismatch between this rf frequency and the cavity length which is solved by driving the rf source from the laser cavity so that any change in the cavity length also changes the rf signal frequency accordingly ensuring they are never out of synchronization. This technique is known as regenerative mode-locking. It is important to note that the temporal width of the mode-locked pulse varies as the inverse of the number of modes that are locked in phase whereas, the intensity of the output scales as the square of this number.

The positive pulse chirping and group velocity dispersion among the different wavelengths is compensated by a four-prism sequence arrangement. By tuning the opening of the slit between the prisms the output pulse width can be tuned.

3.5.1.3 Second Harmonic Generator (SHG)

SHG 3980 (Spectra-Physics; Newport Corp.)[24] uses a barium beta borate (BBO) crystal for a second harmonic generation. It receives the 800 nm beam from Tsunami and generates its frequency-doubled counterpart. BBO crystal can provide certain advantages over other non-linear crystals (like LBO) such as:

i) Wide transmission range (190-3500 nm).
ii) Coverage of broad operating (phase matching) range (690 nm to 1090 nm).
iii) No compensating crystal is necessary; a single crystal is insufficient to match the phase over the operating range.
iv) Large conversion efficiency.
v) High optical homogeneity ($\delta\eta \sim 10^{-6}$ /cm).
vi) Higher damage threshold.
vii) It also minimizes the pulse broadening occurring due to group velocity dispersion.

For a normal refractive medium, the polarization is usually written as a linear function of the electric field. However, in a non-centrosymmetric crystal, it can depend on the higher powers of the electric field leading to a power-series expansion of polarization. When a light of frequency ω is absorbed by such a non-linear optical medium, the dipole oscillations radiate the light of 2ω and higher harmonics along with the principal wavelength. BBO being an excellent non-linear optical medium with great optical and mechanical properties is employed in current SHG systems.

The conversion efficiency is inversely proportional to the beam cross-sectional area. Therefore, the beam waist is further decreased by a telescopic lens arrangement. Controlling mirrors employed are attached with external micrometre screws to tune the incidence angle of the input beam on the surface of the BBO crystal so as to produce maximum power. A beam splitter prism separates the second harmonics (SH) from its fundamental and routing mirrors steer the SH beam to get diffracted through a pair of Littrow prisms to minimize the distortion in beam shape as well as any horizontal displacement. Both the SH beam and the fundamental are allowed to exit through two separate output windows.

3.5.1.4 Description of the Set up (Collinear pump-probe geometry)

The TRMOKE microscope experimental set-up[21,25] is placed on top of an optical table (Newport RS 4000) which is connected with 4 hydraulic legs attached to a silent air compressor

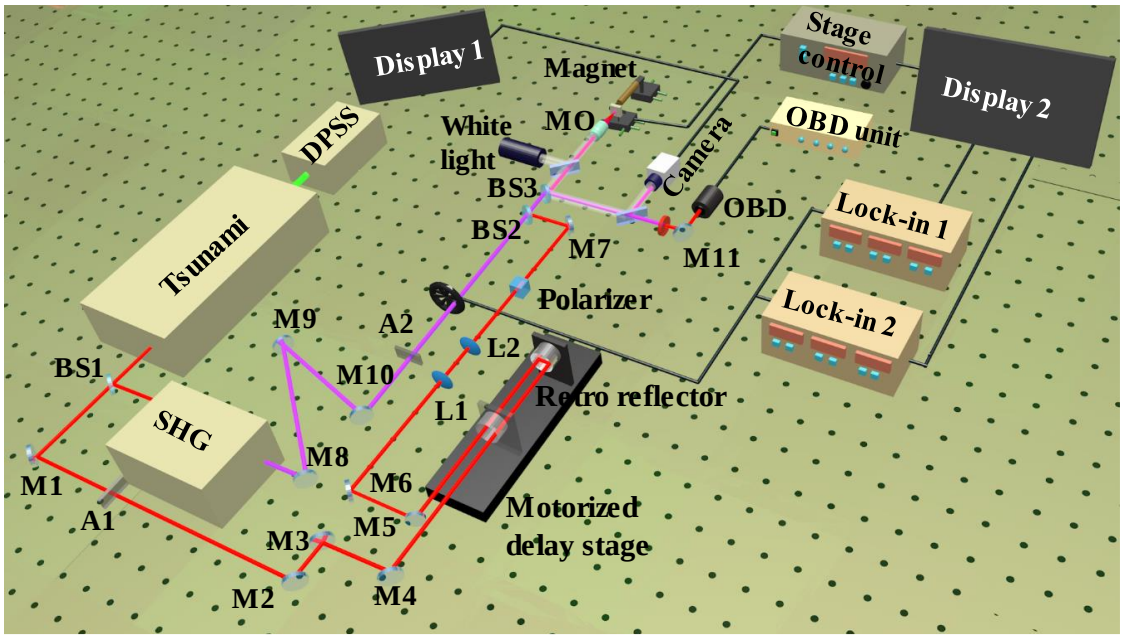

Figure 3.8: Schematic diagram of TRMOKE setup with microscope and collinear pump probe arrangement

to provide the system broadband as well as tuned damped vibration isolation. The adjacent schematic diagram shows the configuration of the setup. A 532 nm green CW laser from Millennia eV (peak power: 10 W: usually operated at 8 W) enters the Tsunami. The Ti: Sapphire gain medium powered with the regenerative mode-locking technology produces an 800 nm pulsed laser with spot size ~2 mm, an average output power of ~2 W and a repetition rate of 80 MHz. The s-polarized (horizontal) fundamental beam is passed through a 70:30 beam splitter and the stronger part, after getting frequency doubled (λ = 400 nm) by the SHG emits with a temporal width of ~100 fs and power ~200 mW. The weaker part of the fundamental (probe, hereafter) is guided using a set of dielectric mirrors before entering the retro-reflector placed on a motorized programmable delay stage (Newport ESP 301). After the delay, the probe faces a pair of lenses in telescopic arrangement to proceed through a Glan-Thompson polarizer and is steered by another family of 3 dielectric mirrors to finally incident on a 50:50 beam splitter, known as beam combiner.

On the other hand, the beam from the SHG (hereafter, 'pump') is also guided by several dielectric mirrors in its path. A spectral filter is used to eliminate the residual fundamental from the SGH beam which would otherwise have created noise in the output signal. A linear dielectric neutral density filter is employed to attenuate the power of the pump beam as per the requirement. Finally, the beam is passed through a mechanical chopper modulating it at 2 kHz which collects the reference signal for phase-sensitive detection. At the beam combiner surface, both the pump and probe combine at 90° to each other and the combined beam is made to incident normally on the back aperture of a microscope objective (40X, 0.65 numerical aperture). The sample is usually attached to a holder connected to the piezoelectric x-y-z scanning stage placed right after the microscope objective. The pump and probe beam pass through the objective in a collinear manner and fall on the sample. The distance of the objective from the sample surface is carefully chosen with the help of a linear stage screw so that the probe beam remains tightly focused with a spot size of ~800 nm. However, due to chromatic aberration, the pump beam remains slightly defocused with a spot size of ~ 1μm. A visualization arrangement is also set up using white light, a plane glass slide and a CCD camera. The white light after getting back reflected from the sample comes out through the MO and is guided to CCD connected to the desktop monitor.

The back reflected pump and the probe beam also exit through the MO and are steered towards to the OBD. Before allowing to the OBD, a spectral filter is employed in the beam path to eliminate the pump beam from the mixed signal. The OBD construction is discussed in the

static MOKE section. It is connected to the controller and signals from (A-B) and (A+B) ports are sent to the lock-in amplifiers (SRS 830). For a precise estimation of Kerr rotation, (A-B) signal is calibrated first and then set to zero in a multimeter reading for a negative delay value by adjusting the screw attached to OBD. A well-defined rigorous process of optical alignment is executed in different segments of TRMOKE set up such as retro-reflector, probe and pump beams, OBD etc. for achieving reliable time-resolved precessional Kerr oscillation data.

3.5.2 Non-Collinear Time Resolved Kerr Effect Magnetometer

The custom-made non-collinear TRMOKE set-up we have used to measure the ultrafast magnetization dynamics present in the dissertation is another sophisticated measurement set-up. Here we are going to provide a brief about the crucial components as well as the working principles of the setup in a nutshell. The femtosecond amplifier-based TRMOKE magnetometer is comprised of the following units:

i) **Laser Unit**: All-in-one integrated amplified laser system (brand: Libra; Company: Coherent)[26] consisting of the following sections: diode lasers, diode pumped solid state laser (Verdi) coupled with a mode-locked ultrafast oscillator (VPUF) (Vitesse, in compact form) and diode-pumped Q-switched laser (Evolution).

ii) **Temporal Delay generator**: A retroreflector panel mounted on a delay stage and corresponding motion controller unit

iii) **Steering Optics**: a number of highly reflecting dielectric mirrors capable of withstanding high pulse energy, lenses and circular/ linear neutral density filters (or attenuators).

iv) **Detection Assembly**: two silicon photodiode detectors, a Glan-Thompson polarizer, an analyzer crystal, an optical chopper with a chopper controller and two lock-in amplifier units connected to a desktop.

We present here a short, functional description of laser units integrated within Libra-namely Vitesse and Evolution. Afterwards, we shall also discuss the principle of chirped pulse amplification and SHG.

3.5.2.1 Vitesse

This segment of Libra consists of essentially three parts: the diode system, diode pumped solid state laser called Verdi and Verdi pumped ultrafast oscillator (VPUF) system which we will describe here[27].

i) **Diode system:** This part consists of two laser diodes, electrical circuits, a power box

and an air cooling system with computerized power and a current monitor. The diodes produce CW laser and the output is carried via fibre optical package (FAP) modules. Proper heat sinks and cooling fans are employed to maintain the temperature of the FAP modules to achieve efficient laser output.

ii) **Verdi:** It is essentially a single-frequency ring cavity resonator with Neodymium Vanadate (Nd: YVO_4) as the active medium with an LBO crystal for intra-cavity frequency doubling. The resonator receives the 808 nm CW laser from the FAP modules and converts it to strong line emission at 1064 nm. The optimum temperature of vanadate is maintained to minimize thermal focusing and astigmatism. The LBO crystal maintained at 150°C acts as an output coupler also which after generating the frequency-doubled counterpart (532 nm) lets the beam exit the resonator cavity.

iii) **VPUF:** Verdi pumped ultrafast Ti: Sapphire oscillator, called VPUF for short is the mode-locking unit inside the compact Vitesse system. It is pumped by the 532 nm CW output from Verdi. VPUF relies on Kerr lensing based passive mode locking system. Due to the non-linear optical Kerr effect, the high-intensity laser beam with a Gaussian power distribution across the profile experiences a gradient of refractive index from the centre to the edge while passing through the active medium. Therefore, the Kerr lensing acts as an artificial saturable absorber for the beam without the presence of any real saturable absorber leading to self-mode-locking. For stable mode-locking, the cavity is made unstable for CW operation by positioning an aperture which drives the process further. Now the group velocity dispersion (GVD) causes spectral chirping and the self-phase modulation caused by the self-focusing introduces temporal chirping and pulse broadening. Multiple Fabry-Perot etalons are employed to address these issues by setting the net GVD to null.

3.5.2.2 Evolution

It is a Q-switched laser with an output of 527 nm at a repetition rate of 1 kHz. It consists of a diode laser for pumping and Nd: LiYF4 gain medium[28]. For acousto-optic Q switching, a piezoelectric transducer drives the silica crystal at ultrasonic frequencies which generates ultrasonic standing waves diffraction grating within the medium. By switching the vibration on or off, one can block or allow the Q-switched laser pulse to emit. An LBO crystal is operated at a constant tower temperature (164 °C) for converting a 1053 nm laser to a 527 nm laser

3.5.2.3 Regenerative Chirped Pulse Amplification (RCPA)

Libra essentially employs the RCPA technique to generate ultrashort intense laser pulses. The high-frequency laser beam, on power amplification, might damage the gain medium itself or lose the energy in a very short time by unwanted self-focusing. This problem is handled elegantly by employing a technique known as chirped pulse amplification (CPA). In the CPA technique, prior to amplification, a laser beam is considerably stretched out in time resulting in a significant reduction in peak power. Then the laser beam is allowed to pass through the Ti: sapphire crystal multiple times in the RGA cavity of Libra. This regenerative amplification converts the pulse energy from a few nJ to a few mJ. Finally, the pulse is again compressed producing a high-power ultrashort laser pulse. The stretching and compressing of the pulse are done by the respective grating devices. A typical stretcher grating introduces a longer temporal delay in the high frequency (blue band) side of the spectra and positive GVD whereas a compressor grating introduces the negative GVD and negative time delay by allowing the low frequency (red band) components to travel a longer distance to compensate the delay.

3.5.2.4 Second Harmonic Generator

Libra provides a pulsed laser output of 800 nm with a repetition rate of 1 kHz. An SHG (Harmonic, HGS-T) is employed to produce the frequency doubled beam which eventually serves as the pump for the TRMOKE system. As the working principle is very similar to the one already described earlier in section 3.5.1.3, we refrained from further describing it here.

3.5.2.5 Description of the Set up (Non-collinear pump-probe geometry)

The non-collinear TRMOKE set-up is placed on top of an optical table (Newport RS 4000) with tuned damped vibration isolation. The setup is schematically shown in the fig. 3.8. The fundamental 800 nm pulsed laser emits from Libra with spot size of ~2 mm, an average output power of ~4 W and a repetition rate of 1 kHz. A part of the s-polarized fundamental is channeled through the SHG to produce frequency doubled (λ = 400 nm) output emission with temporal width of ~50 fs and power ~500 mW. The highly attenuated counterpart of the fundamental (probe, hereafter) is guided using a set of dielectric mirrors to a retroreflector on a motorized delay stage (Newport ESP 301). Before the retroreflector, the beam is collimated by a pair of plano-convex lenses arranged in a telescopic form. After the delay, the probe passes through a Glan-Thompson polarizer (GTH5M, Thorlabs; extinction ratio 100000:1) and is steered by another family of 3 mirrors to finally incident on the sample. A plano-convex lens is used to focus the probe tightly on the sample surface making a spot size of ~100 μm. Another

attenuator is kept in the path of the probe for further modulation of the incident power.

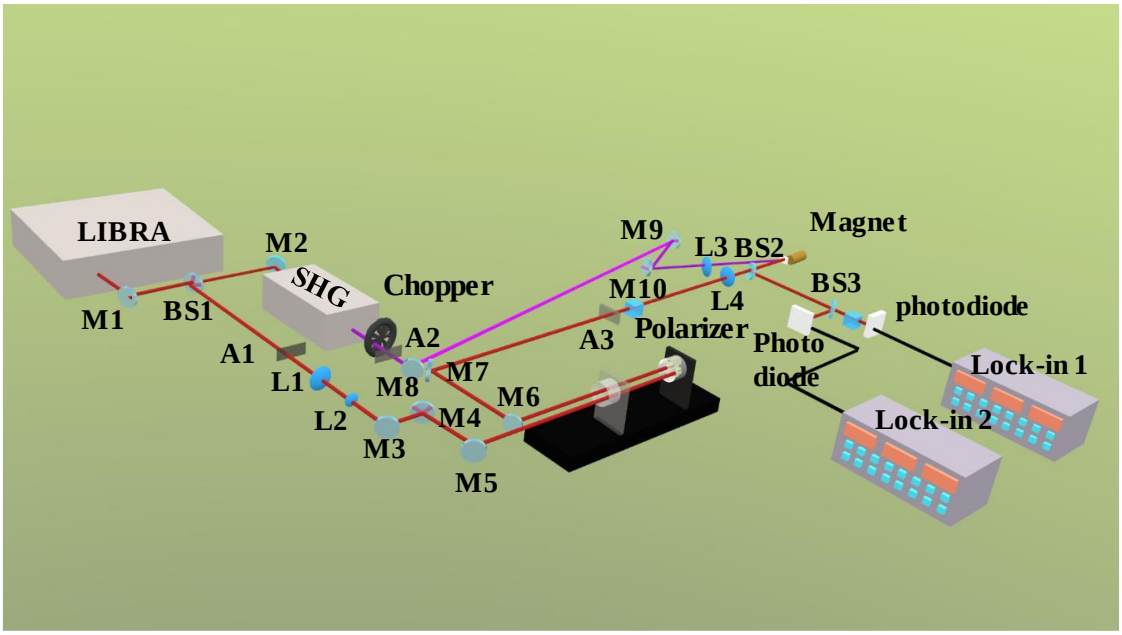

Figure 3.9: Schematic diagram of TRMOKE setup with non-collinear pump probe arrangement

The emission from SHG is guided by multiple mirrors to finally incident on the sample. The idea is to keep the path difference null between the pump and the probe. The pump makes an oblique angle with the surface and is blocked by a beam-blocker after reflection from the sample. A circular attenuator is employed in the pump path to conveniently tune the fluence during the experiment. In this non-linear overlapping of the pump and probe, the detection assembly is quite different from that of the collinear setup. For detection, the back-reflected probe is divided by a 50:50 beam splitter. One part is directly sent to a Si-photo detector connected to a lock-in amplifier which measures the reflectivity signal. Another part is passed through an analyzer (another Glan-Thompson polarizer) and finally falls on the Si detector. This detects the Kerr rotation on a slight reflectivity background when the analyzer is kept 1° away from the cross-Nicol or extinction condition. The sample is kept attached to a glass slide and holder connected to an x-y stage and a permanent magnet is employed just behind the glass slide at polar geometry. A mechanical chopper (MC 200B, Thorlabs) is used in the path of the pump beam which chops the laser at 373 Hz frequency and sends the reference to both the lock-in amplifiers (SR830, Stanford Research Systems) for phase-sensitive detection in a stroboscopic manner.

3.6 Numerical Techniques

As described earlier, the precessional magnetization dynamics is governed by the Landau

Lifshitz Gilbert (LLG) equation. The ferromagnetic resonance in thin films and bulk ellipsoidal materials can be understood with the help of LLG under macrospin formalism. Here, the LLG equation is linearized under the approximation of small angle rotation and is analytically solved assuming a single domain inside the material, i.e., a giant representative spin called "macrospin". However, understanding of magnetization dynamics in realistic systems such as a collection of patterned magnetic dots, antidots, bi-component or multilayered heterostructures with finite boundaries requires the incorporation of the effect of actual non-uniform demagnetizing fields thus demanding a non-trivial numerical treatment. Though the discrete spin models such as the Ising model or Heisenberg model can take into account the inhomogeneity of the small nanostructure, however, limited computational resources make the calculation extremely challenging for micron or sub-micron-sized nanostructures. Micromagnetic continuum theory bridges the gap between the discrete model and the macrospin model. In micromagnetic formalism, the magnetization within the medium is a continuous function of space. However, the medium is assumed to be comprised of a large number of tiny identical cells, each having a single macrospin representing the average magnetization of the cell. In numerical frameworks, one can carefully choose the cell dimensions to capture the appropriate long and short-range interactions, nature of the evolver, initial boundary conditions etc. to obtain numerical predictions of the magnetization dynamics in low-dimensional complex magnetic structures. Depending upon the way the program discretizes the sample space, there are two categories of micromagnetic simulation frameworks namely i) finite difference method (FDM) and ii) finite element method (FEM). While FDM-based programs can attain a faster solution to LLG equation sometimes, FEM-based packages are able to reproduce the edge inaccuracies in a real system better. There are a few popular choices for FDM-based micromagnetic packages such as i) OOMMF, ii) MuMax3, iii) LLG micromagnetic simulator, iv) Boris, v) Ubermag, vi) Micromagnus, vii) Magsimus etc. while i) Nmag ii) fastMag iii) Magpar etc. are well known micromagnetic frameworks which rely upon FEM. The simulations presented in the dissertation are carried out using OOMMF and LLG micro. Also, a home-built software "Dotmag" has been used for power and phase profile analysis of the spin-wave modes. Below we discuss the key aspects of these techniques.

3.6.1 OOMMF

Object-oriented micromagnetic framework (OOMMF)[29] is an open-source cross-platform (Windows, Linux and a few UNIX-based operating systems) FDM-based micromagnetic simulation programs originally developed by Michael Donahue and D. G. Porter. It is one of

the oldest and most reliable numerical packages written in C++ and Tcl/Tk script. In OOMMF the simulation specimen is usually specified via the 'box atlas' module in the code ('.mif') itself. However, sometimes the sample geometry and the associated boundaries might be non-trivial which can be handled efficiently by defining the image replica of the actual sample via the powerful 'image atlas' module. All the other necessary conditions such as the initial magnetization, exchange stiffness constant, magnetic anisotropy, saturation magnetization and bias magnetic field configurations are specified using the respective modules within the code. OOMMF being an FDM-based simulation package discretizes the given sample in cuboidal/ parallelepiped cells having user-specified cell dimensions in the 'mesh' segment. The cell dimension has a crucial role to incorporate the dipole and exchange interactions interplay in a system and is usually kept smaller than the exchange length of the material under consideration. It is worthy to note that the OOMMF has limited functionality to incorporate the exact 3D structures with irregular geometries. Moreover, it provides a lot of methods for solving ordinary differential equations to choose from. For the iterative method of solution, either the time evolver or the energy evolver can be used with the help of their respective drivers. Depending upon the stopping criterion, drivers provide the initial condition to the evolver in each iterative step and help the program save the state parameters in vector format. Where the time evolver solves the LLG equation for each of the cells in an iterative approach, the energy evolver attempts to find the global minima in the energy profile of the structure in every step. On satisfying the convergence criterion, the program stops and all the time-dependent parameters such as magnetization, field components and energies are extracted in '.ovf' or '.omf' format. OOMMF also supports the output of the parameters in plain text format for further processing and is enriched with live graph plotting functionality.

3.6.2 LLG Micromagnetic Simulator

LLG micromagnetic simulator (LLG micro, hereafter) is a commercial software for solving LLG equation in micromagnetic formalism developed by M. R. Scheinfein[30]. It has a very user-friendly interface for optimized input and post-simulation analyses. In the input interface, the user can enter all the relevant magnetic parameters and the sample details can be provided in an image format. It can offer a significant edge in comparison to OOMMF in simulating multilayered heterostructures with varying magnetic properties across the thickness due to its flexible input interface. It also offers to configure a time-dependent bias field in the simulation. LLG micro first sets up the 3D cartesian mesh environment with supplied parameters and boundary conditions. LLG micro offers four different integrators to solve LLG: i) Euler

Cartesian, ii) Gauss-Seidel, iii) Cartesian predictor-corrector and iv) rotation matrices method. Depending upon the problem requirement one can choose between these solvers. Such as the Euler Cartesian method offers the least simulation time but also suffers with the least accuracy, Rotation matrices method works best when the damping is higher than 0.5 or so. However, the Cartesian predictor-corrector can be one of the best choices for most situations as it offers faster solutions with higher accuracy even when the damping is 0.01 or below.

One of the most important features of LLG micro is the opportunity for powerful visualization and post-simulation computations. Here, the magnetic domains and the interaction field components in the nanostructures under investigation can be visualized in coloured contour plots. Some additional functionalities like spin-polarized currents, effects of finite temperature etc. can also be incorporated in simulation by LLG micro.

3.6.3 Dotmag

In the study of spin-wave dynamics, power and phase profile information can add superior insights to the overall understanding and are thus considered indispensable. While most of the micromagnetic packages (commercial or open source) do a great job by offering different LLG solvers with various functionalities, almost all of them lack a straightforward module to calculate this. Keeping this in mind, Dotmag[31,32], a set of codes, is developed by our group on the Matlab platform. Dotmag does not solve the LLG equation, rather it helps in the post-processing of the OOMMF output files and is employed to extract further information about the magnetization dynamics demonstrated by a nanosystem. In OOMMF, each of the output .omf files contains the magnetization as a function of spatial coordinates [$m = m\ (x,y,z)$] and thus, the collection of all such files in a proper sequence provides nothing but the magnetization as a function of both space and time i.e. mathematically,

$$m = m(x, y, z, t) \tag{3.3}$$

It is quite non-trivial to understand the power and phase information for any particular spin wave from this data. The central idea is to observe the power and phase distribution on a 2D slice of the specimen for a definite resonant mode frequency. This is essentially done in Dotmag by taking the projection of the magnetization at a particular constant z plane and then by performing a discrete fast Fourier transform to it. So, after fixing $z = z_0$ (some constant) magnetization is no more a function of z. A calculation of FFT readily transforms the magnetization intensities in the frequency domain which means,

$$FFT\ [m(x, y, t] = \tilde{m}(x, y, f)$$

Now $\tilde{m}(x, y, f)$ being a complex function of planar spatial coordinates and frequency, the

power and phase information for any given frequency f_0 are calculated numerically by using the following relations:

Power:

$$P(x, y, f_0) = 20\ \log_{10}[\tilde{m}(x, y, f_0)] \tag{3.4}$$

Phase:

$$\phi(x, y, f_0) = \tan^{-1}\left(\frac{Im\ [\tilde{m}(x, y, f_0)]}{Re\ [\tilde{m}(x, y, f_0)]}\right) \tag{3.5}$$

The SW power is expressed in terms of dB and phase in radians. The Dotmag is executed in a Matlab environment and the extracted output shows the spatial mapping of power and phase at discrete frequencies. It is important to note that, the frequency resolution depends upon the total time window of the simulation while the spatial resolution of calculated power and phase maps depends on the discretization of the specimen during micromagnetic simulation.

3.7 References

[1]C. A. Bishop, in *Vacuum Deposition onto Webs, Films and Foils*, edited by C. A. Bishop (William Andrew Publishing, Oxford, 2011), pp. 261.
[2]R. Behrisch, *Sputtering by particle bombardment* (Springer-Verlag New York, 1981), Vol. 1.
[3]J. T. Gudmundsson and D. Lundin, in *High Power Impulse Magnetron Sputtering*, edited by D. Lundin, T. Minea, and J. T. Gudmundsson (Elsevier, 2020), pp. 1.
[4]R. F. W. Pease, Contemporary Physics **22**, 265 (1981).
[5]A. A. Tseng, C. Kuan, C. D. Chen, and K. J. Ma, IEEE Transactions on Electronics Packaging Manufacturing **26**, 141 (2003).
[6]M. Shinji and O. Yukinori, Nanotechnology **7**, 247 (1996).
[7]A. T. Hindmarch, D. E. Parkes, and A. W. Rushforth, Vacuum **86**, 1600 (2012).
[8]D. McMullan, Scanning **17**, 175 (1995).
[9]P. Eaton and P. West, *Atomic force microscopy* (Oxford university press, 2010).
[10]F. J. Giessibl, Rev. Mod. Phys **75**, 949 (2003).
[11]C. Schönenberger and S. Alvarado, Zeitschrift für Physik B Condensed Matter **80**, 373 (1990).
[12]B. E. Warren, *X-ray Diffraction* (Courier Corporation, 1990).
[13]A. A. Bunaciu, E. g. Udriştioiu, and H. Y. Aboul-Enein, Crit. Rev. Anal. Chem. **45**, 289 (2015).
[14]E. Chason and T. M. Mayer, Crit. Rev. Solid State Mater. Sci. **22**, 1 (1997).
[15]G. Vignaud and A. Gibaud, J. Appl. Crystallogr. **52**, 201 (2019).
[16]S. Hasegawa, in *Characterization of Materials*2012), pp. 1.
[17]N. Masud and J. B. Pendry, Journal of Physics C: Solid State Physics **9**, 1833 (1976).
[18]S. Foner, Rev. Sci. Instrum. **30**, 548 (1959).
[19]A. Barman and J. Sinha, *Spin Dynamics and Damping in Ferromagnetic Thin Films and*

Nanostructures (Springer International Publishing, 2018).
[20]B. Rana, D. Kumar, S. Barman, S. Pal, Y. Fukuma, Y. Otani, and A. Barman, ACS Nano **5**, 9559 (2011).
[21]A. Barman and A. Haldar, in *Solid State Phys.*, edited by R. E. Camley, and R. L. Stamps (Academic Press, 2014), pp. 1.
[22]Spectra-Physics, *Millennia eV User's Manual* (Newport Corporation, Santa Clara, CA, 2013).
[23]*User's Manual: Tsunami Modelocked Ti:Sapphire Laser* (Spectra-Physics, California, USA, 2002).
[24]*User's Manual, Model 3980: Frequency Doubler and Pulse Selector* (Spectra-Physics, California, USA, 2002).
[25]B. Rana, University of Calcutta, 2013.
[26]*Operators Manual: Libra Ultrafast Amplifier Laser System* (Coherent, Santa Clara, USA.
[27]*Vitesse Diode Pumped Modelocked Ti:Sapphire Laser* (Coherent, Santa Clara, USA.
[28]*Operator's Manual: Evolution-15/30, High-Energy, High-Average Power, Diode-Pumped, Kilohertz, Q-Switched, Intra-Cavity Doubled, Nd:YLF Laser* (Coherent, Santa Clara, USA.
[29] M. Donahue, D. G. Porter NIST Interagency Report No. 6376; National Institute of Standard and Technology, Gaithersburg, MD, URL: http://math.nist.gov/oommf:(1999).
[30]M. R. Scheinfein LLG Micromagnetics Simulator, http://llgmicro.home.mindspring.com (accessed March 8, 2018).
[31]D. Kumar, O. Dmytriiev, S. Ponraj, and A. Barman, J Phys. D:Appl. Phys **45**, 015001 (2011).
[32]G. Venkat, D. Kumar, M. Franchin, O. Dmytriiev, M. Mruczkiewicz, H. Fangohr, A. Barman, M. Krawczyk, and A. Prabhakar, IEEE Trans. Magn. **49**, 524 (2013).

Chapter 4

4. Dynamic Configurational Anisotropy in $Ni_{80}Fe_{20}$ Antidot Lattice with Complex Geometry

4.1 Introduction

Magnonics[1], initially emerged as a sub-branch of magnetism, has matured in the last decade as a major branch of condensed matter physics and nanoscience dealing with principles and potential realization of energy-efficient logic, processing and communication devices via excitation, active or passive manipulation and detection of spin waves, known as magnons in its quantized form[2-4]. The recent developments in this field have successfully entangled the conventional findings with various fascinating quantum mechanical effects like spin-orbit coupling (SOC)[5], spin current[6], Dzyaloshinskii-Moriya interaction (DMI)[7], non-linearity[8] and topological effects[9,10] thereby strengthening the fundamentals as well as presenting next-generation multifunctional magnonic devices with superior functionalities[4]. The faster propagation velocities demonstrated by short-wavelength spin waves[11] and magnon current generated by the collective unidirectional motion of spin-wave, showing lower energy dissipation in comparison to spin-polarized or pure spin-current, strongly envisioned the future potential of magnonics[12,13]. Moreover, the possibility of energy harvesting has been demonstrated in the achievement of strongly-coupled magnon-phonon[14], magnon-photon[15,16] or magnon-magnon[17,18] systems, which offers potential for quantum transduction and gives rise to the emerging branch of hybrid magnonics[19,20].

Ferromagnetic antidot lattices (ADLs) have emerged as one of the most attractive systems in the magnonic crystal (MC)[21] family, where the periodic modulation of magnetic properties is achieved via the incorporation of non-magnetic etched out sections or nanoholes in an otherwise continuous ferromagnetic media. They exhibit immense potential for designing high speed reconfigurable magnonic devices operating in the sub-100 nm magnon wavelength regime by efficient tailoring of the dipole-exchange interactions[11]. The initial works on the magnetization dynamics of ADLs revealed excitation of nonuniform magnonic modes[22], pattern induced splitting [23], magnetic field strength and orientation-dependent localization and delocalization of spin-wave modes [24-27], and anisotropic spin-wave propagation[28]. A flurry of successive experimental, as well as numerical investigations[29-31], have surfaced

focusing on manipulation of physical parameters and engineering of magnonic band structure[32,33] by varying the geometric properties including shape[34], lattice constant[35], lattice symmetry[36-38], base material[39], besides the strength and orientation of external bias magnetic field[40]. These are associated with the exploitation of potential applications in GHz-frequency on-chip filters[41], waveguides[42], multiplexers[43], couplers[44], phase shifters[45], transistors[46] and logic devices[47].

Recently, the idea of introducing geometric complexity in MCs has attracted significant attention due to the richer and more complex spin-wave dynamics[48]. Substantial reconfigurability of rich spin-wave dynamics has been demonstrated in various complex ADLs in the form of quasiperiodic octagonal lattice[49], defective honeycomb lattice[50], octagonal lattice with triangular basis[51], some aperiodic structures[52],artificial fractal structures[53] and many more quasiperiodic MCs in recent studies[54-57]. This calls for investigation of new structures in the pursuit of more versatile and reconfigurable spin-wave dynamics. Here we investigate the spin-wave dynamics of a diamond-shaped antidot lattice (DADLs, hereafter)[58], where the diamond shaped antidots are arranged on square and hexagonal lattices. Few earlier studies on diamond shaped nanofilms explored the dependence of magnetic reversal on the length-to-width ratio [59] along with correlation of shape anisotropy[60] and influences of demagnetizing field[61] for this type of basis. Thus, diamond shaped basis can be regarded as the square nanohole rotated by 45° from one of its edges, which can introduce an additional symmetry in the anisotropic of the overall spin-wave dynamics. The ferromagnetic nanochannels between the antidots, which accommodate the extension of spin-waves, can be substantially modified due to the presence of demagnetized regions around the four sharp corners of the diamond-shaped basis, which are unusually placed *w.r.t.* the symmetry of the lattice. Thus, DADLs are expected to exhibit a unique pattern of inhomogeneity in the local magnetostatic field distribution, which, in turn, can produce atypical anisotropic signature in the evolution of spin-waves.

Here, we have studied the precessional magnetization dynamics of two types of DADL using the time-resolved magneto-optical Kerr effect (TRMOKE) microscope and micromagnetic simulations. A rich variation of the spin-wave dynamics with the strength and in-plane orientation of the external bias field has unravelled the signature of mode conversion from extended to quantized/localized nature. An extensive comparative study between the DADLs arranged in square and closely packed hexagonal symmetry leads to the understanding of the competition between the basis shape and lattice symmetry in the overall dynamical configurational magnetic anisotropy. The internal magnetic field profiles enveloping the sharp

edges of the antidots have been found to be crucial in the mode conversion and offers great tunability of spin-wave dynamics for this complex configuration.

4.2 Experimental and Simulation Details

4.2.1 Sample Fabrication

Two-dimensional diamond-shaped antidot arrays carved on $Ni_{80}Fe_{20}$ (Permalloy or Py hereafter) film, arranged in square and hexagonal lattice symmetry, were fabricated over an area of 25×25 μm^2 using a combination of electron beam lithography (EBL), electron beam evaporation (EBE) and ion milling techniques[51]. Firstly, a 20-nm-thick Py layer was grown on a self-oxidized Si(100) substrate using EBE technique at a base pressure of ~2×10^{-8} torr. To protect the Py film from the external atmosphere as well as from the possible degradation from the laser heating during TRMOKE measurement, a capping layer of 3 nm of Al_2O_3 was deposited on top of the Py at the same base pressure of ~2×10^{-8} torr and a deposition rate of 0.2 Å/s. A magnetic hysteresis loop of Py film coated with Al_2O_3 measured using static magneto-optical Kerr effect (MOKE) presented in fig. 8.1(a) of Appendix A ensures that the quality of the Py film does not alter due to deposition of Al_2O_3. No discernible shift in the MOKE loop due to exchange bias effect as a result of possible surface oxidation is observed. A bilayer of MMA and PMMA was applied on the Py/Al_2O_3 and EBL was used to prepare the desired pattern on the resist. This was followed by the Argon ion-milling at a base pressure of 1×10^{-4} torr with 60 mA beam current for 6 minutes and subsequent lift-off of the resist to obtain the ADLs. The scanning electron microscope (SEM) images of the fabricated ADLs are presented in fig. 4.1(a) and 4.1(b). The diamond-shaped antidots have a corner-to-corner length (d) of 200 nm and separation between nearest edge (s) of 300 nm with a mild tolerance (±5%) in its lateral dimensions. The lattice constant (a) for the square lattice is 500 nm, whereas in the hexagonal lattice, the lattice parameters are found to be a = 500 nm, b = 520 nm and γ' = 120°. It is clear from the SEM images that the edges of the diamond antidots suffer from mild deformation from the ideal shape.

4.2.2 Time-Resolved Magneto-Optic Kerr Effect Measurement

A custom-built TRMOKE microscope set up based on two-colour collinear pump-probe geometry was employed to study the time-resolved magnetization dynamics which essentially used the fundamental laser beam (wavelength, λ = 800 nm, pulse-width = 80 fs) from a mode-locked Ti-sapphire laser (Tsunami, Spectra-Physics) to probe the dynamics whereas its frequency-doubled counterpart (λ = 400 nm, pulse-width = 100 fs) was used to optically excite

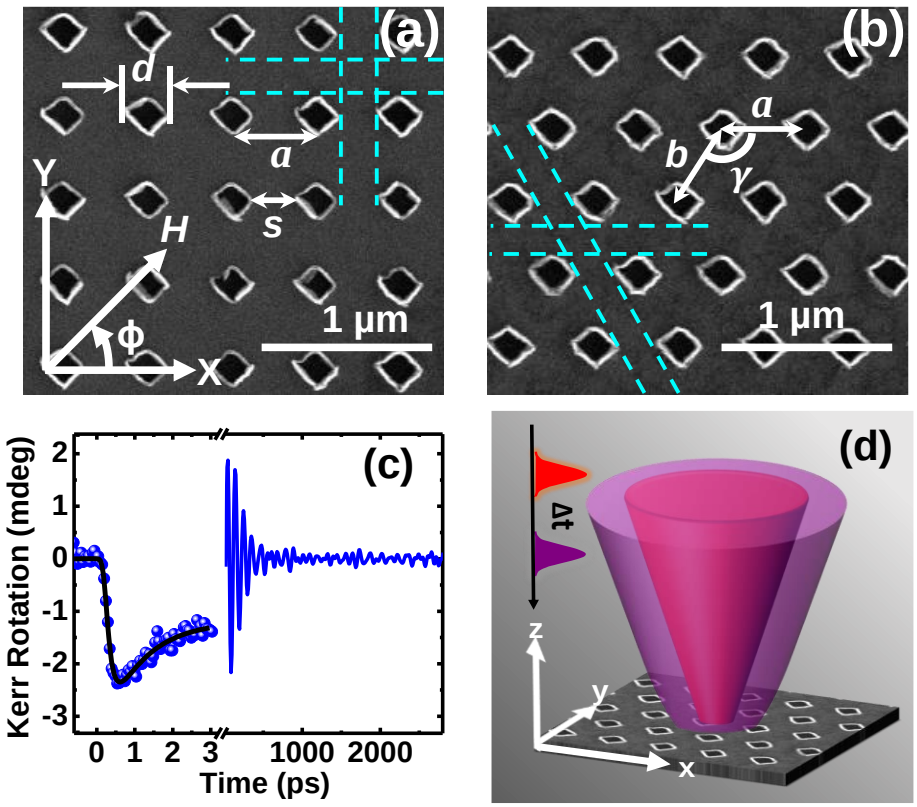

Figure 4.1: SEM images of (a) square and (b) hexagonal diamond antidot lattices. The spin-wave extension channels are schematically shown by dotted lines in the SEM images. (c) Typical time-resolved Ker-rotation data from the square lattice showing ultrafast demagnetization, fast relaxation and slow relaxation superimposed with precession of magnetization. (d) TRMOKE measurement geometry with collinear pump and probe beams.

(pump) the sample. A retro-reflector mounted on a motorized delay stage was placed on the path of the probe beam which allowed us to introduce the variable temporal delay between the pump and probe pulses. Both the beams were then combined and allowed to pass collinearly through a microscope objective (40x, N.A. = 0.65) and made to incident on the sample. The probe was tightly focused to a spot size of ~800 nm and the pump was kept at a slightly defocused condition having a spot size of ~1 μm on the sample surface as depicted in the schematic fig. 4.1(c). A thorough and careful alignment ensured that the collinear condition was maintained throughout the experiment. The sample was placed on a piezoelectric x-y-z scanning stage with a feedback loop, allowing the pump and probe to excite and collect the dynamics from the same sample position respectively. A magnetic field was applied on the sample with around 10° tilt from the sample plane. This tilt ensured the necessary out-of-plane demagnetizing which was altered by the pump pulse to launch the magnetization precession in the sample. The in-plane component of this magnetic field is referred to as the bias magnetic

field (H), whose magnitude and direction (φ) were varied during the measurements. The pump beam was modulated by an optical chopper and was used as a reference signal for the phase-sensitive detection of the signal by a pair of lock-in amplifiers. The optical bridge detector (OBD) which used a polarized beam splitter followed by a pair of photodiodes in the balanced condition[62], ensured the distinct detection of reflectivity and Kerr rotation signals without any breakthrough of one into another.

4.2.3 Simulation in Micromagnetic Framework

The origin and nature of the spin-wave modes was studied under the micromagnetic framework. Here, we essentially solve the Landau-Lifshitz-Gilbert (LLG) semi-classical equation for the system under consideration in the continuum limit. In the object-oriented micromagnetic framework (OOMMF) [63] we used a finite difference based approach and sub-divided the whole system into several rectangular prism-like cells each of them possessing a single macrospin. At first, a static magnetic microstate was constructed under the bias magnetic field from an initially uniformly oriented magnetization state. Then the optical excitation by a laser pulse was mimicked by a square magnetic pulse with magnitude of 30 Oe and 20 ps pulse duration. The system was then allowed to relax under the bias magnetic field only and the time-driver iteratively solved the LLG equation thereby finding out all possible resonant modes for spins from different zones of the sample under the study. Here, the sample was discretized into cells with dimensions $4\times4\times20$ nm^3 with an intention to incorporate the exchange interaction in play as the exchange length of Py is ~5.2 nm. The material parameters used in the simulation like Gilbert damping $\alpha = 0.008$ and exchange stiffness constant $A = 1.3\times10^{-6}$ erg/cm was taken from the literature[64], whereas saturation magnetization $M_s = 860$ emu/cc, gyromagnetic ratio $\gamma = 17.6$MHz/Oe and magnetocrystalline anisotropy constant $K = 0$ values was extracted from the fit of the bias field dependence of a 20-nm-thick Py blanket film deposited under the same conditions. Since Py film was deposited using EBE it is likely to be highly polycrystalline in nature with grains having no specific orientation, and hence, carries no significant contribution from magnetocrystalline anisotropy. However, to confirm that, magnetic hysteresis loops of the Py/Al_2O_3 film at different in-plane magnetic field orientations (φ) are measured. A plot of the coercive field as a function φ obtained from static MOKE measurement is presented in fig. 8.1(b) of Appendix A which validates the consideration of negligible magneto-crystalline anisotropy in the simulation. Nevertheless, consideration of small value of K would have introduced an additional two-fold symmetry in the frequency vs. ϕ in the simulation but no qualitative change in the nature of the spin-wave mode. We have also performed simulations

introducing the actual edge deformations in the antidot shape as shown in fig. 8.2 of Appendix A, where nearly identical results are obtained to that of the ideal antidot shape.

4.3 Results and Discussion

Figure 4.1(c) shows representative Kerr rotation data in the sub-picosecond to nanosecond time domain from the square DADL sample, which reveals three different temporal phenomena during the interaction of ultrashort laser pulse with the sample. Region I refers to the well-known ultrafast demagnetization followed by the fast remagnetization (region II) and precessional motion of magnetization superimposed with a slow remagnetization (region III) process. There an essential energy exchange takes place initially among the electron, spin and lattice heat baths and then with the surroundings[65]. The data have been fitted with the theoretical expression (Eq. 4.1) obtained from solving three coupled differential equations in the three temperature model considering the generation of hot electrons after interacting with laser, a loss of spin memory and subsequent distribution of energies during the remagnetization process[66].

$$-\frac{\Delta M}{M} = \left\{\left[\frac{A_1}{\left(1+\frac{t}{\tau_0}\right)^{\frac{1}{2}}} - \frac{A_2\tau_E - A_1\tau_M}{\tau_E - \tau_M}e^{-\left(\frac{t}{\tau_M}\right)} - \frac{\tau_E(A_1 - A_2)}{\tau_E - \tau_M}e^{-\left(\frac{t}{\tau_E}\right)}\right]H(t) + A_3\delta(t)\right\} \otimes G(t) \quad (4.1)$$

Here, A_1 represents the amplitude of magnetization after equilibrium is restored, $A2$ is proportional to the rise in the electronic temperature and $A3$ corresponds to the state filling effects. $H(t)$, $\delta(t)$ and $G(t)$ are the Heaviside step function, Dirac delta function and Gaussian function corresponding to the laser pulse. From the fit, we have calculated τ_M = 187 ± 19 fs, 224 ± 7 fs, and τ_E= 949 ± 17 fs, 958 ± 20 fs for the square and hexagonal lattices respectively. Since τ_M is a material parameter is is not expected to change significantly with lattice geometry but the slight difference in τ_M between these two lattices may stem from slightly different condition of measurement and different in defects and deformations in the two samples.

4.3.1 Bias Field Dependence of Magnetization Dynamics

At first, we study the bias field dependent frequencies of the spin waves. A biexponential background was subtracted from the time-resolved Kerr rotation data corresponding to the fast and slow remagnetization to obtain the purely precessional oscillation of magnetization. Subsequently fast Fourier transformation (FFT) was applied to the time-resolved data with rectangular window function to obtain the power vs. frequency spectra of the spin-wave modes

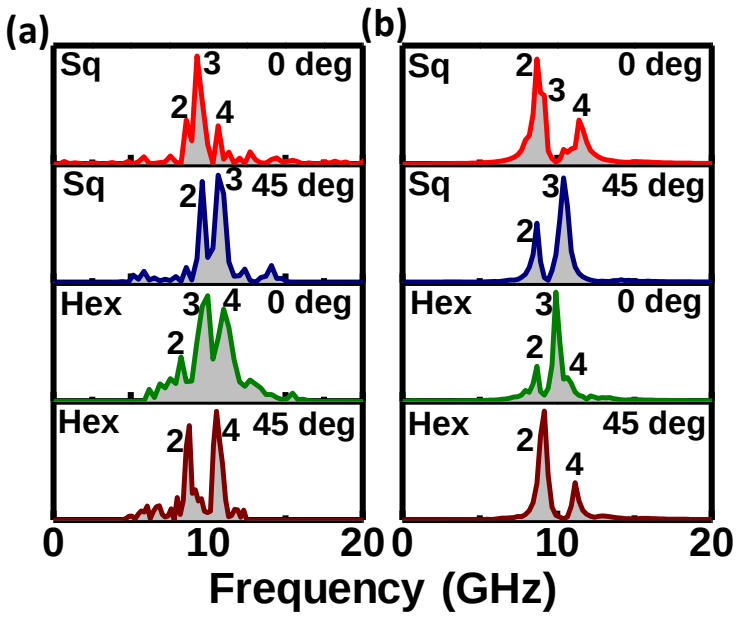

Figure 4.2: (a) Experimental and (b) simulated spin-wave power spectra at H = 1 kOe for φ = 0° and 45° in square and hexagonal DADL.

for the two lattices as shown in fig. 4.2 for H = 1 kOe. Figures 4.3(a) and (b) represent the bias field variation of frequency (f vs. H) of three spin-wave modes for in the range 0.38 kOe ≤ H ≤ 1.0 kOe at $\varphi = 0°$. A systematic variation in f with H is observed in both square and hexagonal DADL confirming purely magnetic origin of the modes. The lowest frequency mode M1 and the highest frequency mode M5 appear only for values of H and exhibit no stable field dispersion. Interestingly, mode M3 can be identified as a uniform mode both for the square and hexagonal DADL as discussed later in this article. Therefore, we fitted f vs. H of M3 with the well-known Kittel equation (Eq. 4.2)

$$f = \frac{\gamma}{2\pi}\sqrt{(H + H_k)\left(H + H_k + 4\pi M_{eff}\right)} \tag{4.2}$$

using magneto-crystalline anisotropy field H_K = 0 and extracted the effective magnetization values (M_{eff}) as 767 emu/cc and 918 emu/cc for Square and hexagonal DADL respectively. Here the effective magnetization parameter takes care of the effects from the demagnetizing fields around the antidot and readjusts itself resulting in a significant alteration from its bulk value.

4.3.2 Investigation of Configurational Anisotropy

In order to investigate the role of configurational magnetic anisotropy in the modulation of spin-wave dynamics, the time-resolved precessional oscillations were measured by varying φ

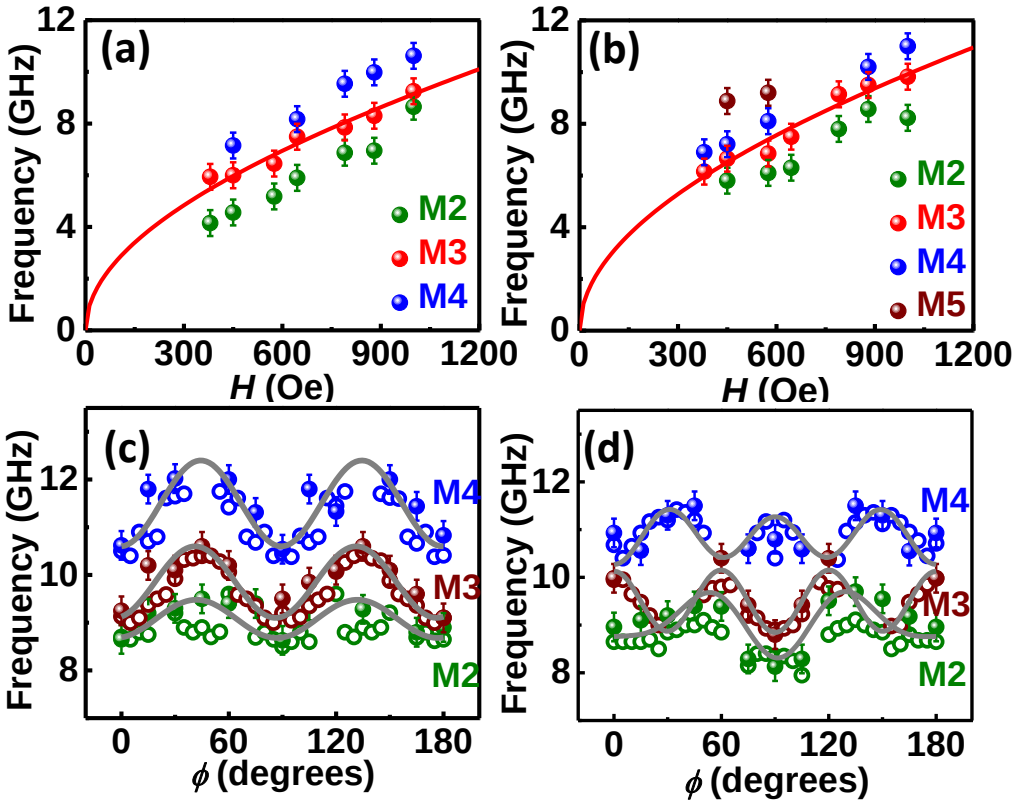

Figure 4.3: Bias field dependence of spin-wave mode frequencies in (a) square and (b) hexagonal DADL. Anisotropic variation of spin-wave frequencies with in-plane orientation of bias magnetic field at H = 1.0 kOe in (c) square and (d) hexagonal DADL.

in the range $0° \leq \varphi \leq 180°$ at $H = 1$ kOe. Figure 4.2(a) experimental spin-wave spectra for the two lattices at $\varphi = 0°$ and 45°, while fig. 4.2(b) shows the corresponding simulated spin-wave spectra. Figures 4.3(c) and (d) plot the angular dispersion of the spin-wave mode frequencies for the square and hexagonal DADL, respectively. The solid and hollow circles represent the experimental and simulated mode frequencies, whereas, the solid lines represent the theoretical fits consisting of a weighted combination of different harmonic functions corresponding to different rotational symmetries. The angular dispersion for the square DADL (fig. 4.3(c)) reveals that modes M3 and M4 attain their respective maxima at 45° and then gradually decrease to attain minima at 90° together in phase thereby clearly indicating anisotropic nature with four-fold rotational symmetry. Mode M2 also shows four-fold anisotropy with a much lower amplitude of anisotropic contribution. Figure 4.3(d) shows the angular evolution of spin-wave modes for hexagonal DADL. Here, mode M4 attains its maxima periodically at a gap of 30° though with a significant variation in the amplitude which can be fitted using a harmonic function with a strong six-fold symmetry along with the superposition of a weak four-fold

symmetry. Mode M3 displays a similar anisotropic behaviour with modified weightage of harmonics though in the opposite phase to that of mode M4. The anisotropic nature exhibited by mode M2 is quite complex in the regime under consideration. This mode is found to be coupled with the mode M3 in the range $25° \leq \varphi < 55°$ and in the subsequent complementary angles.

4.3.3 Investigation of Spatial Spin-Wave Power and Phase Profiles

For a better understanding of the origin and behaviour of the spin-wave modes at various angles, the spatial profiles (power and phase) of these modes were calculated using a custom-built MATLAB based code, named "Dotmag" [67]. The simulated power and phase maps of the square DADL, as shown in fig. 4.4, shows the presence of different spin-wave resonant modes, namely an energetically trapped or localized edge mode, a uniformly extended mode via antidot channel and quantized standing wave mode due to the modulation of confining magnetic potential by the demagnetizing fields around diamond-shaped antidots. For a

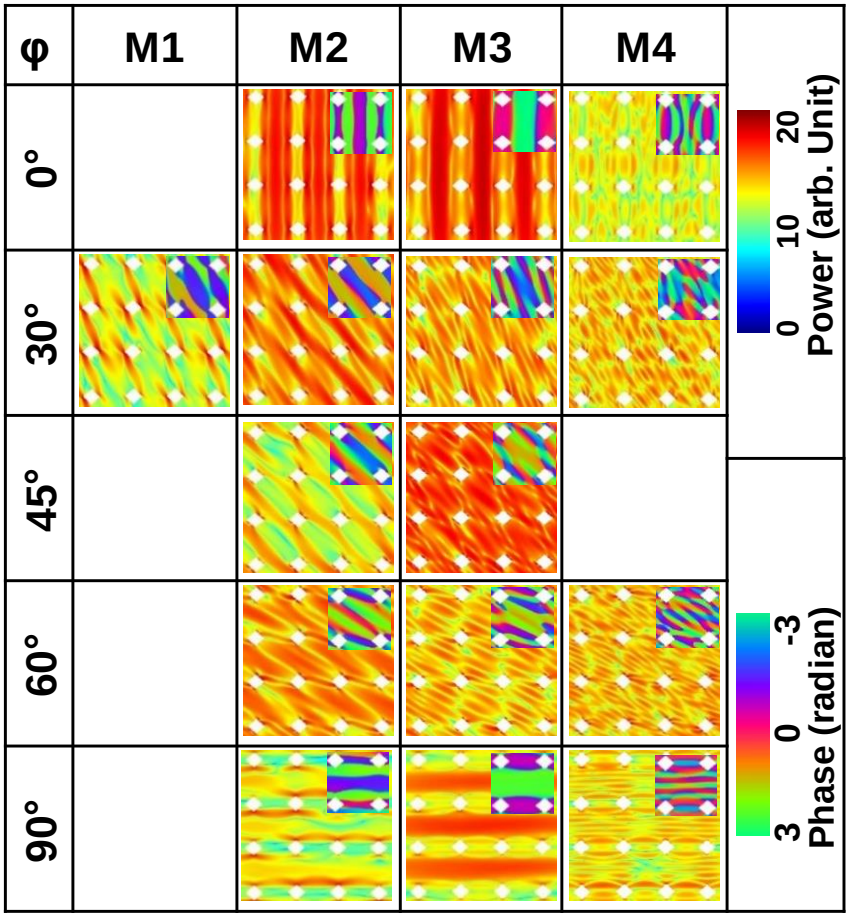

Figure 4.4: Power and phase (embedded) profiles of the spin-wave modes in square DADL at different in-plane bias magnetic field orientations (φ) at H = 1.0 kOe. The colour maps for power and phase profiles are shown at the right side of the figure.

consistent description of the nature of the standing spin-wave modes, we assign 'n' as a quantization number to a resonant mode confined between two nearest neighbour basis units. We observe that the lowest frequency mode M1, which only appears at some specific values of φ, is an edge mode with a very low power concentrated at the sharp corners of diamond antidots. At $\varphi = 30°$, the power from the basis edges couples with the first nearest neighbour and helps to gain this mode a considerable intensity. At $\varphi = 0°$, mode M2 gets an extended nature in the y-direction through the Py channel aided by the dipole and exchange interactions, although, at the same time it forms a standing wave pattern in the x-direction between two nearest neighbouring diamond antidots in a backward volume (BV)-like geometry with $n = 3$. Interestingly at $\varphi = 45°$, this mode power extends up to the 2nd nearest neighbour or even further but did not extend through the full channel thereby showing a *pseudo-extended* nature with $n = 3$. At $\varphi = 60°$, the nature of M2 changes drastically and it becomes a quantized mode between two 2nd nearest neighbours. At 90°, this mode becomes a localized one ($n = 3$) with much-reduced power concentrated only at the edges of the antidots. The other higher frequency mode, M3 has extended nature like M2 through the Py channel along the y-direction in the DE geometry at $\varphi = 0°$. However, with the increase of φ, mode M3 becomes a quantized mode in BV-like geometry with $n = 5$, 7 and 5 at $\varphi = 30°$, 45° and 60° respectively. At $\varphi = 90°$, mode M3 undergoes a remarkable transformation by reclaiming its extended nature along the x-direction, and hence, a phenomenon of *mode conversion* with the variation of the orientation of the bias magnetic field is observed. The mode M4 remains highly quantized for the entire angular regime under consideration with $n = 7$, 7, 9 and 7 at $\varphi = 0°$, 30°, 60° and 90°, respectively, with its axis in consonance with the bias orientation. .

The power and phase (embedded inside) profiles for the hexagonal DADL, presented in fig. 4.5, give us insight into the spin-wave modes for this ADL type. At $\varphi = 0°$, the mode M2 is an edge mediated extended mode in the y-direction having quantized nature in BV-like geometry along the x-direction with $n = 3$ despite the dearth of ferromagnetic channel formation at this angle. At $\varphi = 30°$, a wider channel becomes accessible to the spin-wave for the hexagonal arrangement of the lattice, and as a consequence, mode M2 converts to a fully extended mode confirming a clear mode conversion. However, for $30° \leq \varphi \leq 90°$ nature of this mode significantly modifies to pseudo-extended mode with $n = 3$ for both $\varphi = 45°$ and 60°. At $\varphi = 90°$, mode M2 is converted into a quantized mode ($n = 7$) with maximum power concentrated along the edges of the antidots. On the contrary, mode M3 has a quantized nature at all values of φ in the range $0° \leq \varphi \leq 75°$, but at $\varphi = 90°$, a channel is opened for this mode to convert it to

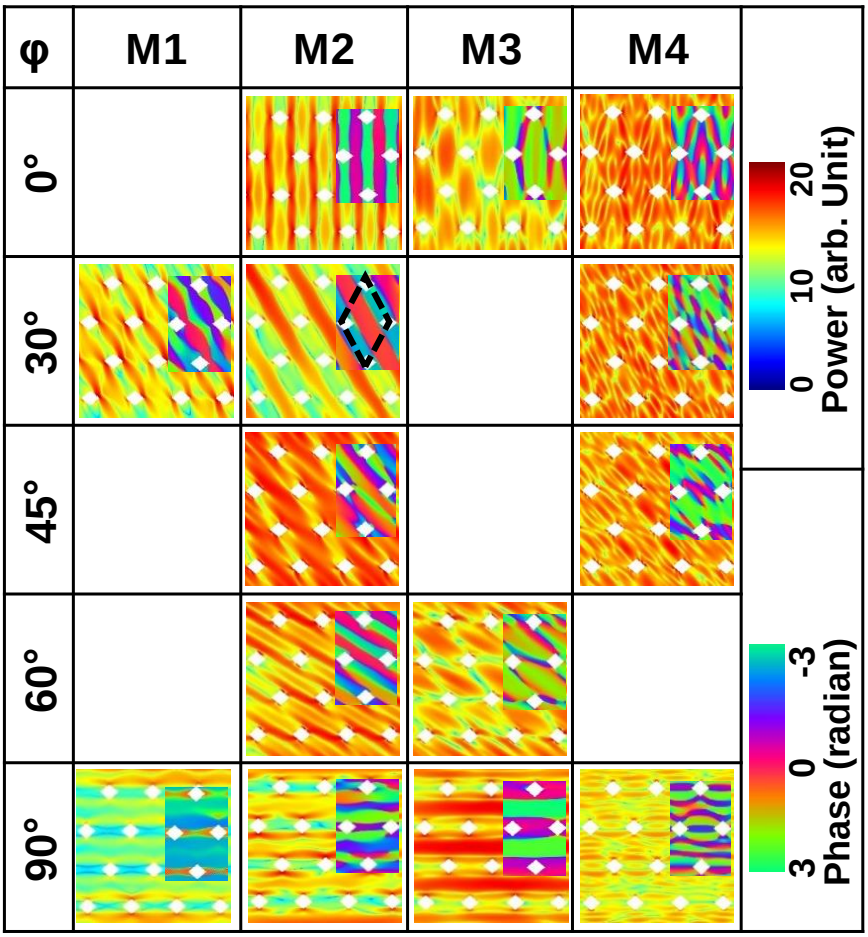

Figure 4.5: Power and phase (embedded) profiles of the spin-wave modes in hexagonal DADL at different in-plane bias magnetic field orientations (φ) at H = 1.0 kOe. The colour maps for power and phase profiles are shown at the right side of the figure.

an extended one. We observe mode conversion both for M2 and M3 but at different values of φ. The mode M4 is a quantized mode for all values of $\varphi < 90°$ with n = 7, 7 and 3 for φ = 0°, 30° and 45°. This mode undergoes moderate alteration at φ = 90° at which its phase contrast become clear with n = 11. The variation in the confining potentials at φ = 90° within the rhombic region (as shown by the black dotted box) for the other angles could play a leading role in this sharp alteration of mode character.

4.3.4 Calculation of Internal Magnetostatic Field Profiles

To investigate the origin of the anisotropic behaviour of the spin-waves we further calculated the internal magnetostatic fields using LLG micromagnetic simulator [68]. The contour plots of the simulated magnetostatic field distribution for the 3 × 3 arrays of square and hexagonal DADLs are shown in the section 8.3 of Appendix A. Figures 4.6(a) and (b) show a line-scan plot of the internal field along the x-direction across the dotted line, which reveal systematic

decrease in the internal field strength with φ in the range $0° \leq \varphi < 90°$ for both square and hexagonal DADLs. However, careful observation in fig. 4.6(c) enables us to understand the drastic modulation exhibited by the contour plots of the magnetostatic field map on changing the orientation of the bias magnetic field. For the square lattice at $\varphi = 0°$, the field lines are only concentrated around the sharp corners of the antidots. However, the magnetostatic field lines show denser distribution at the sharp corners of the diamond antidots and a very strong nearest neighbour interaction (see fig. 8.3 of Appendix A) i.e. coupling in the x-direction for φ

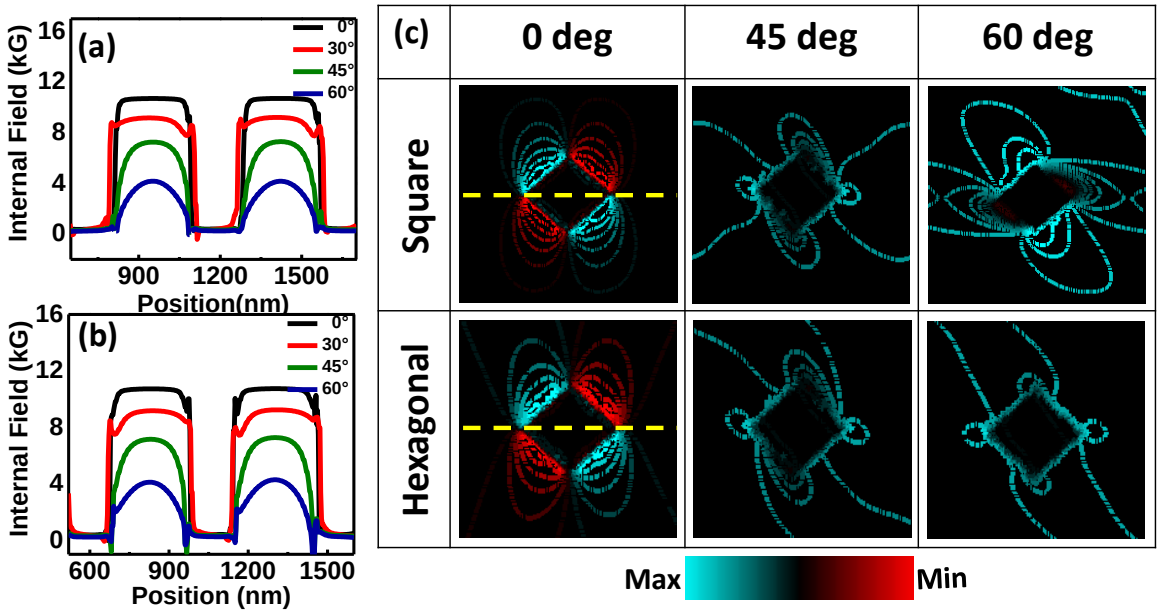

Figure 4.6: Line scans of internal magnetic field for different bias magnetic field orientations (φ) in (a) square and (b) hexagonal DADL. (c) Internal magnetic field distribution for different φ values. The dotted lines represent the position of the line scans presented in (a) and (b). The colour map is shown at the bottom of (c).

= 45° and 60°. On the other hand, in the case of hexagonal lattice, a weak diagonal interaction is observed in the field profile at $\varphi = 0°$ which enhances with increasing φ, thereby putting a significant contribution to the confining magnetic potential and diagonal channel in case of the hexagonal lattice. For both the lattices, the field lines display an asymmetric distribution attributed to the strong inhomogeneity in the demagnetizing field around the diamond antidot corners strengthening the possibilities of the presence of edge modes in the collective dynamics. The observed mode conversion phenomena from extended to localized mode or vice versa along with strong anisotropic modulation of spin-wave dynamics can be attributed to the variation of effective internal magnetic fields with the bias field orientation.

4.4 Conclusion

In summary, we investigated the ultrafast spin dynamics of $Ni_{80}Fe_{20}$ diamond antidot lattices (DADL) arranged in square and hexagonal geometry by varying the strength and in-plane orientation of the bias magnetic field employing TRMOKE magnetometry. The rich multimodal spin-wave spectra unlocked systematic variation with the strength of the applied bias field. The effect of the configurational anisotropy has been studied by varying the azimuthal angle of the bias magnetic field unveiling four-fold anisotropy for the square DADL while a signature of strong six-fold and a weak four-fold symmetry is observed in the anisotropic nature of spin-wave modes from hexagonally arranged DADL. The experimentally obtained spin-wave dynamics were qualitatively reproduced by micromagnetic simulations. Moreover, the calculated power and phase profiles gave deeper insights and enabled us to identify the mode conversion from quantized to extended or pseudo-extended mode taking place at different azimuthal orientations. In addition to this, the significant modulation in the simulated internal magnetostatic field distribution with in-plane angular variation crafted by both the lattice symmetry and the basis shape together was found to be solely responsible for such anisotropic modulation of magnonic spectra. The efficient tunability exhibited by the DADL is anticipated to be crucial from scientific as well as technological viewpoint and might come up with new possibilities in designing magnon-based on-chip communication devices in the GHz frequencies.

4.5 References

[1]B. Lenk, H. Ulrichs, F. Garbs, and M. Münzenberg, Physics Reports **507**, 107 (2011).
[2]V. V. Kruglyak, S. O. Demokritov, and D. Grundler, J Phys. D:Appl. Phys **43**, 264001 (2010).
[3]M. Krawczyk and D. Grundler, J Phys. Condens. Mater. **26**, 123202 (2014).
[4]A. Barman *et al.*, J Phys. Cond. Mater. (2021).
[5]F. Hellman *et al.*, Rev. Mod. Phys **89**, 025006 (2017).
[6]S. Panda, S. Mondal, J. Sinha, S. Choudhury, and A. Barman, Sci. Adv. **5**, eaav7200 (2019).
[7]V. E. Dmitrienko, E. N. Ovchinnikova, S. P. Collins, G. Nisbet, G. Beutier, Y. O. Kvashnin, V. V. Mazurenko, A. I. Lichtenstein, and M. I. Katsnelson, Nat. Phys **10**, 202 (2014).
[8]F. Guo, L. M. Belova, and R. D. McMichael, Phys. Rev. B **91**, 064426 (2015).
[9]X. S. Wang, H. W. Zhang, and X. R. Wang, Phys. Rev. Appl. **9**, 024029 (2018).
[10]R. Chisnell, J. S. Helton, D. E. Freedman, D. K. Singh, R. I. Bewley, D. G. Nocera, and Y. S. Lee, Phys. Rev. Lett. **115**, 147201 (2015).
[11]C. Liu *et al.*, Nat. Commun. **9**, 738 (2018).
[12]D. A. Bozhko, A. A. Serga, P. Clausen, V. I. Vasyuchka, F. Heussner, G. A. Melkov, A. Pomyalov, V. S. L'vov, and B. J. N. P. Hillebrands, Nat. Phys **12**, 1057 (2016).
[13]D. A. Bozhko, A. J. E. Kreil, H. Y. Musiienko-Shmarova, A. A. Serga, A. Pomyalov, V. S.

L'vov, and B. Hillebrands, Nat. Commun. **10**, 2460 (2019).
[14]C. Berk, M. Jaris, W. Yang, S. Dhuey, S. Cabrini, and H. Schmidt, Nat. Commun. **10**, 2652 (2019).
[15]Y. Tabuchi, S. Ishino, T. Ishikawa, R. Yamazaki, K. Usami, and Y. Nakamura, Phys. Rev. Lett **113**, 083603 (2014).
[16]Y. Tabuchi, S. Ishino, A. Noguchi, T. Ishikawa, R. Yamazaki, K. Usami, and Y. Nakamura, Science **349**, 405 (2015).
[17]J. Chen, C. Liu, T. Liu, Y. Xiao, K. Xia, G. E. W. Bauer, M. Wu, and H. Yu, Phys. Rev. Lett **120**, 217202 (2018).
[18]K. Adhikari, S. Sahoo, A. K. Mondal, Y. Otani, and A. Barman, Phys. Rev. B **101** (2020).
[19]D. Lachance-Quirion, Y. Tabuchi, A. Gloppe, K. Usami, and Y. Nakamura, Appl. Phys. Exp. **12**, 070101 (2019).
[20]Y. Li, W. Zhang, V. Tyberkevych, W.-K. Kwok, A. Hoffmann, and V. Novosad, J Appl. Phys. **128**, 130902 (2020).
[21]S. A. Nikitov, P. Tailhades, and C. S. Tsai, J Magn. Magn. Mater. **236**, 320 (2001).
[22]O. Martyanov, V. Yudanov, R. Lee, S. Nepijko, H. Elmers, R. Hertel, C. Schneider, and G. J. P. R. B. Schönhense, Phys. Rev. B **75**, 174429 (2007).
[23]S. McPhail, C. Gürtler, J. Shilton, N. Curson, and J. J. P. R. B. Bland, Phys. Rev. B **72**, 094414 (2005).
[24]S. Neusser, B. Botters, M. Becherer, D. Schmitt-Landsiedel, and D. Grundler, Appl. Phys. Lett. **93**, 122501 (2008).
[25]S. Neusser, B. Botters, and D. Grundler, Phys. Rev. B **78**, 054406 (2008).
[26]H. Ulrichs, B. Lenk, and M. Münzenberg, Appl. Phys. Lett. **97**, 092506 (2010).
[27]S. Tacchi, M. Madami, G. Gubbiotti, G. Carlotti, A. O. Adeyeye, S. Neusser, B. Botters, and D. Grundler, IEEE Trans. Magn. **46**, 172 (2010).
[28]S. Neusser, G. Duerr, H. G. Bauer, S. Tacchi, M. Madami, G. Woltersdorf, G. Gubbiotti, C. H. Back, and D. Grundler, Phys. Rev. Lett **105**, 067208 (2010).
[29]G. Venkat, D. Kumar, M. Franchin, O. Dmytriiev, M. Mruczkiewicz, H. Fangohr, A. Barman, M. Krawczyk, and A. Prabhakar, IEEE Trans. Magn. **49**, 524 (2013).
[30]D. Kumar, O. Dmytriiev, S. Ponraj, and A. Barman, J Phys. D:Appl. Phys **45**, 015001 (2011).
[31]D. Kumar and A. O. Adeyeye, J Phys. D:Appl. Phys **50** (2017).
[32]J. W. Kłos, D. Kumar, J. Romero-Vivas, H. Fangohr, M. Franchin, M. Krawczyk, and A. Barman, Phys. Rev. B **86**, 184433 (2012).
[33]S. Neusser, G. Duerr, S. Tacchi, M. Madami, M. L. Sokolovskyy, G. Gubbiotti, M. Krawczyk, and D. Grundler, Phys. Rev. B **84**, 094454 (2011).
[34]A. De, S. Mondal, S. Choudhury, S. Sahoo, S. Majumder, S. Barman, Y. Otani, and A. Barman, J Magn. Magn. Mater. **487** (2019).
[35]R. Mandal *et al.*, ACS Nano **6**, 3397 (2012).
[36]R. Mandal, S. Barman, S. Saha, Y. Otani, and A. Barman, J Appl. Phys. **118** (2015).
[37]S. Tacchi, M. Madami, G. Gubbiotti, G. Carlotti, A. O. Adeyeye, S. Neusser, B. Botters, and D. Grundler, IEEE Trans. Magn. **46**, 1440 (2010).
[38]A. Manzin and O. Bottauscio, J Phys. D:Appl. Phys **45** (2012).
[39]S. Pal, J. W. Klos, K. Das, O. Hellwig, P. Gruszecki, M. Krawczyk, and A. Barman, Appl. Phys. Lett. **105**, 162408 (2014).
[40]S. Choudhury, S. Majumder, S. Barman, Y. Otani, and A. Barman, Phys. Rev. Appl. **10** (2018).
[41]S.-K. Kim, K.-S. Lee, and D.-S. Han, Appl. Phys. Lett. **95**, 082507 (2009).
[42]V. E. Demidov, M. P. Kostylev, K. Rott, J. Münchenberger, G. Reiss, and S. O. Demokritov, Appl. Phys. Lett. **99**, 082507 (2011).

[43]K. Vogt, F. Y. Fradin, J. E. Pearson, T. Sebastian, S. D. Bader, B. Hillebrands, A. Hoffmann, and H. Schultheiss, Nat. Commun. **5**, 3727 (2014).
[44]H. Yu, G. Duerr, R. Huber, M. Bahr, T. Schwarze, F. Brandl, and D. Grundler, Nat. Commun. **4**, 2702 (2013).
[45]Y. Au, M. Dvornik, O. Dmytriiev, and V. V. Kruglyak, Appl. Phys. Lett. **100**, 172408 (2012).
[46]A. V. Chumak, A. A. Serga, and B. Hillebrands, Nat. Commun. **5**, 4700 (2014).
[47]T. Schneider, A. A. Serga, B. Leven, B. Hillebrands, R. L. Stamps, and M. P. Kostylev, Appl. Phys. Lett. **92**, 022505 (2008).
[48]A. Barman, S. Mondal, S. Sahoo, and A. De, J Appl. Phys. **128** (2020).
[49]S. Choudhury, S. Barman, Y. Otani, and A. Barman, ACS Nano **11**, 8814 (2017).
[50]S. Choudhury, S. Barman, Y. Otani, and A. Barman, J Magn. Magn. Mater. **489** (2019).
[51]A. De, K. Dutta, S. Mondal, S. Barman, Y. Otani, and A. Barman, Phys. Rev. B **103** (2021).
[52]S. Watanabe, V. S. Bhat, K. Baumgaertl, and D. Grundler, Adv. Func. Mat. **30**, 2001388 (2020).
[53]Y. Y. Dai, H. Wang, T. Yang, and Z. D. Zhang, J Magn. Magn. Mater. **483**, 70 (2019).
[54]V. S. Bhat, J. Sklenar, B. Farmer, J. Woods, J. T. Hastings, S. J. Lee, J. B. Ketterson, and L. E. De Long, Phys. Rev. Lett **111**, 077201 (2013).
[55]V. S. Bhat, J. Sklenar, B. Farmer, J. Woods, J. B. Ketterson, J. T. Hastings, and L. E. D. Long, J Appl. Phys. **115**, 17C502 (2014).
[56]F. Lisiecki *et al.*, Phys. Rev. Appl. **11**, 054061 (2019).
[57]J. Rychły, J. W. Kłos, and M. Krawczyk, J Phys. D:Appl. Phys **49**, 175001 (2016).
[58]V. Bhat, J. Woods, L. E. D. Long, J. T. Hastings, J. Sklenar, J. B. Ketterson, and M. Pechan, IEEE Trans. Magn. **49**, 1029 (2013).
[59]W. L. Zhang, R. J. Tang, H. C. Jiang, W. X. Zhang, B. Peng, and H. W. Zhang, IEEE Trans. Magn. **41**, 4390 (2005).
[60]S. Xu, J. Yin, R. Tang, W. Zhang, B. Peng, and W. Zhang, Phys. B: Condens. Matter **525**, 26 (2017).
[61]S. Goolaup, A. O. Adeyeye, and N. Singh, J Phys. D:Appl. Phys **38**, 2749 (2005).
[62]A. Barman, T. Kimura, Y. Otani, Y. Fukuma, K. Akahane, and S. Meguro, Rev Sci Instrum **79**, 123905 (2008).
[63]M. Donahue, D. G. Porter, NIST Interagency Report No. 6376; National Institute of Standard and Technology, Gaithersburg, MD, URL: http://math.nist.gov/oommf:(1999).
[64]K. H. J. Buschow, (2009).
[65]E. Beaurepaire, J. C. Merle, A. Daunois, and J. Y. Bigot, Physical Review Letters **76**, 4250 (1996).
[66]G. Malinowski, F. Dalla Longa, J. H. H. Rietjens, P. V. Paluskar, R. Huijink, H. J. M. Swagten, and B. Koopmans, Nat. Phys **4**, 855 (2008).
[67]D. Kumar, O. Dmytriiev, S. Ponraj, and A. Barman, J Phys. D:Appl. Phys **45** (2012).
[68]M. R. Scheinfein, LLG Micromagnetics Simulator, http://llgmicro.home.mindspring.com (accessed March 8, 2018).

Chapter 5

5. All-Optical Detection of Spin Pumping and Giant Interfacial Spin Transparency in $Co_2Fe_{0.4}Mn_{0.6}Si$/Pt Heterostructure

5.1 Introduction

Efficient generation and precise manipulation of pure spin current[1] have become pivotal aspects of contemporary spintronics[2] offering a robust mechanism to harness the spin degree of freedom in a myriad of low-dimensional systems[3,4]. As pure spin current consists of the flow of spin angular momentum devoid of net charge transfer, it holds the potential to minimize the Joule heating and Oersted fields[5] in a circuit promising the development of ultra-low-power computing technology. The active manipulation of pure spin current in a ferromagnet (FM)/nonmagnet (NM) thin film heterostructure has three crucial aspects, namely, generation, transport and absorption [6]. Various physical phenomena such as spin Hall effect (SHE)[7,8], spin caloric effects[9-12], spin pumping[13], non-local injection of spin[14,15], have been utilized for efficient generation of pure spin current in FM/NM heterostructures. Amongst those, spin pumping tenders an elegant method as it is free from the impedance mismatch problem[16]. This mechanism can be quantitatively treated in terms of spin-diffusion length of the NM and spin-mixing conductance[17] associated with the FM/NM interface. Additionally, for spin-orbit torque-based applications, interfacial spin transparency is a salient parameter determining the spin transfer efficiency. Interfacial spin transparency as a function of spin-mixing conductance and spin-diffusion length essentially measures the amount of spin that can effectively pass through the interface[18]. Therefore, from an application viewpoint, a large value of interfacial spin transparency is the key for improved device efficiency[19].

Very few reports are available in the literature exploring the potential of Heusler compound and heavy metal heterostructure in effective spin current manipulation using spin pumping [20,21]. Cobalt-based Heusler compounds are promising half-metallic materials [22] which gained considerable interest for their application potential in tunnel magnetoresistance (TMR) devices[23,24], spin-torque nano oscillator (STNO) with low switching current[25,26] etc. They can provide significant edge in the pure spin current manipulation over the other FM materials because of their ultra-low intrinsic magnetic damping[27-29] and stable spin-

polarized band structure[30]. $Co_2Fe_{0.4}Mn_{0.6}Si$ (CFMS, hereafter) shows high Curie temperature (~1000 K)[31], low Gilbert damping (0.004)[28] and its high spin polarization leads to superior TMR ratio than its peers. On the other hand, platinum is an archetypal heavy metal with high spin-orbit coupling (SOC) strength[32], and is popular for its giant spin Hall conductivity, low resistivity, high stability and efficiency as a spin reservoir in FM/NM heterostructures.

Incidentally, majority of the studies on spin pumping in the literature are carried out by studying inverse spin Hall effect (ISHE) employing all-electrical techniques such as ferromagnetic resonance (FMR). More recently, the all-optical time-resolved magneto-optical Kerr effect (TR-MOKE) has been used as a reliable and non-invasive technique to probe spin pumping including spin-mixing conductance, spin-diffusion length and interfacial spin transparency in FM/NM heterostructures [19,33]. This technique is devoid of any complex microfabrication of delicate waveguide structures. Besides, local measurement of magnetization dynamics directly in the time domain gives it a significant advantage in precise and reliable determination of magnetic damping parameter over the alternative techniques. Therefore, the objective of this study is to perform unambiguous measurement of spin pumping and related phenomena in CFMS/Pt heterostructures using the all-optical TRMOKE technique and to extract the important parameters as discussed above. From the experimental results, we have extracted the spin-mixing conductance and spin-diffusion length for the CFMS/Pt heterostructure using both the ballistic model[34-36] and the drift-diffusion model of spin transport[37,38], and thereby the interfacial spin transparency employing two different approaches, namely, the spin-Hall magnetoresistance model[39] and spin-transfer torque based model[40]. Moreover, we have compared the relative contributions from the spin pumping, spin memory loss (SML) and two-magnon scattering (TMS) at the interface to the magnetic damping parameter. This study will substantially enhance the in-depth understanding of the fundamental magnetic properties of Heusler compound-based FM/HM heterostructures and promote them as a promising candidate for future spin-orbitronic devices.

5.2 Experimental Details

5.2.1 Sample Fabrication

Thin films of CFMS Heusler compound were deposited on a 20 nm thick buffer layer of Cr grown on the top of a single crystalline MgO (001) substrate at room temperature using ultra-high vacuum-compatible magnetron sputtering at a base pressure below 1×10^{-7} torr. This was followed by in-situ annealing at 500 °C to promote the high-quality crystalline ordering of CFMS. After the in-situ annealing for CFMS layer, a Pt layer was deposited at room

temperature. The depositions were carried out typically at a rate of 0.01 Å/s with Ar pressure of 5 millitorr. Two series of films with stacks of MgO/Cr(20)/CFMS(d)/Pt(t) were prepared for the present investigation. For series I (S1-S6), the nominal CFMS layer thickness was varied as d = 10, 12, 14, 16, 20 nm while maintaining a constant thickness of Pt layer at t = 5 nm. For series II (S7-S12), the Pt layer thickness was varied as t = 1, 2, 3, 4, 8, 12 nm, keeping a constant thickness of CFMS layer at d = 16 nm. A 2 nm thick capping layer made of Al was deposited on top of all the sample stacks to protect those from any external degradation including oxidation due to exposure in the atmosphere as well as to the femtosecond laser. For convenience, we have listed the sample names and nominal thickness values in table 5.1.

5.2.2 Measurements

In-situ reflection high energy electron diffraction (RHEED) images of the samples were acquired to investigate the surface structural quality of the thin films. On the other hand, *ex-situ* out-of-plane and tilted x-ray diffraction (XRD) patterns in θ-2θ geometry were measured to reveal the crystalline phase information and atomic site ordering in the thin films. Atomic force microscopy (AFM) was used to probe the average surface roughness and the topography of the sample stacks and a standard four-probe technique was used to measure the resistivity. Static magnetic properties were measured using a vibrating sample magnetometer (VSM) at room temperature. A custom-built all-optical time-resolved magneto-optical Kerr effect (TRMOKE) magnetometer based on two-colour optical pump-probe setup in a non-collinear geometry was employed to measure the ultrafast magnetization dynamics from the samples. Here the fundamental laser beam (wavelength, λ = 800 nm, full width at half maximum, FWHM ≈ 40 fs) from an amplified femtosecond laser source (Libra, Coherent Inc.) was split into two parts using a 30:70 beam splitter and the weaker part is used as probe and the second harmonic of the stronger part of this beam (λ = 400 nm, FWHM > 40 fs) was used as pump to excite the dynamics in the sample. The pump beam has a larger spot size (~400 μm) on the sample surface as opposed to that of the probe beam (~100 μm) ensuring the detection of local dynamics from a uniformly excited zone. The pump beam was obliquely incident on the sample, while the probe beam was incident normal to the sample plane so that the polar Kerr rotation is measured from the sample using a polarized beam splitter and two separate photodiodes. A variable magnetic field was applied to the sample at a small angle (~15°) from the sample plane, the in-plane component of which (H) is referred to as the bias magnetic field. An optical chopper was used to modulate the pump beam at 373 Hz and Kerr rotation and

reflectivity were recorded by two separate lock-in amplifiers in a phase-sensitive manner avoiding any possible breakthrough of one into another.

5.3 Results and Discussion

5.3.1 Structural Characterization

The crystalline phase and atomic-site ordering play non-trivial roles in the determination of the magnetic properties of Heusler compounds[22,41]. Therefore, before proceeding to the investigations of dynamic magnetic properties, we have performed some important structural characterizations of the deposited samples systematically. In fig. 5.1(a), XRD data measured in usual θ-2θ geometry are shown for a few representative samples from both series I and II. The presence of a strong diffraction peak from CFMS (400) at 66.3° suggests good crystalline growth of CFMS associated with cubic lattice symmetry, whereas a clear diffraction peak at 31.8° from CFMS (200) strongly indicates the formation of B2 lattice ordering for all the CFMS layers under investigation. A tilted XRD scan presented in fig. 5.1(b) shows no clear CFMS (111) peak, thereby ruling out the possibility of any admixture of $L2_1$ phase in the lattice

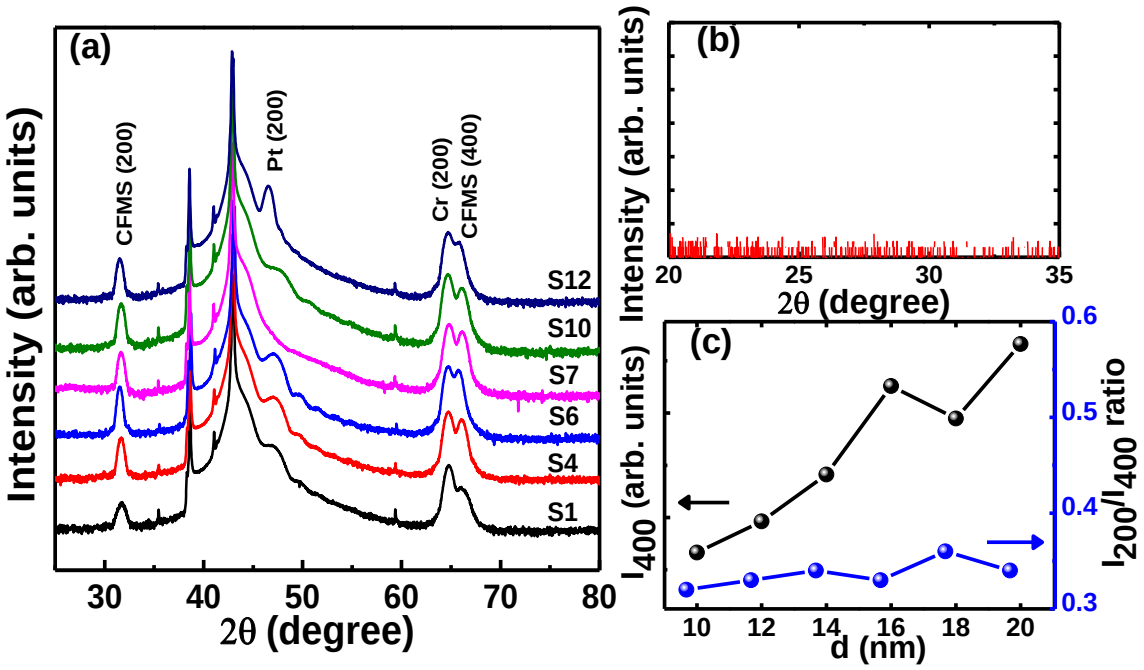

Figure 5.1: (a) XRD patterns for the MgO (sub)/Cr/CFMS/Pt/Al samples measured in conventional θ-2θ geometry. Intense diffraction Peaks from CFMS (200), CFMS (400) and Pt (200) are identified along with Cr (200) peak. (b) The tilted XRD scan showing no prominent peak from CFMS (111) indicating the absence of $L2_1$ structural phase. (c) Intensity of CFMS (400) diffraction peak is found to increase with CFMS layer thickness whereas the integrated intensity ratio between CFMS (200) and CFMS (400) peaks remains thickness invariant suggesting a stable Co-atomic site ordering

ordering. Careful observation reveals that both the intensities of the CFMS (200) and CFMS (400) superlattice peaks are increasing for the case of S1 (d = 10 nm) to S3 (d = 20 nm) which are in consonance with the increasing nominal thickness. As a previous report[41] presented a thickness dependent ordering for CFMS, we have calculated the integrated intensity ratio of CFMS (200) to CFMS (400) diffraction peaks as shown in fig 5.1(c). Though an increasing trend in the intensity of CFMS (400) peak signifies an improvement of cubic crystalline structure, the nearly constant value of the integrated intensity ratio confirms a very stable atomic-site ordering of Co-atoms within the compound structure. The degree of lattice strain can also be qualitatively understood from the analysis of Pt (100) peak, which is presented in section 9.1 of Appendix B.

To understand the nature of oriented growth of the CFMS and Pt thin film layers along the MgO [100] and MgO [110] directions, in-situ RHEED images have been acquired. The images for CFMS and Pt layers are depicted in fig. 5.2(a) for the sample S4. The prominent streaks observed in the images confirm the epitaxial growth of both the CFMS and Pt layers. The

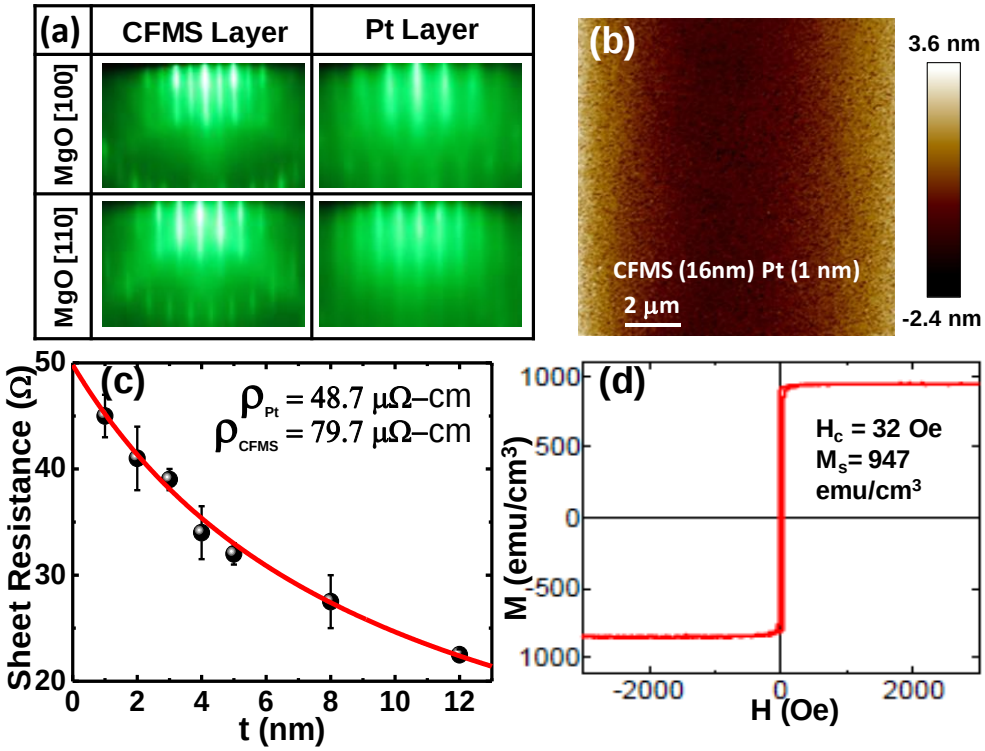

Figure 5.2: (a) In-situ RHEED patterns exhibiting clear streaks along MgO [100] and MgO [110] crystallographic directions obtained from CFMS and Pt layers. (b) Measurement of mean surface roughness from AFM image. (c) Variation of sheet resistance of the heterostructure as a function of Pt layer thickness. (d) Representative result of magnetization vs magnetic field from in-plane VSM measurements for S1 sample showing extraction of coercive field and saturation magnetization.

CFMS (001) and Pt (001) planes have grown on the MgO (001) plane. In addition, the CFMS [110] and Pt [100] directions have aligned parallel to the MgO [100] direction. Here, the Cr layer acts as a buffer layer which promotes the epitaxial growth of layers by reducing the lattice mismatch between MgO and CFMS layer. Previous studies suggested the achievement of a better crystalline ordering after post-deposition annealing [29,42] which is reconfirmed by the RHEED patterns from all the samples. From these RHEED observation, we found the following epitaxial relationship: MgO (001) || Cr (001) || CFMS (001) || Pt (001) and MgO [100] || Cr [110] || CFMS [110] || Pt [100].

The AFM image revealing the surface topography for a particular sample (S7) is presented in fig. 5.2(b). The mean surface roughness calculated over a large area shows a fairly small value of 0.48 nm. The average topographical roughness corresponding to all the samples are of the same order. However, for the heterostructure, interface roughness for the individual layers significantly contribute to the control the spin transport across the interface. Layer thickness and roughness values estimated from the simulation of X-ray reflectivity measurement data are presented in table 5.1. For further details, please refer to section 9.2 of Appendix B.

Table 5.1: Coercive field and saturation magnetization values extracted from VSM measurements along with thickness and roughness estimated from XRR data for MgO (sub)/Cr(20)/CFMS(*d*)/Pt(*t*)/Al(2) samples

S	Measured from VSM		Nominal Thickness		Thickness and roughness extracted from XRR							
	H_c (Oe)	M_s (emu/cc)	CFMS	Pt	Cr (buffer)		CFMS		Pt		Al (capping)	
			d (nm)	*t* (nm)	*d* (nm)	σ (nm)	*d* (nm)	σ (nm)	*t* (nm)	σ (nm)	*d* (nm)	σ (nm)
S1	32	947	10	5	20.28	0.60	10.15	0.21	5.50	0.39	2.20	0.30
S2	32	902	12	5	20.08	0.30	12.01	0.40	5.70	0.36	2.10	0.60
S3	34	888	14	5	20.28	0.50	14.02	0.28	5.60	0.44	2.00	0.60
S4	30	922	16	5	20.68	0.30	16.01	0.22	6.00	0.45	2.00	0.21
S5	26	868	18	5	20.38	0.59	18.04	0.33	5.85	0.53	2.00	0.50
S6	24	896	20	5	20.58	0.30	20.01	0.21	5.75	0.45	2.00	0.60
S7	24	909	16	1	20.05	0.29	16.00	0.39	1.70	0.33	1.90	0.69
S8	33	875	16	2	20.35	0.33	15.97	0.27	2.84	0.47	1.29	0.68
S9	22	923	16	3	20.56	0.42	16.20	0.31	3.70	0.48	2.73	0.48
S10	30	871	16	4	20.06	0.22	16.10	0.21	4.78	0.35	2.33	0.38
S11	22	856	16	8	20.94	0.30	15.80	0.32	8.90	0.45	2.01	0.35
S12	25	895	16	12	20.44	0.20	15.20	0.29	12.50	0.45	2.00	0.26

Fig. 5.2(c) displays the variation of the sheet resistance of the heterostructure as a function of the platinum layer thickness. The resistance vs thickness data are fitted using a standard parallel

combination of resistance model and the resistivities of the CFMS and Pt layers are calculated as $79.7 \pm 1.1\ \mu\Omega.\,\mathrm{cm}$ and $48.7 \pm 0.8\ \mu\Omega.\,\mathrm{cm}$ respectively.

5.3.2 Static Magnetic Properties

The magnetic hysteresis behaviour of all samples has been studied using VSM at room temperature. Fig. 5.2(d) shows a typical plot of magnetization vs in-plane applied magnetic field of S1 sample along the easy axis of CFMS ([110] direction) which reveals a square hysteresis loop for the sample. The estimated saturation magnetization (M_s) and coercive field (H_c) values for all samples are presented in table 5.1. The M_s values differ slightly from one another and show about 10-18% reduction from the bulk value of 1050 emu/cc[41]. The H_c values for the samples are found to be small having an upper bound of ~35 Oe.

5.3.3 Investigation of Damping Constant from All-Optical TRMOKE Measurement

The phenomenon of spin pumping at the CFMS/Pt interface is schematically depicted in fig. 5.3(a) along with the optical pump-probe measurement geometry. A typical TRMOKE result presented in fig. 5.3(b) comprises of signatures from different physical phenomena associated with a magnetic system in the femtosecond to nanosecond timescale. When an ultrashort laser pulse is incident upon a ferromagnetic surface, a sudden drop in magnetization is observed referred to as the ultrafast demagnetization[43]. The magnetization then exhibits a recovery via spin-lattice relaxation giving rise to the fast relaxation process. The third regime essentially consists of the slow relaxation process superimposed with spin precession where the energy is redistributed from the system to the surroundings and the system reclaims its initial magnetization[44]. To find the magnetic damping, it is imperative to calculate the effective magnetization and the characteristic decay time associated with the precession of spins. To execute this, the precessional Kerr oscillations, after eliminating the bi-exponential background caused by the relaxation, are fitted with a sinusoidal function with decaying amplitude of the following form:

$$\theta_k(t) = Ae^{-\frac{t}{\tau}} sin(2\pi\nu t + \varphi) \tag{5.1}$$

where τ is the decay constant of the spin precessional motion with frequency ν and amplitude A. Time-resolved Kerr oscillations are measured at different strengths of the bias magnetic field and the corresponding frequency values have been calculated from the fast Fourier transform (FFT) spectra. We plot the bias magnetic field dependence of the precessional frequency and the effective magnetization has been extracted for all samples from theoretical fit using the Kittel formula for uniform precessional mode given below[45,46]:

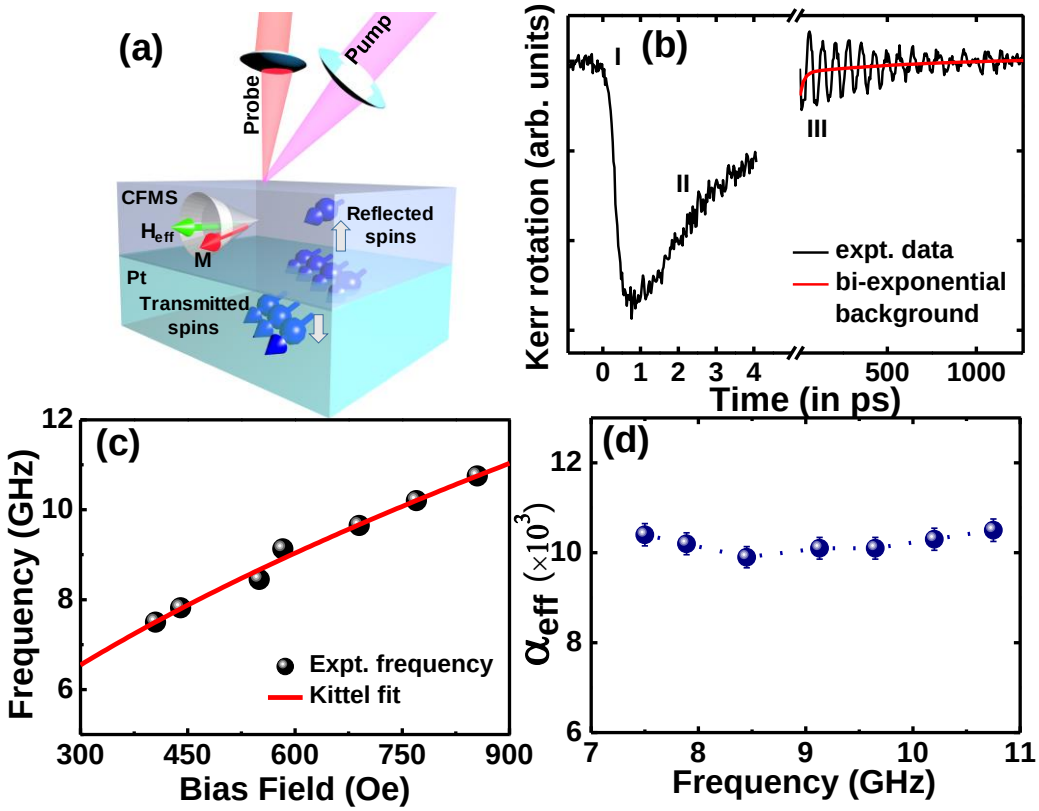

Figure 5.3: (a) Schematic representation of spin pumping mechanism in CFMS/Pt interface measured employing non-collinear pump-probe arrangement (b) Three different regimes present in a typical TRMOKE data from the MgO(sub)/Cr(20)/CFMS (10)/Pt (5)/Al heterostructure at *H*=1.0 kOe. The bi-exponential background fitting is shown in red solid line. (c) Bias field dependence of the precessional frequency measured for sample S1 fitted with Kittel formula. (d) Effective Gilbert damping extracted for sample S1 showing nearly frequency-independent values.

$$\nu = \frac{\gamma}{2\pi}\sqrt{(Hcos(\theta_H - \theta_M) + H_a)(Hcos(\theta_H - \theta_M) + H_b)} \tag{5.2}$$

where $\gamma = {}^{g\mu_B}/_{\hbar}$; g, μ_B and $\hbar$ being the Lande g-factor, Bohr magneton and reduced Planck's constant respectively and H represents the bias magnetic field. θ_H and θ_M are the respective angles between in-plane easy axis with the applied bias field orientation and direction of magnetization. H_a and H_b are the contributions from two-fold and four-fold anisotropies and are given by[45]:

$$H_a = \frac{2K_2}{M_s}cos\,2\theta_M + \frac{2K_4}{M_s}cos\,4\theta_M$$

$$H_b = 4\pi M_s + \frac{2K_z}{M_s} - \frac{2K_2}{M_s}sin^2\,\theta_M + \frac{K_4}{M_s}(2 - sin^2(2\theta_M)) \tag{5.3}$$

where K_2, K_4 and K_z are in-plane uniaxial, cubic crystalline and out-of-plane anisotropy constant.

Further details of the Kittel fit parameters along with the values of anisotropic constants can be found in the Appendix B (section 9.3). The effective damping (α_{eff}) constant is then extracted employing the following relation[45,47]:

$$\alpha_{eff} = \frac{2}{\gamma\tau(2Hcos(\theta_H - \theta_M) + H_a + H_b)} \tag{5.4}$$

In fig. 5.3(c) we have shown the uniform precessional mode frequencies as obtained from sample 1 at different bias magnetic field strengths. The field dependent dynamics has been fitted with the Kittel formula given by eq. 5.2 to extract the K_2, K_4 and K_z. We have also extracted α_{eff} at different bias magnetic field strengths. A plot of α_{eff} vs precession frequency for S1 shown in fig. 5.3(d) revealed that α_{eff} is nearly invariant with precession frequency. As magnetic damping is highly correlated to atomic site ordering in CFMS[41], a nearly frequency-independent value of α_{eff} can be attributed to a stable B2 structure observed for the studied samples and indicates the absence of any significant amount of inhomogeneous anisotropy distribution and two-magnon scattering (TMS)[48] due to the presence of surface and volume impurities[42]. Nevertheless, we have extracted the precise contribution of TMS later in this article.

5.3.4 Modulation of Damping as a Route to Probe Spin Pumping

In an FM/NM heterostructure, apart from the intrinsic Gilbert damping, there can be various other physical mechanisms contributing to the magnetic damping such as spin pumping, two-magnon scattering, spin memory loss, etc. In a non-local contribution to damping like spin pumping, the FM layer acts as a source of spin current and the optically induced spin current in the FM layer flows through the FM/NM interface and finally dissipates in the adjacent NM layer acting as an absorption medium for spin current or a spin sink. This leads to an enhancement in the effective damping. This phenomenon is theoretically modelled by Tserkovnyak et al. using a modified Landau-Lifshitz Gilbert equation given below[13]:

$$\frac{d\boldsymbol{m}}{dt} = -\gamma(\boldsymbol{m} \times \boldsymbol{H_{eff}}) + \alpha_0\left(\boldsymbol{m} \times \frac{d\boldsymbol{m}}{dt}\right) + \frac{\gamma}{VM_s}\boldsymbol{I_s} \tag{5.5}$$

Here, α_0 is the intrinsic Gilbert damping and V is the volume of the FM layer. The net spin current $\boldsymbol{I_s}$ consists of a DC contribution $\boldsymbol{I_s^0}$ which is null for the present case, pumped spin current $\boldsymbol{I_s^{pump}}$ from FM layer and a spin backflow current $\boldsymbol{I_s^{back}}$ from NM layer to FM layer since a practical NM material might not act as an ideal spin sink. Thus,

$$\boldsymbol{I_s} = \boldsymbol{I_s^0} + \boldsymbol{I_s^{pump}} + \boldsymbol{I_s^{back}} \tag{5.6}$$

The effect of a backflow of spin current from the NM to FM layer can be quantified by β as[49,50]:

$$\beta = \left[2\pi G_{\uparrow\downarrow}\sqrt{\frac{\epsilon}{3}}\tanh(\frac{t}{\lambda})\right]^{-1} \tag{5.7}$$

which depends on the spin-diffusion length (λ) of the NM medium.

Here, ϵ is the spin-flip probability given by [51,52]:

$$\epsilon = \left(\frac{Z_{Pt}e^2}{\hbar c}\right)^4 \tag{5.8}$$

whose value is obtained as 0.105 using Z_{Pt} = 78 for platinum and $\frac{e^2}{\hbar c}$ is the fine structure constant = $^1/_{137}$

However, the transport of spin current through the interface is characterized by intrinsic and effective spin-mixing conductance. The effective spin-mixing conductance takes care of the spin backflow factor, and as the thickness of the NM layer enhances, it approaches the intrinsic spin-mixing conductance asymptotically in the regime of no or negligible backflow current. In the ballistic spin transport approach, the relation between spin-mixing conductance and enhancement of damping can be modelled as[35,36]:

$$G_{eff} = G_{\uparrow\downarrow}\,(1 - e^{-\frac{2t}{\lambda}}) \tag{5.9}$$

$$G_{eff} = \frac{4\pi d M_s \Delta\alpha}{g\mu_B} = \frac{4\pi d M_s}{g\mu_B}(\alpha_{eff} - \alpha_0) \tag{5.10}$$

Since the ballistic model does not take the resistivity of the NM layer into consideration, an alternative model based on drift-diffusion framework[37,38] provides another functional relation between spin-mixing conductance and modulation of damping:

$$G_{eff} = \frac{G_{\uparrow\downarrow}}{1 + \frac{e^2\lambda\rho G_{\uparrow\downarrow}}{h}coth(\frac{t}{\lambda})} \tag{5.11}$$

where ρ is the resistivity of the NM and the reverse flow of the spin current is represented by the hyperbolic cotangent term present in the denominator.

Now, according to the spin Hall magnetoresistance model, the detected spin current at the NM layer is smaller than the spin current pumped out of the FM layer. This reduction can indicate many possible physical factors like the presence of local disorder and intermix at the FM/NM interface accompanied by electronic band mismatch etc. In the spin Hall magnetoresistance (SHM) model[39], interfacial spin transparency (T) parametrizes all these hindrances and is correlated with G_{eff} by the following relation:

$$T = \frac{G_{eff}\, tanh(\frac{t}{2\lambda})}{G_{eff} coth(\frac{t}{2\lambda}) + \frac{h}{2e^2\lambda\rho}} \,. \tag{5.12}$$

However, in the spin-transfer torque (STT)-based model the spin backflow factors are neglected. In the higher thickness regime of both the FM and NM layer and the interfacial spin transparency attains the following form[40]:

$$T = \frac{\frac{2G_{\uparrow\downarrow}}{G_{NM}}}{1 + \frac{2G_{\uparrow\downarrow}}{G_{NM}}} \tag{5.13}$$

where $G_{NM} = \frac{h}{e^2\lambda\rho}$ refers to as the spin conductance for the platinum layer here.

In a heterostructure like the one under investigation, there could be other physical effects playing a role in the observed modulation of damping. The spin angular momentum exerted by the precessing spins in the FM layer can suffer a loss at the interface due to spin memory loss (SML)[53], two-magnon scattering (TMS) etc. Whereas the spin-orbit coupling at the interface or proximity induced interfacial depolarization leads to the SML and consequent enhancement of damping, the creation of degenerate magnon modes from an initially uniform FMR mode caused by the surface inhomogeneity scattering centres, leads to TMS effect[54]. Inclusion of these two effects into the effective damping gives the following modified set of expressions[19,55]:

$$\alpha_{eff} = \alpha_0 + \alpha_{SP} + \alpha_{SML} + \alpha_{TMS}$$

$$\alpha_{eff} = \alpha_0 + \frac{g\mu_B}{4\pi d M_{eff}}\left(G_{eff} + G_{SML}\right) + \frac{\beta_{TMS}}{d^2}. \tag{5.14}$$

G_{SML} is the spin conductance due to SML and β_{TMS} is the TMS coefficient depending on the defect density and perpendicular magnetic anisotropy in the FM layer.

5.3.5 Investigation of Thickness-Dependent Enhancement of Damping

The bi-exponential background subtracted precessional Kerr oscillations recorded at H= 1.0 kOe are presented in fig. 5.4(a) where the NM layer thickness is varied as $1 \leq t \leq 12$ nm for the sample Sub/Cr(20)/CFMS(16)/Pt(t)/Al(2) (shown schematically in fig. 5.4(b). A non-monotonic variation of α_{eff} is observed with t as presented in fig. 5.4(c). In the lower thickness regime, i.e. t < 4 nm, α_{eff} increases rapidly but for $t \geq 4$ nm, it starts to saturate and asymptotically approaches a value of 8.5×10^{-3}. This result is fitted using the ballistic model of spin transport with eq. (5.9) and (5.10) to estimate the intrinsic spin-mixing conductance, $G_{\uparrow\downarrow} = (6.51 \pm 0.21) \times 10^{15}$ cm^{-2} and the characteristic spin-diffusion length for platinum layer, $\lambda =$

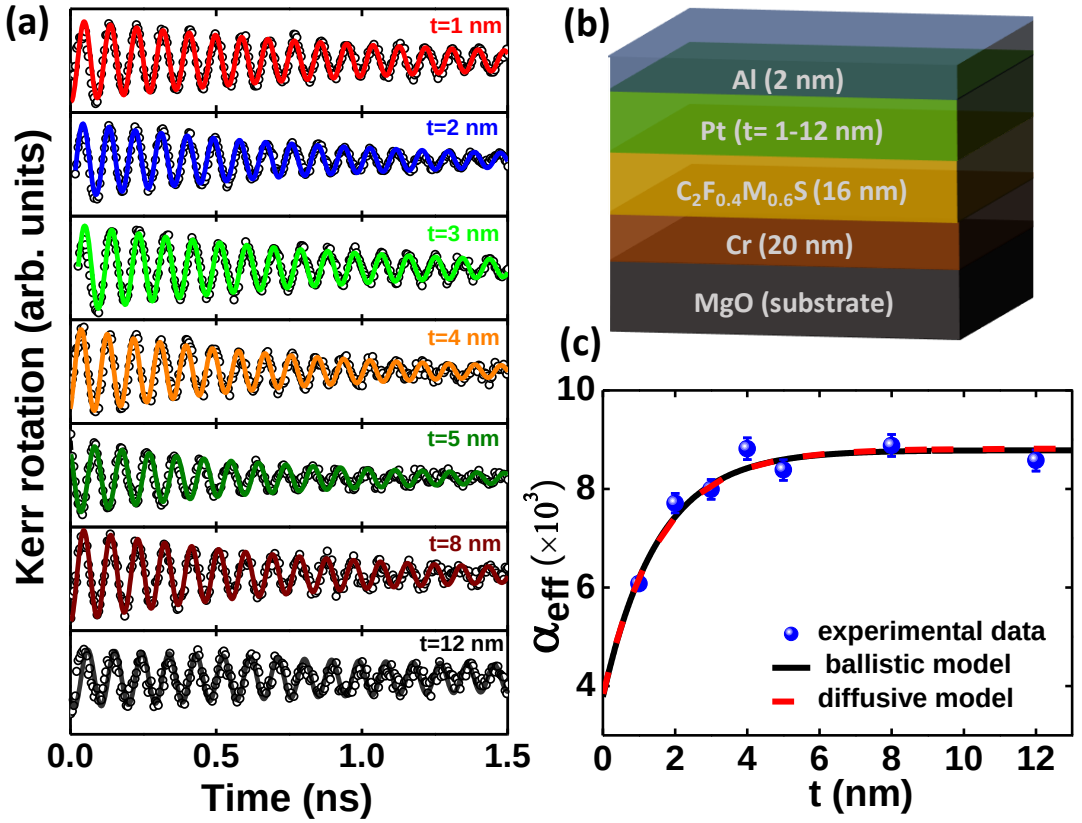

Figure 5.4: (a) Background subtracted time-resolved Kerr rotation data for samples with Pt thickness t = 1, 2, 3, 4, 5, 8 and 12 nm recorded at H = 1.0 kOe (b) Schematic representation of the corresponding sample with varying thickness of the Pt layer. (c) Variation of α_{eff} as a function of t. The solid and dashed lines represent the theoretical fits employing the ballistic and drift-diffusive spin transport model, respectively to extract the intrinsic spin-mixing conductance and the spin-diffusion length

3.06 ± 0.29 nm. Moreover, we have further fitted our results employing eq. (5.10) and (5.11) as suggested by the spin diffusive model resulting $G_{\uparrow\downarrow} = (1.23 \pm 0.11) \times 10^{16}$ cm^{-2} and $\lambda = 3.23 \pm 0.11$ nm as a fitting parameter. Unlike the ballistic approach that assumes a fast spin current transfer in the regime of $t << \lambda$, the resistivity of Pt is taken into consideration in the calculation of $G_{\uparrow\downarrow}$ by the diffusion model giving a higher estimate of spin-mixing conductance. The differences in the way the spin backflow is incorporated in both frameworks can be attributed to the differences in the estimated value of $G_{\uparrow\downarrow}$. However, the values obtained for spin-diffusion length using both the models are close enough and also are in agreement with the existing literature [53,56]. From eq. (5.8), we have calculated the spin-flip probability for platinum as ϵ = 0.105 as mentioned above and the corresponding β as (1.40 ± 0.11) × 10^{-16} cm^2 from eq. (5.7) for the sample with t = 12 nm. Here, β exhibits a strong width dependent modulation (up to 74%) and attains its maximum value of (2.44 ± 0.22) × 10^{-16} cm^2 for the sample with the lowest Pt layer thickness, t = 1 nm.

Investigation of precessional dynamics for the other set of samples Sub/Cr(20)/CFMS(d)/Pt(5)/Al(2) where the FM layer thickness (d) was varied as $10 \leq d \leq 20$ nm provides an avenue for direct experimental determination of G_{eff}. The time-resolved Kerr rotational data for these samples measured at H= 1.0 kOe are presented in fig 5.5(a). A plot of α_{eff} vs $1/d$ (fig. 5.5(b)) shows an almost linear behaviour. The experimental result is fitted with the theoretical expression given by eq. (5.10) to derive the values of α_0 and G_{eff} to be 0.0039 ± 0.0004 and (6.08 ± 0.12) × 10^{15} cm^{-2}, respectively.

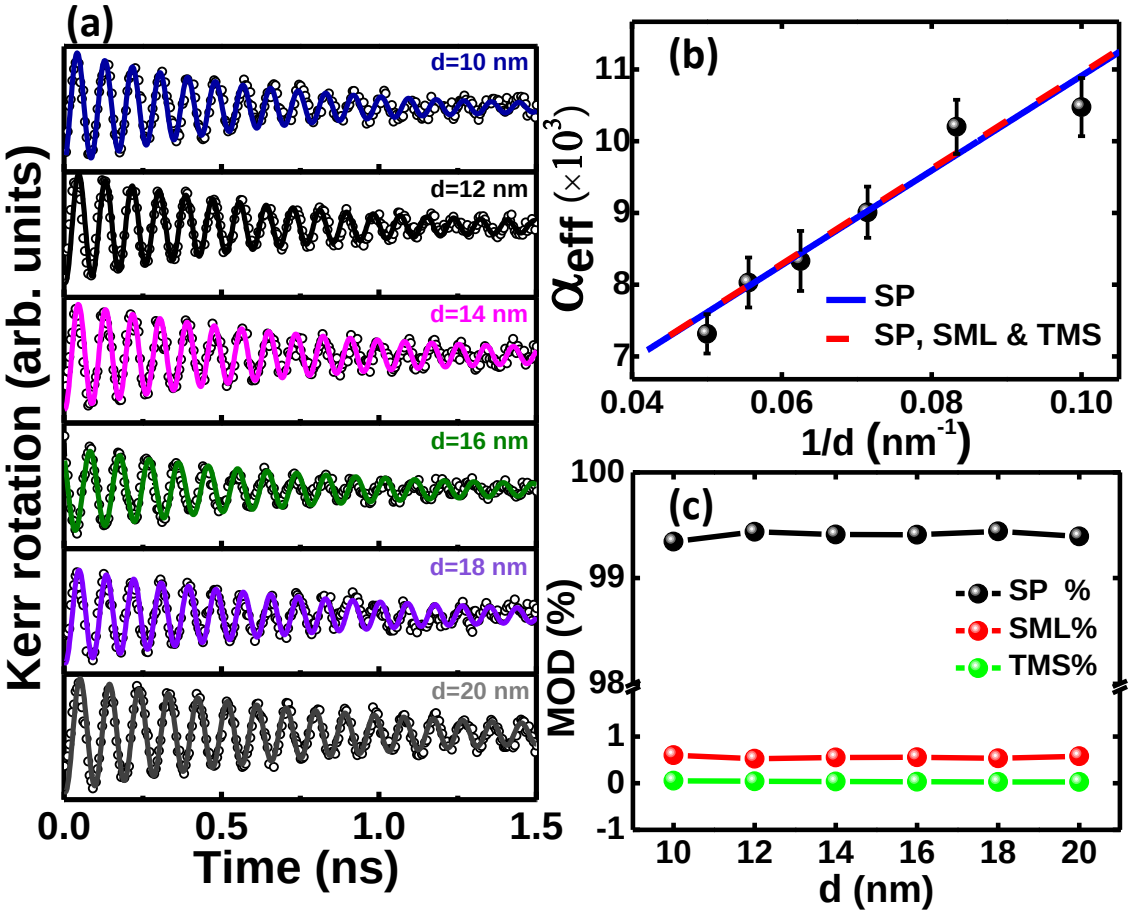

Figure 5.5: (a) Background subtracted time-resolved Kerr rotation data for samples with CFMS thickness 10,12,14,16,18 and 20 nm obtained at H=1.0 kOe. (b) Enhancement of effective Gilbert damping with inverse of CFMS layer thickness is shown. The blue solid line represents the theoretical fit considering spin pumping only whereas red dashed line represents fitting with contributions from spin memory loss (SML) and two-magnon scattering (TMS) taking into consideration. (c) Percentage contribution in modulation of damping (MOD) from spin pumping, SML and TMS across the thickness range of CFMS layer

Subsequently, to disentangle any possible contributions of SML and TMS at the interface from that of spin pumping in the modulation of damping, we have further fitted the results using a modified expression for α_{eff} as given by eq. (5.14). From this fit, we have extracted the value of G_{SML} = (3.21 ± 0.15) × 10^{13} cm^{-2} and the coefficient for TMS is found to be β_{TMS} = (3.57 ±

0.21) × 10^{-18} cm^2 which shows that the contributions of SML and TMS in the modulation of damping are negligible in comparison to that of spin pumping. Their relative contributions and plotted in fig 5.5(c), which confirm that the effects of spin pumping is far more dominant for the systems under investigation. It is to be noted that the value of G_{eff} obtained for the CFMS/Pt interface is significantly higher than the value for other FM/NM heterostructures, as shown in table 5.2, promoting this system as a strong candidate for spin-orbit torque (SOT)-based devices.

Table 5.2: Comparison of effective spin mixing conductance and interfacial spin transparency obtained from present work with the values reported in the literatures

NM/FM Material Systems	Spin Mixing Conductance	Interfacial Spin Transparency
Material Interfaces with Pt		
Pt/Py[18]	1.52	0.25
Pt/Co[18]	3.96	0.65
Pt/FM[40]	0.6-1.2	0.34-0.67
Pt/YIG[57]	0.3-1.2	NA
Pt/Fe[58,59]	2.0-4.4	NA
Pt/$Co_{50}Fe_{50}$[60]	2.5	NA
Material Interfaces with Heuslers		
β-Ta/Co_2FeAl[61]	2.90	0.68
Co_2FeAl/Mo[62]	1.56	NA
MoS_2 /Co_2FeAl[63]	1.49	0.46
Co_2FeAl/Cu/β-Ta[64]	3.40	NA
Material Interfaces with Heuslers and Pt		
Co_2MnSi/Pt[65]	6.5-9.0	NA
$Co_2FeAl_{0.5}Si_{0.5}$/Pt[66]	2.1-3.7	NA
$Co_2Fe_{0.4}Mn_{0.6}Si$/Pt [this work]	6.5-12.3	0.87

We have further measured the resistivity of the Pt layer and used G_{eff} as obtained above to extract the interfacial spin transparency, *T*. As *T* depends on the electronic band matching of the metals in an FM/NM junction, it is an electronic property of the interface and a higher value of *T* is always desirable for energy-efficient SOT applications. We have found $T = 0.84 \pm 0.03$ using the eq. (12) considering the SHM model, while eq. (13) from STT-based model yields $T = 0.87 \pm 0.02$ which is slightly higher than that obtained from SHM. From the table 5.2, it is evident that the interfacial transparency value that we obtained from the present study is highest among the available literature reports on various FM/NM systems involving heavy metals. Interfacial spin transparency essentially expresses the probability of transfer of spins across the interface of ferromagnet and non-magnet interface. As it is a function of effective spin mixing

conductance, it will highly depend on the spin-orbit coupling strength of the NM material involved. Apart from this, interface band structure matching, presence of lattice defects and dislocations, Fermi velocity are some of the crucial factors[63] governing the efficiency of spin transport and thereby implicitly contribute to manipulation of spin transparency. The spin density of states (DOS) at the Fermi level directly correlates with the Gilbert relaxation parameter and associated damping[67].

$$G \propto \xi^2 D(E_F) \tag{5.15}$$

Also, G has a linear relationship with damping

$$G = \gamma \alpha M_s \tag{5.16}$$

Therefore,

$$\alpha \propto \xi^2 D(E_F) \tag{5.17}$$

ξ spin orbit coupling (SOC) parameter is very small for CFMS and constant for Pt. Also, Pt being a metal will possesses high DOS at the Fermi level. Thus, for Pt both high SOC strength and large occupancy at the Fermi level controls the rapid dissipation strong spin angular momentum inflow from the CFMS layer and strongly enhances the effective damping. Therefore, both the material choice as well as careful engineering of the interface play crucial role in observed large T. The giant interfacial spin transparency value essentially suggests the ease of spin transfer through a favourable CFMS/Pt interface and ushers superior application potential of CFMS/Pt heterostructure in pure spin current-based devices.

5.4 Conclusion

We have extensively investigated spin pumping and related phenomena in the CFMS/Pt heterostructure employing a non-invasive and reliable all-optical time-resolved magneto-optical Kerr effect technique. A strong but linear enhancement of effective damping is observed with increasing CFMS layer thickness whereas an initial exponential rise followed by saturation in damping is found with a systematic variation of Pt layer thickness in the range of 1 to 12 nm. The relationship between effective damping and the thickness of the CFMS layer has been modelled to extract the intrinsic Gilbert damping to be 0.0039 ± 0.0004 and effective spin-mixing conductance to be (6.08 ± 0.12) × 10^{15} cm^{-2} . The results for variation of effective damping with Pt thickness have been modelled employing ballistic spin transport as well as drift-diffusive based framework for spin transport to extract the intrinsic spin-mixing conductance values of (6.51 ± 0.21) × 10^{15} cm^{-2} and (1.23 ± 0.11) × 10^{16} cm^{-2}, respectively. Furthermore, we have isolated the contributions from spin memory loss and two magnon scattering to damping and found them to be negligible to that from spin pumping. The T value

is also estimated to be 0.84 ± 0.03 and 0.87 ± 0.02 using the spin Hall magnetoresistance model and spin-transfer torque model, respectively. The value of T is one of the highest reported values in such FM/NM heterostructure so far. The large interfacial transparency in conjunction with the high value of effective spin-mixing conductance and small intrinsic Gilbert damping strongly place the CFMS/Pt heterostructure as a potential candidate for SOT-based new generation storage and memory devices.

5.5 References

[1]A. Hoffmann, Phys Status Solidi C **4**, 4236 (2007).
[2]S. D. Bader and S. S. P. Parkin, Annu. Rev. Condens. Matter Phys **1**, 71 (2010).
[3]A. Hirohata, K. Yamada, Y. Nakatani, I. L. Prejbeanu, B. Dieny, P. Pirro, and B. Hillebrands, J Magn. Magn. Mater. **509**, 166711 (2020).
[4]I. Žutić, J. Fabian, and S. Das Sarma, Rev. Mod. Phys **76**, 323 (2004).
[5]C. Chappert and J.-V. Kim, Nat. Phys **4**, 837 (2008).
[6]F. Hellman *et al.*, Rev. Mod. Phys **89**, 025006 (2017).
[7]J. E. Hirsch, Phys. Rev. Lett **83**, 1834 (1999).
[8]J. Sinova, S. O. Valenzuela, J. Wunderlich, C. H. Back, and T. Jungwirth, Rev. Mod. Phys **87**, 1213 (2015).
[9]K. Uchida, S. Takahashi, K. Harii, J. Ieda, W. Koshibae, K. Ando, S. Maekawa, and E. Saitoh, Nature **455**, 778 (2008).
[10]W. Lin, M. Hehn, L. Chaput, B. Negulescu, S. Andrieu, F. Montaigne, and S. Mangin, Nat. Commun. **3**, 744 (2012).
[11]G. E. W. Bauer, E. Saitoh, and B. J. van Wees, Nat. Mater. **11**, 391 (2012).
[12]P. Sheng, Y. Sakuraba, Y. C. Lau, S. Takahashi, S. Mitani, and M. Hayashi, Sci. Adv. **3**, e1701503 (2017).
[13]Y. Tserkovnyak, A. Brataas, and G. E. Bauer, Phys. Rev. Lett **88**, 117601 (2002).
[14]V. E. Demidov, S. Urazhdin, R. Liu, B. Divinskiy, A. Telegin, and S. O. Demokritov, Nat. Commun. **7**, 10446 (2016).
[15]Y. Fukuma, L. Wang, H. Idzuchi, S. Takahashi, S. Maekawa, and Y. Otani, Nat. Mater. **10**, 527 (2011).
[16]S. Maekawa, S. O. Valenzula, E. Saitoh, and T. Kimura, *Spin current* (Oxford University Press, Oxford, 2017), 2nd edn., Series on Semiconductor Science and Technology.
[17]A. Brataas, Y. V. Nazarov, and G. E. Bauer, Phys. Rev. Lett **84**, 2481 (2000).
[18]W. Zhang, W. Han, X. Jiang, S.-H. Yang, and S. S. P. Parkin, Nat. Phys **11**, 496 (2015).
[19]S. N. Panda, S. Majumder, A. Bhattacharyya, S. Dutta, S. Choudhury, and A. Barman, ACS Appl. Mater. Inter. **13**, 20875 (2021).
[20]H. Chudo, K. Ando, K. Saito, S. Okayasu, R. Haruki, Y. Sakuraba, H. Yasuoka, K. Takanashi, and E. Saitoh, J Appl. Phys. **109**, 073915 (2011).
[21]B. B. Singh, K. Roy, P. Gupta, T. Seki, K. Takanashi, and S. Bedanta, NPG Asia Mater. **13**, 9 (2021).
[22]K. Elphick, W. Frost, M. Samiepour, T. Kubota, K. Takanashi, H. Sukegawa, S. Mitani, and A. Hirohata, Sci. Technol. Adv. Mater. **22**, 235 (2021).
[23]T. Kubota, S. Tsunegi, M. Oogane, S. Mizukami, T. Miyazaki, H. Naganuma, and Y. Ando, Appl. Phys. Lett. **94**, 122504 (2009).
[24]H.-x. Liu, Y. Honda, T. Taira, K.-i. Matsuda, M. Arita, T. Uemura, and M. Yamamoto, Appl.

Phys. Lett. **101**, 132418 (2012).
[25]T. Seki, Y. Sakuraba, H. Arai, M. Ueda, R. Okura, H. Imamura, and K. Takanashi, Appl. Phys. Lett. **105**, 092406 (2014).
[26]T. Yamamoto, T. Seki, and K. Takanashi, Phys. Rev. B **94**, 094419 (2016).
[27]S. Picozzi, A. Continenza, and A. J. Freeman, Phys. Rev. B **66**, 094421 (2002).
[28]A. L. Kwilu, M. Oogane, H. Naganuma, M. Sahashi, and Y. Ando, J Appl. Phys. **117**, 17D140 (2015).
[29]L. Bainsla, R. Yilgin, J. Okabayashi, A. Ono, K. Suzuki, and S. Mizukami, Phys. Rev. B **96**, 094404 (2017).
[30]B. Balke, G. H. Fecher, H. C. Kandpal, C. Felser, K. Kobayashi, E. Ikenaga, J.-J. Kim, and S. Ueda, Phys. Rev. B **74**, 104405 (2006).
[31]M. Oogane, T. Kubota, Y. Kota, S. Mizukami, H. Naganuma, A. Sakuma, and Y. Ando, Appl. Phys. Lett. **96**, 252501 (2010).
[32]A. Soumyanarayanan, N. Reyren, A. Fert, and C. Panagopoulos, Nature **539**, 509 (2016).
[33]S. Panda, S. Mondal, J. Sinha, S. Choudhury, and A. Barman, Sci. Adv. **5**, eaav7200 (2019).
[34]J. M. Shaw, H. T. Nembach, and T. J. Silva, Phys. Rev. B **85**, 054412 (2012).
[35]J. Foros, G. Woltersdorf, B. Heinrich, and A. Brataas, J Appl. Phys. **97**, 10A714 (2005).
[36]J. Borge and I. V. Tokatly, Phys. Rev. B **96**, 115445 (2017).
[37]C. T. Boone, H. T. Nembach, J. M. Shaw, and T. J. Silva, J Appl. Phys. **113**, 153906 (2013).
[38]C. T. Boone, J. M. Shaw, H. T. Nembach, and T. J. Silva, J Appl. Phys. **117**, 223910 (2015).
[39]Y. T. Chen, S. Takahashi, H. Nakayama, M. Althammer, S. T. B. Goennenwein, E. Saitoh, and G. E. W. Bauer, Phys. Rev. B **87**, 144411 (2013).
[40]C.-F. Pai, Y. Ou, L. H. Vilela-Leão, D. C. Ralph, and R. A. Buhrman, Phys. Rev. B **92**, 064426 (2015).
[41]S. Pan, S. Mondal, T. Seki, K. Takanashi, and A. Barman, Phys. Rev. B **94**, 184417 (2016).
[42]S. Pan, T. Seki, K. Takanashi, and A. Barman, Phys. Rev. Appl. **7**, 064012 (2017).
[43]E. Beaurepaire, J. C. Merle, A. Daunois, and J. Y. Bigot, Phys. Rev. Lett **76**, 4250 (1996).
[44]A. Barman and J. Sinha, *Spin Dynamics and Damping in Ferromagnetic Thin Films and Nanostructures* (Springer International Publishing, 2018).
[45]H. C. Yuan *et al.*, Appl. Phys. Lett. **105**, 072413 (2014).
[46]M. R. Karim *et al.*, J Phys. Chem. C **125**, 10483 (2021).
[47]S. Pan, S. Choudhury, J. Sinha, and A. Barman, J Magn. Magn. Mater. **502**, 166545 (2020).
[48]Y. Fan *et al.*, Phys. Rev. B **89**, 094428 (2014).
[49]Y. Tserkovnyak, A. Brataas, and G. E. W. Bauer, Phys. Rev. B **66**, 224403 (2002).
[50]M. D. Kaufmann, Dissertation, 2007.
[51]H. Nakayama, K. Ando, K. Harii, T. Yoshino, R. Takahashi, Y. Kajiwara, K. Uchida, Y. Fujikawa, and E. Saitoh, Phys. Rev. B **85**, 144408 (2012).
[52]A. Azevedo, L. H. Vilela-Leão, R. L. Rodríguez-Suárez, A. F. Lacerda Santos, and S. M. Rezende, Phys. Rev. B **83**, 144402 (2011).
[53]J. C. Rojas-Sanchez *et al.*, Phys. Rev. Lett **112**, 106602 (2014).
[54]M. J. Hurben and C. E. Patton, J Appl. Phys. **83**, 4344 (1998).
[55]L. Zhu, D. C. Ralph, and R. A. Buhrman, Phys. Rev. Lett **123**, 057203 (2019).
[56]L. Liu, T. Moriyama, D. C. Ralph, and R. A. Buhrman, Phys. Rev. Lett **106**, 036601 (2011).
[57]M. Haertinger, C. H. Back, J. Lotze, M. Weiler, S. Geprägs, H. Huebl, S. T. B. Goennenwein, and G. Woltersdorf, Phys. Rev. B **92**, 054437 (2015).
[58]E. T. Papaioannou, P. Fuhrmann, M. B. Jungfleisch, T. Brächer, P. Pirro, V. Lauer, J. Lösch, and B. Hillebrands, Appl. Phys. Lett. **103**, 162401 (2013).
[59]S. Keller *et al.*, New J Phys **20**, 053002 (2018).
[60]Y. Li *et al.*, Phys. Rev. Lett. **122**, 117203 (2019).
[61]S. Akansel, A. Kumar, N. Behera, S. Husain, R. Brucas, S. Chaudhary, and P. Svedlindh,

Phys. Rev. B **97**, 134421 (2018).
[62]S. Husain, A. Kumar, V. Barwal, N. Behera, S. Akansel, P. Svedlindh, and S. Chaudhary, Phys. Rev. B **97**, 064420 (2018).
[63]S. Husain, A. Kumar, P. Kumar, A. Kumar, V. Barwal, N. Behera, S. Choudhary, P. Svedlindh, and S. Chaudhary, Phys. Rev. B **98**, 180404 (2018).
[64]A. Kumar, R. Gupta, S. Husain, N. Behera, S. Hait, S. Chaudhary, R. Brucas, and P. Svedlindh, Phys. Rev. B **100**, 214433 (2019).
[65]Y. Sasaki, S. Sugimoto, Y. K. Takahashi, and S. Kasai, Aip Adv **10**, 085311 (2020).
[66]Y. Wu, Y.-L. Zhao, Q. Xiong, X.-G. Xu, Y. Sun, S.-Q. Zhang, and Y. Jiang, Chinese Phys. B **23**, 018503 (2013).
[67]V. Kamberský, Can. J. Phys. **48**, 2906 (1970).

Chapter 6

6. Controlled Evolution of Ultrafast Demagnetization in Heusler Compound and Heavy Metal Interface

6.1 Introduction

Pulsed laser-induced ultrafast demagnetization has become a topic of immediate interest ever since its discovery in 1996 by Beaurepaire *et al.*[1] as it offers the potential realization of manipulating the magnetic order at an unprecedented speed. Thus, the intriguing phenomenon has been extensively studied in ferromagnetic transition metals[2], semiconductors[3,4], rare earth alloys[5,6] and half-metallic alloys[7] to achieve a solid understanding of the underlying mechanism associated with the ultrashort timescale[8]. In their paper, Beaurepaire *et al.*[1] proposed a simple phenomenological model, known as the three-temperature model (3TM) which presented a physical description of the phenomenon by considering the possible energy exchanges between the spin, electron and lattice baths in thermal equilibrium. Subsequently, many plausible mechanisms were put forward to describe the route of dissipation for spin angular momentum[9] to explain the dramatic decay of magnetic order within a few hundreds of femtoseconds. The majority of the proposed models such as Elliot-Yafet electron-phonon scattering[10], Coulomb exchange scattering[11], electron magnon scattering[9,12] and Stoner excitation are based on ultrafast spin-flip scatterings. Even direct laser excitation mediated[11] and electromagnetic radiation-mediated relativistic approaches[13] too adopted the spin-flip process as the sole underlying mechanism. Nevertheless, the phenomenon has also been attempted to be explained based on purely spin-dependent transport of excited hot carriers devoid of spin-flips, termed as super-diffusive spin transport[14,15]. Besides, a thermal current driven mechanism has also been put forward[16] and efforts have been made in terms of fundamental studies to achieve better control over the process in various materials[17].

However, it is imperative to extend a deeper understanding of the phenomenon in the heterostructures catering to the specific need of the modern technology-driven industry dealing with high-speed and energy-efficient devices. In recent times, ferromagnetic and heavy metal (FM/HM) based heterostructures[18,19] have emerged as one of the best choices for spintronic and spin-orbitronic device structures such as spin-orbit torque (SOT) magnetic random access memory (MRAM)[20] devices for their enormous application potential[21,22]. Cobalt-based

half-metallic Heusler compounds are ideal materials[23] to fit in this type of FM/HM structures for having low minority spin density of states[24] thereby achieving very high spin polarization and low switching current[25,26]. In addition to that, they are top-tier candidates in magnetic storage such as hard disks and various other spintronic and magnonic applications because of their small intrinsic Gilbert damping (α)[27,28]. On the other hand, Pt has long been a widely popular heavy metal (HM) candidate from a technological point of view for its lower resistivity, higher SOC strength and superior device efficiency involving FM/HM heterostructure[29]. Recently, it has been shown that the interface of the Heusler compound and Pt can offer giant spin transparency along with very high spin mixing conductivity and thus can be a crucial choice in spin current-based devices[19,30].

There have been reports on extensive studies on Heusler material focusing on the precessional dynamics conducted in the electrical and all-optical manner [31]. Reports are also available in the literature showing a correlation between the demagnetization time, Fermi level position and half-metallicity for cobalt-based Heusler alloy thin films [32,33]. However, there is a dearth of systematic studies in the literature dealing with the femtosecond and picosecond dynamics simultaneously for FM/HM heterostructure. Therefore, an extensive theoretical and experimental investigation is required for achieving a comprehensive fundamental understanding of such an interface.

Thus, the objective of the present study is to perform a systematic investigation of the ultrafast demagnetization in $Co_2Fe_{0.4}Mn_{0.6}Si$/Pt heterostructure and to understand the correlation with the precessional dynamics with an insight into the underlying microscopic nature. Here we have employed an all-optical time-resolved magneto-optical Kerr effect (TRMOKE) technique that has long been demonstrated as one of the most efficient methods to probe the spin and magnetization dynamics in the femtosecond to nanosecond temporal regime offering local, non-invasive measurement and reliable determination of demagnetization time as well as effective Gilbert damping. In this study, we present a thickness-dependent strong modification of the ultrafast demagnetization time in an engineered heterostructure interface consisting of a Heusler compound and a heavy metal which have further been correlated with the effective Gilbert damping associated with the precessional dynamics of the system. Phonon-mediated spin-flip scattering (SFS) has been considered the primary mechanism responsible for the ultrafast quenching of magnetic order which has been validated employing microscopic three-temperature (M3TM) model. Furthermore, the significant role of spin transport through the interface has also been demonstrated in ultrafast spin dynamics.

6.2 Experimental Details

6.2.1 Fabrication

Two series of heterostructures with configuration: MgO(sub)/Cr(20 nm)/CFMS(d)/Pt(t) were prepared for our investigation. For series I (S1-S6), the CFMS layer thickness was varied as d = 10, 12, 14, 16, 18, and 20 nm keeping the thickness of the Pt layer constant at t = 5 nm. For series II (S7-S12), the Pt layer thickness was systematically varied as t = 1, 2, 3, 4, 5, 8, 12 nm, maintaining a constant d = 16 nm. A 2-nm-thick protective Al layer was deposited on top of the sample stacks to prevent any external degradation such as oxidation due to atmospheric exposure, high pulse energy from femtosecond laser etc. The deposition of CFMS Heusler compound thin films was carried out at room temperature using ultra-high vacuum magnetron sputtering at a base pressure below 1×10^{-7} torr. Here, a single crystalline MgO (001) substrate was used and on top of that, a 20-nm-thick Cr was deposited to serve as the buffer layer. The deposition of CFMS was followed by in-situ annealing at 500 °C to promote the crystalline ordering of CFMS with subsequent growth of the Pt layer at room temperature to reduce the interface intermixing. The depositions were executed at a rate of 0.01 Å/s with Ar pressure of 5 millitorrs.

6.2.2 Measurements

In-situ reflection high energy electron diffraction (RHEED) images from the samples were procured to check the epitaxial growth quality of the CFMS and Pt thin films. In addition to that, *ex-situ* out-of-plane and tilted x-ray diffraction (XRD) patterns in standard θ-2θ geometry were recorded to extract the crystalline phase information as well as chemical (atomic-site) ordering. After that, the x-ray reflectivity (XRR) measurement and simulation technique are employed to confirm the actual thickness of the constituent layers. Magnetic hysteresis properties of the samples were investigated at room temperature using a vibrating sample magnetometer (VSM).

To measure the ultrafast demagnetization and fast relaxation dynamics from the samples, an all-optical time-resolved magneto-optical Kerr effect (TRMOKE) magnetometer is employed. The present set-up is a custom-built one in a non-collinear geometry that adopts a two-colour pump-probe technique to explore the magnetization dynamics at the ultrafast timescale. At first, the fundamental laser beam from an amplified femtosecond laser source (Libra, Coherent Inc.) with wavelength (λ) = 800 nm and full width at half maximum (FWHM) ≈ 40 fs was split into two parts using a 30:70 beam splitter. The weaker part of the fundamental laser beam is

utilized as a probe and the frequency-doubled stronger part of this beam (λ = 400 nm, FWHM > 40 fs) is used as a pump so as to trigger the dynamics. On the surface of the sample, the pump beam has a larger spot size (~400 μm) in comparison to that of the probe beam (~100 μm) ensuring the measurement of local dynamics from a uniformly excited area. Here, the pump beam is made to incident obliquely on the sample, while the probe beam is allowed to incident normally to measure the polar Kerr rotation from the sample using a polarized beam splitter and two separate silicon photodiodes. A variable magnetic field is applied to the sample at a small angle (~15°), the in-plane component of which (*H*) is defined as the bias magnetic field. Finally, a pair of lock-in amplifiers (SRS 830) are employed for phase-sensitive detection of Kerr rotation and reflectivity data without any mutual interference and an optical chopper modulating the pump beam at 373 Hz serves as the reference for the detection.

6.3 Results and Discussion

6.3.1 Structural and Interface Characteristics

In order to proceed with a systematic investigation it is imperative to study the structural characteristics of the series of samples as the material properties of the Heusler compounds tend to change to a great extent depending upon their crystalline phase and the chemical ordering at the atomic sites[34]. A strong XRD peak obtained from CFMS (200) confirms the formation of B2 crystalline structure whereas the intense diffraction peak arising from CFMS (400) indicates its association with cubic crystalline symmetry. The nominal thicknesses of the constituent layers have been confirmed by best-fit to the experimental XRR fringes. The magnetic hysteresis behaviour at room temperature has also been studied using VSM with an in-plane magnetic field applied along the easy axis (CFMS [110]) which shows that all the samples have very low coercive fields (~22-30 Oe) and the extracted values of saturation magnetization show a moderate reduction from its bulk counterpart (~1050 emu/cc)[35]. An *in-situ* RHEED imaging along the MgO [100] and MgO [110] direction reveals overall epitaxial relationship as:

MgO (001) || Cr (001) || CFMS (001) || Pt (001)

and, MgO [100] || Cr [110] || CFMS [110] || Pt [100].

A detailed investigation and discussion on the structural ordering, epitaxial growth, interface and magnetic properties of the similar heterostructure can be found in earlier reports[19].

6.3.2 All-optical investigation of ultrafast demagnetization and precessional dynamics

Fig. 6.1(a) shows the schematic of the sample with all the constituent layers. A typical time-resolved Kerr rotation data obtained from all-optical TRMOKE measurement is comprised of different phenomena recorded from a few fs to a few ns regime can be decomposed into three temporal regimes as shown in fig. 6.1(b). The sudden loss of magnetic order probed within hundreds of femtoseconds (regime 1) after shining an intense femtosecond laser pulse is known as ultrafast demagnetization. The system then attempts to regain its magnetic order within a few picoseconds which is known as fast relaxation (regime 2). Regime 3 essentially consists of the precessional motion of the magnetization superimposed with the slow relaxation mechanism which extends in the ns timescale. The relative change in magnetization in ultrafast timescale enables a route to faster and non-invasive optical manipulation of magnetic order. The experimental data plotted in fig. 6.1(c) has been fitted to extract the characteristic time for ultrafast demagnetization (τ_m) and fast relaxation (τ_e) employing an analytical expression as given below[2].

$$-\frac{\Delta M_z}{M_z} = \left\{ \left[\frac{A_1}{\sqrt{1+\frac{t}{\tau_0}}} - \frac{A_2\tau_e - A_1\tau_m}{\tau_e - \tau_m} e^{-\left(\frac{t}{\tau_m}\right)} - \frac{\tau_e(A_1 - A_2)}{\tau_e - \tau_m} e^{-\left(\frac{t}{\tau_e}\right)} \right] H(t) + A_3\delta(t) \right\} \otimes G(t) \quad (6.1)$$

This expression has been derived using the three-temperature thermal reservoir model (3TM) under suitable approximations. The 3TM model provides a pretty accurate phenomenological description of the ultrafast demagnetization and the subsequent fast remagnetization considering the energy exchanges taking place between the thermal baths- spin, electron and lattice interacting with one another. For the case of direct laser-induced demagnetization, the laser photon interacts with the electronic degree of freedom first and elevates it above the Fermi level, creating a population of hot electrons. The direct interaction between the laser photon and the spin reservoir is prohibited by the angular momentum selection rule[36]. This is followed by the rapid thermalization of electrons, when they interact with the spin bath causing a loss of spin phase memory, resulting in sudden quenching of the ferromagnetic order in the material. However, the spin bath then dissipates its excess energy by interacting with the lattice and environment. By doing so it relaxes back to the initial order although at a much slower pace in comparison to that of ultrafast demagnetization. Here, in equation 1, τ_0 represents the timescale associated with the electron-phonon interaction. Where the weight factor A_1 being

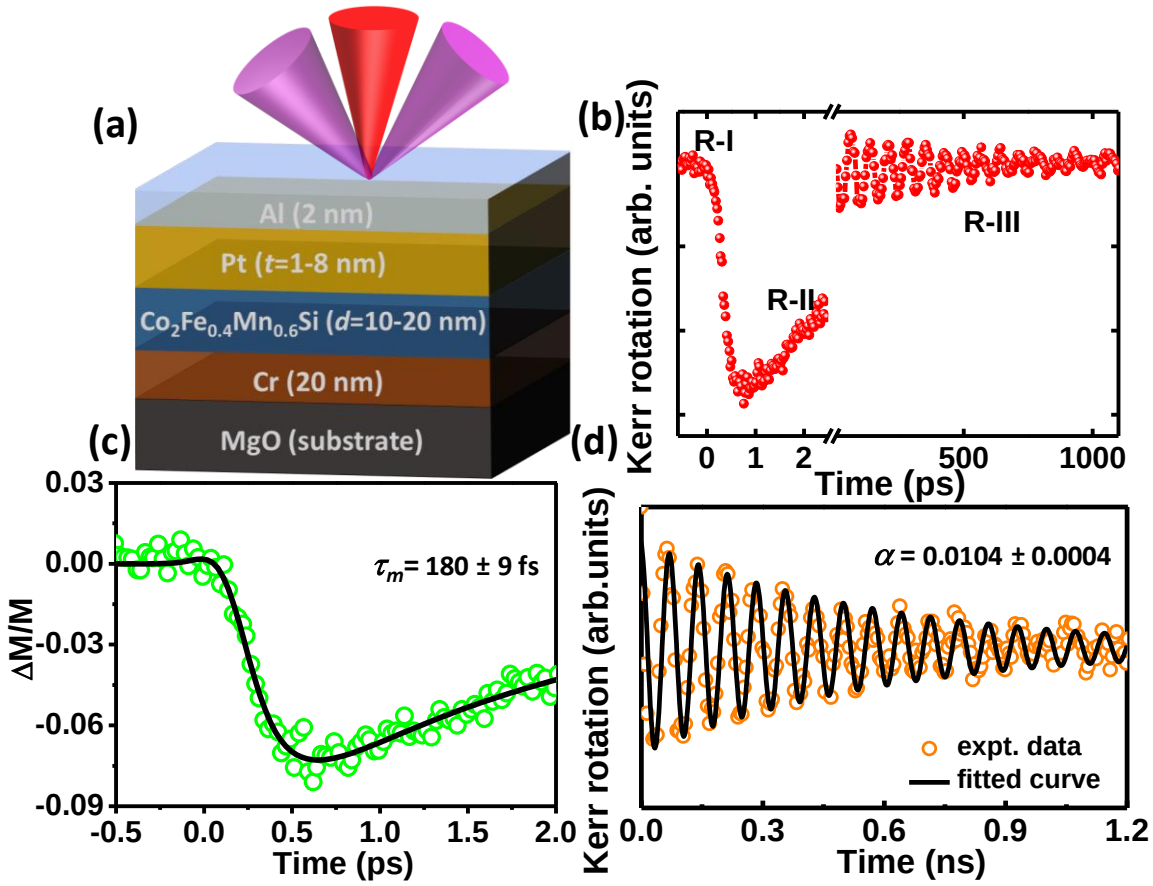

Figure 6.1: Schematic representation of the CFMS/Pt heterostructure sample with varying thickness (b) a representative TRMOKE data depicting three different temporal sections including the ultrafast demagnetization as well as precessional Kerr oscillation with a bi-exponential background. (c) Ultrafast demagnetization and fast relaxation dynamics shown upto 2 ps-green circles represent experimental data points whereas black solid line represents theoretical fit. (c) background-subtracted precessional Kerr rotation-experimental data shown in orange circles. Solid line shows decaying sinusoidal fit employed to extract characteristic decay time and effective Gilbert damping.

proportional to the magnetization after equilibrium is regained between the electron, spin and lattice subsystems, A_2 follows the rise in temperature for the electronic reservoir. The magnitude of the state filling effect occurring during the overlapping between the pump and probe $[\delta(t)]$ is represented by A_3. The function is then convoluted with a Gaussian laser pulse function, represented by $G(t)$ to arrive at the normalized change in magnetization.

In the process of electron-lattice and spin-lattice relaxation, the rapid modification in the crystalline anisotropy due to the elevated lattice temperature triggers the precessional motion of magnetization around an effective magnetic field. The precession takes place alongside the slow re-magnetization process when lattice and electronic degrees attempt to achieve thermal equilibrium with the surroundings. The precessional motion of magnetization can be parameterized by the associated Gilbert damping parameter, α and the precessional frequency,

f. In our experiment, the bi-exponential background associated with heat dissipation during the slow relaxation has been eliminated and the precessional oscillation is fitted with a decaying harmonic function to extract the characteristic decay constant (fig. 6.1(d)) which is factored in along with the effective magnetization to calculate the effective value of α. Constant values of pump and probe fluences have been maintained at 17 mJcm^{-2} and 1.5 mJcm^{-2} to avoid any significant contribution of time smearing in the analyzed values of ultrafast demagnetization time.

6.3.3 Correlation between ultrafast demagnetization and Gilbert damping

Experimental values of ultrafast demagnetization (τ_m) for the two series of samples have been extracted using the best fit from equation 1. The standard deviation in the fitted parameter has been denoted as the error bar. We have observed that τ_m is increasing monotonically with *d*, as

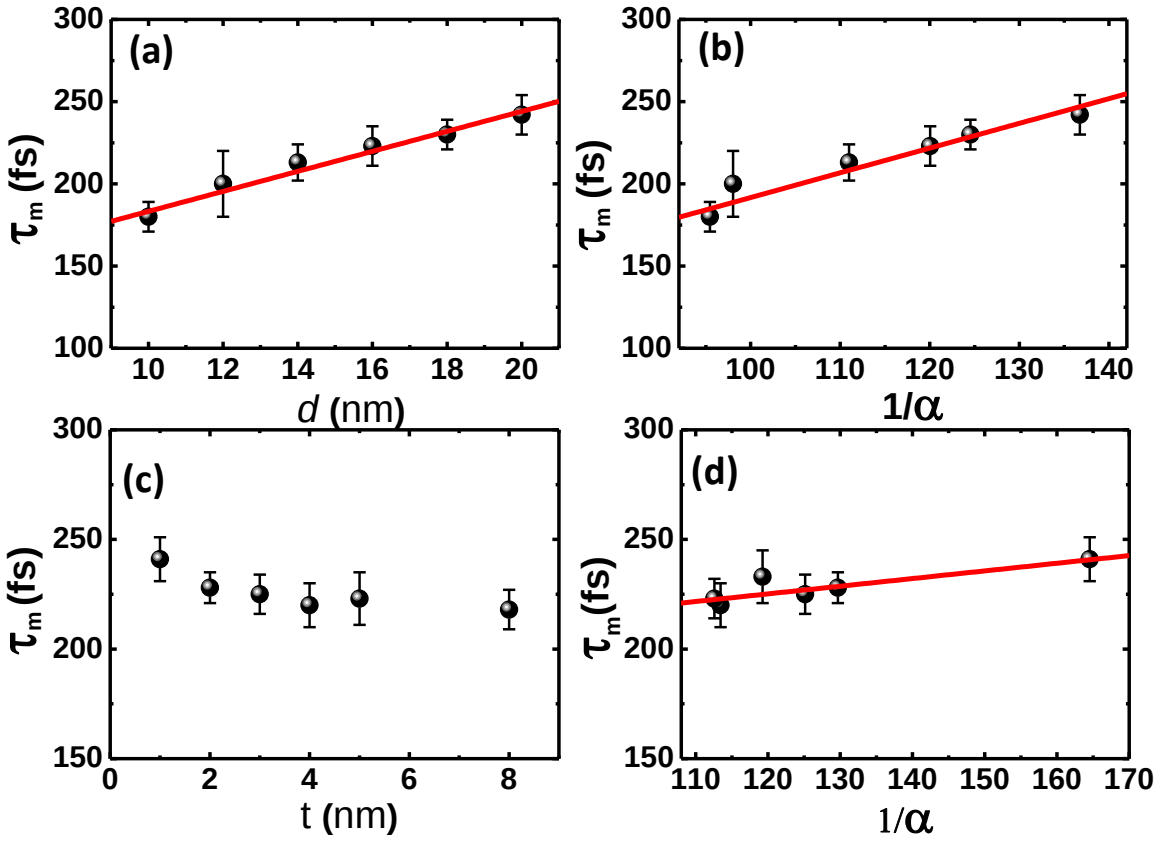

Figure 6.2: (a) Ultrafast demagnetization time (τ_m) as a function of CFMS layer thickness (*d*) with *t*= 5 nm (b) ultrafast demagnetization time (τ_m) as a function of inverse of effective Gilbert damping with varying *d,* showing an inverse correlation between τ_m and α (c) ultrafast demagnetization time (τ_m) as a function of Pt layer thickness (*t*) with *d*= 16 nm (d) ultrafast demagnetization time (τ_m) as a function of inverse of effective Gilbert damping with varying *t,* showing an inverse functional relationship between τ_m and α

shown in fig. 6.2(a) while *t* has been kept fixed at 5 nm. On the other hand, the extracted values of τ_m have been found to decrease gradually with *t*, especially in the lower *t* regime. However, with *t* > 4 nm, τ_m shows no appreciable variation with *t*, as evident from fig. 6.2(c). To explore the correlation of ultrafast demagnetization with the precessional dynamics we have subsequently potted τ_m as a function of inverse of effective damping constant, $1/\alpha$. As the value of $1/\alpha$ increases from 95.4 to 136.7, corresponding to an increase in *d* from 10 to 20 nm, the value of τ_m rapidly and monotonically increases from 180±9 fs to 242±12 fs, as depicted in fig. 6.2(b). However, τ_m increases from 218±9 fs to 241±10 fs with the value of $1/\alpha$ increasing from 112.5 to 164.5 as *t* is varied from 1 nm to 8 nm. Although, τ_m rises at a much slower pace with $1/\alpha$ associated with a variation of *t*, in comparison to that observed for a variation of *d*, we have observed a clear linear relationship between τ_m and α characterizing two largely different timescales of spin dynamics (fig. 6.2(b) and 6.2(d)).

6.3.4 Microscopic three temperature modelling

So far, we have experimentally extracted the value of τ_m and α employing an approximated expression derived from the 3TM and observed their correlation for our system. As the phenomenological 3TM only deals with the exchange of energy between different heat reservoirs, it hardly provides any information about the microscopic nature of the system or its constituting components. Therefore, to achieve a better insight into the underlying microscopic behaviour, we have further attempted modelling of the experimental data employing the microscopic three-temperature model (M3TM). This model, first proposed by Koopmans *et al.*[8,37], considers the Elliott-Yafet type spin-flip scattering interaction mediated by phonons as the main microscopic mechanism responsible for the ultrafast demagnetization and subsequent relaxation dynamics.

In M3TM, the rate equations for electron and lattice temperatures are described by:

$$C_e \frac{dT_e}{dt} = -G_{el}(T_e - T_s) + P(t) \tag{6.2}$$

$$C_l \frac{dT_l}{dt} = -G_{el}(T_l - T_e) \tag{6.3}$$

Which are modified versions of the foundation equations used in phenomenological 3TM. Here, C_e and C_l are the specific heats and T_e and T_l *are* the absolute temperatures of the electron and lattice (phonon) reservoirs, respectively. Considering a mean-field approximation to describe the spin excitation, the femtosecond magnetization dynamics is given by a modified

rate equation:

$$\frac{dm}{dt} = Rm\frac{T_p}{T_c}\left[1 - mcoth\left(m\frac{T_c}{T_e}\right)\right] \tag{6.4}$$

Here, the parameter R is a scaling factor specific to the material system under investigation with the following functional form:

$$R \propto a_{sf}\left({T_c^2}/{\mu_{at}}\right) \tag{6.5}$$

Where a_{sf} denotes the spin-flip probability associated with the Elliot-Yafet type of scattering of electron and phonon momentum. T_c refers to the Curie temperature and μ_{at} denotes the atomic magnetic moment for the system. For setting up the simulations, we chose a laser pump term of the form $P(t) = F\exp[-(t/\tau_p)^2]$ having a Gaussian temporal profile with a pulse width τ_p = 100 fs determined by the pump-probe cross-correlation and proportional to the pump fluence F. The maximum electron temperature rise and thus also the amplitude of magnetization quenching sensitively depends on the laser pump term which is therefore adjusted to reproduce the maximum quenching observed. The electronic specific heat is calculated as $C_e(T_e) = \gamma T_e$ where γ is the Sommerfeld coefficient. The value of γ for CFMS is approximated to 820 $Jm^{-3}K^{-2}$ as a weighted average of the individual γ values of Co, Fe, and Mn found in standard textbooks[38]. The lattice specific heat C_l is calculated at each value of the lattice temperature according to the Debye relation

$$C_l = 9N_A k_B\left(\frac{T}{\theta_D}\right)^3\int_0^{\frac{T}{\theta_D}}\frac{x^4e^x}{(e^x-1)^2} \tag{6.6}$$

where N_A is the Avogadro's number, k_B is the Boltzmann constant and θ_D is the Debye temperature, taken as 441 K. T_c is taken to be 985 K as reported in the literature[39] and μ_{at} to be 2.14μ_B, the weighted average of the constituent elements. Thereafter, the normalized demagnetization traces are directly fitted to equation (4) to obtain G_{el} and a_{sf} as fit parameters. While a_{sf} influences the associated timescale of the demagnetization via the scaling factor R, G_{el} influences mainly the magnetization recovery dynamics. In table 6.1 we have shown the variation of a_{sf} vs d. With t = 5 nm and d varying from 10 nm to 20 nm for samples S1 to S6, we have observed that the fitted value of a_{sf} decreased from 0.0756 to 0.0649 indicating a gradual decrease in spin-flip probability from 7.5% to 6.5%, associated with the correspondingly longer demagnetization times. On the other hand, for d= 16 nm and t varying from 1 nm to 8 nm, a weaker modulation of the demagnetization time is observed in commensurate with the extracted a_{sf}.

Table 6.1: Electron-lattice coupling constant, maximum electron temperature and the spin-flip probability extracted from M3TM

Sample	d (nm)	t (nm)	G_{el} ($\times 10^{18}$ $Js^{-1}m^{-3}K^{-1}$)	$T_{e\,max}$ (K)	a_{sf}
S1	10	5	2.0	968	.0756
S2	12	5	2.0	1161	.0735
S3	14	5	2.0	1055	.0661
S4	16	5	2.0	1080	.0658
S5	18	5	2.0	1175	.0654
S6	20	5	2.0	1029	.0649
S7	16	1	2.6	1114	.0649
S8	16	2	2.4	1297	.0655
S9	16	3	2.4	1159	.0656
S10	16	4	2.2	1115	.0658
S11	16	8	2.0	1053	.0658

So far as the microscopic behaviour of the system is concerned, phonon-mediated spin-flips and the spin current transport can be taking place at the same time. As our model takes care of the quenching of magnetization occurring because of the spin flip scattering processes alone, it will be interesting to see how the model output accounts for the overall dynamics when there can be a significant contribution of the spin current transport, which is spin conserving in nature. Fig 6.3(b) shows that the spin flip probability consistently drops with the enhancement in thickness of the CFMS layer (d), although the rate of decay becomes slightly lower in the higher d range. This decrement predicts the slower rate of quenching and higher demagnetization time observed in the higher d values as shown in the fig. 6.2(a). Here, as the observation has been made with a constant t, we expect a finite amount of spin current transport to be associated with the process. However, the spin-flip scattering remains the sole driving mechanism for the process.

Variation of spin flip scattering probability (a_{sf}) with the thickness of Pt layer (t) has been shown in the fig. 6.3(c). Here, a_{sf} grows with t in an exponential manner and is found to saturate around 0.658 when the thickness (t) is sufficiently higher than the spin diffusion length. In this case, as d remains constant over the complete range of varying t, spin-flip scattering can no longer be responsible for the change in a_{sf} with t. Thus, the demagnetization process is mainly modulated by the spin current transport process which is captured by the model despite the fact that a constant amount of spin flips is taking place. It will be interesting to note that, when the

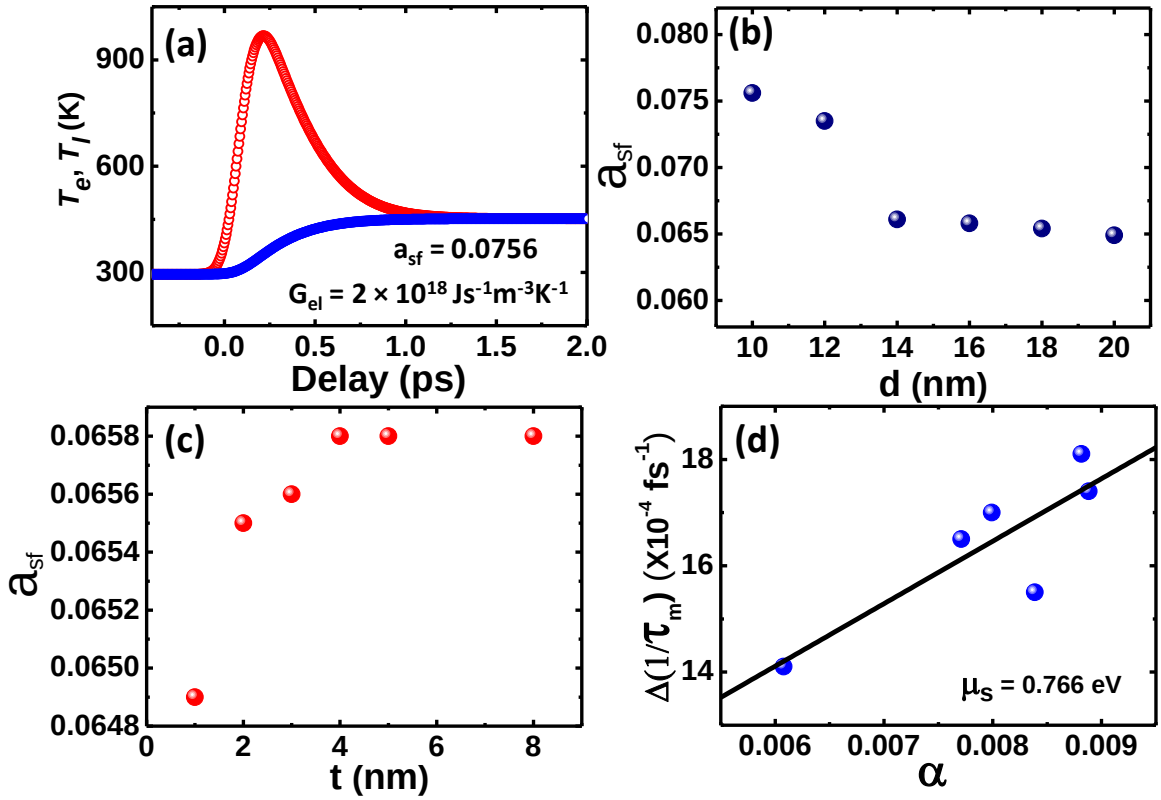

Figure 6.3: (a) Evolution of electronic and lattice temperatures during ultrafast demagnetization and fast relaxation for sample 1. (b) spin-flip probability parameter as a function of the thickness of the CFMS layer (d) (c) enhancement of spin-flip probability parameter with the thickness of the Pt layer (t) (d) Inverse of demagnetization time ($1/\tau_m$) has been plotted as a function of effective Gilbert damping (α) corresponding to the variation in Pt layer thickness (t). The solid line shows theoretical fit to extract the spin chemical potential (μ_s).

spin current transport is the driving mechanism behind the ultrafast quenching of magnetic order, the change is a_{sf} is found to be smaller as compared to the case when spin-flip scattering is the sole driver of the process. This helps us to understand the τ_m vs t behaviour observed in the experiment as shown in fig. 6.2(c).

Although the effect of spin current transport as reflected in the change in a_{sf} appears to be small, the actual effect of the interface in controlling the ultrafast demagnetization dynamics is significant. Earlier literature consisting of the investigation of CFMS thin films reported the τ_m in the range of 355-365 fs for CFMS films of 10-20 nm[31]. On the contrary, we have obtained the value of τ_m as 180±9 fs to 242±12 fs in the present study for CFMS(10)/Pt(5) and CFMS(20)/Pt(5), respectively, which shows a 49.2% and 33.7% acceleration of ultrafast demagnetization in the respective thickness range. We attribute this to the presence of Pt, a

strong spin sink material adjacent to the CFMS, promoting strong spin current transport across the interface. Therefore, it can play a vital role in the modulation of both the dynamics. Because of the strong SOC of Pt, the spins are accumulated at the interface building a significant spin chemical potential. Under the action of this strong driving force, the spin current from the CFMS layer rapidly flows to the Pt layer and gets dissipated creating a large non-local enhancement in effective Gilbert damping. The amount of spin chemical potential can be obtained from the following expression:

$$\Delta\left(\frac{1}{\tau_m}\right) = \frac{\mu_s}{\hbar}(\alpha - \alpha_0) \tag{6.7}$$

We have plotted [fig. 6.3(d)] and calculated μ_s for our system which comes out to be: 0.766 eV. Thus, along with modulating the Gilbert damping and thereby the corresponding precessional dynamics, strong spin transport through this FM/HM interface also serves as an additional avenue for the dissipation of spin angular momentum and the enduing ultrafast demagnetization.

6.4 Conclusion

In summary, we have systematically investigated pulsed laser-induced ultrafast demagnetization in CFMS (d)/Pt (t) heterostructures with varying thicknesses of CFMS and Pt layers. A large tunability of demagnetization time has been found with the variation of the CFMS thickness in the range 10 nm ≤ d ≤ 20 nm. On the contrary, it is found to vary slowly with Pt layer thickness being varied in a considerable range: 1 nm ≤ t ≤ 8 nm. The experimental findings have been found to be in good agreement with the scattering probabilities calculated employing the microscopic three-temperature model. In addition, we observed an inverse correlation between the ultrafast demagnetization time and the effective Gilbert damping. Furthermore, a significant acceleration of ultrafast demagnetization has been observed for the CFMS/Pt heterostructure in comparison to that of CFMS layers alone reported in earlier literature. This has been attributed to the spin transport phenomenon occurring at the interface under the influence of the spin chemical potential manifested mainly due to the large SOC associated with the HM layer. Therefore, strong spin current transport can provide an additional avenue for the dissipation of spins thereby facilitating a highly controllable evolution of femtosecond demagnetization. This study can open up new possibilities in FM/HM heterostructure-based high-speed spintronic device applications.

6.5 References

[1]E. Beaurepaire, J. C. Merle, A. Daunois, and J. Y. Bigot, Phys. Rev. Lett **76**, 4250 (1996).
[2]F. Dalla Longa, J. T. Kohlhepp, W. J. M. de Jonge, and B. Koopmans, Phys. Rev. B **75** (2007).
[3]J. Wang, I. Cotoros, K. M. Dani, X. Liu, J. K. Furdyna, and D. S. Chemla, Phys. Rev. Lett **98**, 217401 (2007).
[4]J. Wang, Ł. Cywiński, C. Sun, J. Kono, H. Munekata, and L. J. Sham, Phys. Rev. B **77**, 235308 (2008).
[5]V. López-Flores, N. Bergeard, V. Halté, C. Stamm, N. Pontius, M. Hehn, E. Otero, E. Beaurepaire, and C. Boeglin, Phys. Rev. B **87**, 214412 (2013).
[6]G. Ju, J. Hohlfeld, B. Bergman, R. J. van de Veerdonk, O. N. Mryasov, J. Y. Kim, X. Wu, D. Weller, and B. Koopmans, Phys. Rev. Lett. **93**, 197403 (2004).
[7]A. Mann *et al.*, Physical Review X **2**, 041008 (2012).
[8]B. Koopmans, J. J. Ruigrok, F. D. Longa, and W. J. de Jonge, Phys. Rev. Lett. **95**, 267207 (2005).
[9]S. Zhang and Z. Li, Phys. Rev. Lett. **93**, 127204 (2004).
[10]E. Carpene, E. Mancini, C. Dallera, M. Brenna, E. Puppin, and S. De Silvestri, Phys. Rev. B **78** (2008).
[11]M. Krauß, T. Roth, S. Alebrand, D. Steil, M. Cinchetti, M. Aeschlimann, and H. C. Schneider, **80**, 180407 (2009).
[12]M. Haag, C. Illg, and M. Fähnle, Phys. Rev. B **90** (2014).
[13]J. Y. Bigot, M. Vomir, and E. Beaurepaire, Nat. Phys **5**, 515 (2009).
[14]M. Battiato, K. Carva, and P. M. Oppeneer, Phys. Rev. Lett. **105**, 027203 (2010).
[15]A. Eschenlohr *et al.*, Nat Mater **12**, 332 (2013).
[16]U. Atxitia, O. Chubykalo-Fesenko, J. Walowski, A. Mann, and M. Münzenberg, Phys. Rev. B **81** (2010).
[17]G. Malinowski, F. Dalla Longa, J. H. H. Rietjens, P. V. Paluskar, R. Huijink, H. J. M. Swagten, and B. Koopmans, Nat. Phys **4**, 855 (2008).
[18]S. Panda, S. Mondal, J. Sinha, S. Choudhury, and A. Barman, Sci. Adv. **5**, eaav7200 (2019).
[19]K. Dutta, S. N. Panda, T. Seki, S. Pan, K. Takanashi, and A. Barman, Advanced Quantum Technologies **5**, 2200033 (2022).
[20]S. Zhang, Y. Su, X. Li, R. Li, W. Tian, J. Hong, and L. You, **114**, 042401 (2019).
[21]C. Chappert, A. Fert, and F. N. Van Dau, Nat Mater **6**, 813 (2007).
[22]C.-F. Pai, M.-H. Nguyen, C. Belvin, L. H. Vilela-Leão, D. Ralph, and R. J. A. P. L. Buhrman, **104**, 082407 (2014).
[23]K. Elphick, W. Frost, M. Samiepour, T. Kubota, K. Takanashi, H. Sukegawa, S. Mitani, and A. Hirohata, Sci. Technol. Adv. Mater. **22**, 235 (2021).
[24]B. Balke, G. H. Fecher, H. C. Kandpal, C. Felser, K. Kobayashi, E. Ikenaga, J.-J. Kim, and S. Ueda, Phys. Rev. B **74**, 104405 (2006).
[25]T. Seki, Y. Sakuraba, H. Arai, M. Ueda, R. Okura, H. Imamura, and K. Takanashi, Appl. Phys. Lett. **105**, 092406 (2014).
[26]T. Yamamoto, T. Seki, and K. Takanashi, Phys. Rev. B **94**, 094419 (2016).
[27]T. Kubota, S. Tsunegi, M. Oogane, S. Mizukami, T. Miyazaki, H. Naganuma, and Y. Ando, Appl. Phys. Lett. **94**, 122504 (2009).
[28]A. L. Kwilu, M. Oogane, H. Naganuma, M. Sahashi, and Y. Ando, J Appl. Phys. **117**, 17D140 (2015).
[29]A. Soumyanarayanan, N. Reyren, A. Fert, and C. Panagopoulos, Nature **539**, 509 (2016).
[30]B. B. Singh, K. Roy, P. Gupta, T. Seki, K. Takanashi, and S. Bedanta, NPG Asia Mater. **13**, 9 (2021).

[31]S. Pan, T. Seki, K. Takanashi, and A. Barman, Phys. Rev. Appl. **7**, 064012 (2017).
[32]S. Pan, T. Seki, K. Takanashi, and A. Barman, Phys. Rev. B **101** (2020).
[33]C. Guillemard *et al.*, Adv. Mater. **32**, e1908357 (2020).
[34]S. Pan, S. Mondal, T. Seki, K. Takanashi, and A. Barman, Phys. Rev. B **94**, 184417 (2016).
[35]T. Yamamoto, T. Seki, M. Kotsugi, and K. Takanashi, Appl. Phys. Lett. **108**, 152402 (2016).
[36]A. Kirilyuk, A. V. Kimel, and T. Rasing, Rev. Mod. Phys **82**, 2731 (2010).
[37]B. Koopmans, G. Malinowski, F. Dalla Longa, D. Steiauf, M. Fahnle, T. Roth, M. Cinchetti, and M. Aeschlimann, Nat Mater **9**, 259 (2010).
[38]C. Kittel and P. McEuen, *Introduction to solid state physics* (Wiley New York, 1996), Vol. 8.
[39]N. Kudo, M. Oogane, M. Tsunoda, and Y. Ando, Aip Adv **9**, 125036 (2019).

Chapter 7
7. Conclusions and Future Perspective

7.1 Conclusions

In essence, the thesis contains rigorous investigations of spin dynamics from the ferromagnetic nanostructures and heterostructures in various timescales ranging from femtosecond to nanosecond employing state-of-the-art time domain experimental techniques. RF and DC magnetron sputtering, and e-beam evaporation techniques have been utilized for the deposition of thin films and heterostructures whereas e-beam lithography has been employed to fabricate the two-dimensional ferromagnetic antidot lattice. SEM has been used to produce the electron micrograph of the nanostructure and the surface topography and the elemental composition are investigated utilizing AFM and EDX techniques respectively. In-situ RHEED has been very effective to probe the crystalline epitaxial growth of the constituting layers of the heterostructures. To understand the structural phase and crystalline ordering better, out-of-plane and tilted XRD has been carried out for the heterostructures. The thickness of the individual layers and corresponding interlayer roughness values have been investigated by employing the X-ray reflectivity (XRR) technique which is simple and non-destructive in nature. The static magnetic properties and reversal behaviour has been explored in VSM and static MOKE to extract the saturation magnetization, coercive field, magneto-crystalline anisotropy etc. For the time domain measurement of ultrafast magnetization dynamics, we have employed the time-resolved magneto-optical Kerr effect (TRMOKE) based on a two-colour pump probe in both collinear and non-collinear geometry. The findings of the experimental investigations have been aided by micromagnetic simulations carried out in OOMMF, LLG Micro and Dotmag.

We started with the investigation of precessional magnetization dynamics from the diamond antidot lattice with square and hexagonal geometry. A rich variation in the multimodal spin-wave spectra is observed with systematic variation in the strength of the applied bias field. Variation of the in-plane orientation of the applied bias field revealed the nature of the dynamic configurational anisotropy for the complex antidot systems. Strong four-fold anisotropy is obtained from the antidot with the square symmetry whereas a mixture of a strong four-fold and a weak six-fold configurational anisotropy has been demonstrated for the antidot with

hexagonal lattice symmetry. The spin wave spectra are also qualitatively reproduced using micromagnetic simulations (OOMMF). A further calculation of the spatial distribution profile for spin wave power and phase enabled us to identify the origin and nature of the modes with deeper insight. The phenomenon of mode conversion from an extended mode to a quantized or pseudo-extended mode is observed at different azimuthal angles depending upon the effect of its geometry. To understand the effect of configurational anisotropy in the manipulation of spin-wave dynamics, we also calculated the internal field profile at different orientations of the applied bias field. We have obtained a stark variation of the internal field distribution with azimuthal orientation and both the lattice symmetry and the diamond shape of the antidot basis played a significant role in this modulation. The effective tunability of the spin-wave dynamics manifested from the dynamic configurational anisotropy of diamond-shaped complex antidot lattice proves them as strong candidates for spin-based on-chip functional logic devices in future.

We have then proceeded to investigate the spin pumping in ferromagnetic/heavy metal (FM/NM) heterostructure which is a crucial interface in advanced spin-orbitronic device applications. Motivated by the exotic properties such as stable spin-polarized band structure, and low intrinsic damping of Cobalt-based Heusler compounds, CFMS has been chosen as FM material. On the other hand, Pt has been selected as the heavy metal system for its high SOC and band matching properties to create a high-quality interface. A heterostructure of CFMS and Pt with varying layer thickness has been deposited on a MgO substrate with a Cr buffer layer for reduced lattice strain employing sputtering. The spin dynamics have been measured employing the TRMOKE microscope-based technique directly at the time domain. As the flow of pure spin current from FM to adjacent NM The effective damping parameter is then extracted as the function of the layer thicknesses and careful modelling of the trend using the ballistic model and drift-diffusion based model provides spin mixing conductance and spin diffusion length which are imperative to parameterize the pure spin current transport through an interface. Finally, we employed spin hall magnetoresistance (SHM) and spin transfer torque (STT) models to extract the interfacial spin transparency and obtained a giant value of 87%. We have demonstrated that the impact of other physical processes which might be responsible for reducing the interface transparency such as spin memory loss (SML) and two-magnon scattering (TMS) are insignificant in comparison to the spin pumping process for the present heterostructure which explains the large modulation of intrinsic Gilbert damping and giant interfacial spin transparency.

In the next study, we have investigated the laser-induced ultrafast demagnetization in CFMS/Pt heterostructure. The demagnetization time is found to be highly tunable with the variation of thickness of the FM layer. However, it shows a weak dependency on Pt layer thickness. The system has been attempted to model with the microscopic three-temperature model based on spin-flip scattering. The variation of the scattering probability parameter extracted from the model is in commensuration with the experimental results. Additionally, an inverse correlation between the ultrafast demagnetization time and effective damping has been obtained for the system. Additionally, we have found an enhancement in the speed of the ultrafast demagnetization in presence of Pt with CFMS. This has been attributed to the spin current transport across the interface due to the strong SOC of Pt. In such a heterostructure, it is shown that spin current transport under strong spin chemical potential can provide an additional channel for the transfer of spin angular momentum that leads to faster demagnetization. Thus a controllable evolution of ultrafast demagnetization can be achieved by manipulating spin current transport across the interface of a suitable heterostructure which can be extremely favourable in future high-speed energy-efficient storage architectures.

7.2 Future Perspectives

Even after its advent of more than two decades ago, modern spintronics is growing at a fast pace. To cater for the need of the technology, it has spread its wings with multiple physical processes taking place at the ultrafast timescale. Thus the investigation of magnetization dynamics at this timescale holds a lot of potential in terms of both fundamental and industrial advantages. Attention must be given to various nanoscale magnetic structures and novel heterostructures interfaces depending upon their future application potential. In this thesis, we attempted to explore the effect of the complex geometry of the overall configurational anisotropy of the antidot lattice to gain considerable control over the resulting precessional dynamics. Similar antidot lattice systems can be designed with more complex geometry following Bravais and non-Bravais arrangement for achieving a comprehensive understanding of the tunability of spin-wave spectra by modulating the dynamic configurational anisotropy. An additional control over the spin dynamics may be achieved it will be allowed to interact with the surface acoustic wave by incorporating a suitable magnetostrictive substrate. Additionally, modulation of spin dynamics in the family of complex nanostructures in contact with a heavy metal layer would be one of the crucial directions for further studies. Considering

so many attractive properties of Heusler alloys and superior spin transport properties across the interface that we explored in this thesis, it will also be interesting to study the spin dynamics of the complex magnonic crystals patterned on the CFMS/Pt heterostructure.

We have already discussed that the FM/NM family of heterostructures give us a vast playground for harnessing the pure spin current and manipulation of ultrafast magnetization dynamics via spin transport. However, a wide variety of fundamental issues needs to be addressed to gain a solid foundation over the phenomena at this timescale to realize their commercial implementation.

We have explored large modulation of intrinsic Gilbert damping by spin current transport because of the spin angular momentum pumped out from the FM layer. It will be interesting to investigate the process at low temperatures as various electronic noises may reduce at the low temperature thereby spin transport at the interface. For ultrafast demagnetization, we explored the possibility that both spin-flip scattering and spin transport can co-exist and significantly contribute to controlling the overall dynamics. Nevertheless, complete isolation of both of the phenomena seems to be challenging and would definitely be a way to look forward. In addition, the heterostructures can be designed in such a way that a comparative study between the laser-induced ultrafast demagnetization and demagnetization caused by the non-equilibrium hot electron transport from the NM layer can be carried out in order to understand the role of spin transport better. Another interesting observation would be the investigation of speed of ultrafast demagnetization with the variation of the wavelength of the pump photon. As the penetration depth of the pump changes significantly with its wavelength, it will alter the distribution of non-equilibrium electrons in the NM medium which are responsible to initiate demagnetization of the adjacent FM medium. Therefore, a significant tunability in the efficiency of ultrafast demagnetization might be observed. Recently, optical inter-site spin transfer (OISTR) has been demonstrated to be effective to reduce the ultrafast demagnetization time in the order of 10-20 fs. This phenomenon needs to be studied extensively in various multi-sub-lattice systems to gain further understanding. Additionally, with the rise of magnetism in two-dimensional layered Vander Waal systems such as CrI_3, Fe_5GeTe_2 etc. in presence of a strong SOC medium they can also serve as novel yet challenging systems to study ultrafast magnetization dynamics and may provide a novel perspective to the field in near future.

8. Appendix A: Chapter 4

8.1 Static Magneto-Optical Kerr Effect Measurement of Permalloy film

In Fig. 8.1 (a) magnetic hysteresis loop of a Py(20 nm)/Al_2O_3(3 nm) film deposited under same conditions to that of DADL sample is measured using a static magneto-optical Kerr effect (MOKE) magnetometer. The normalized magnetization (Kerr rotation) vs. applied magnetic

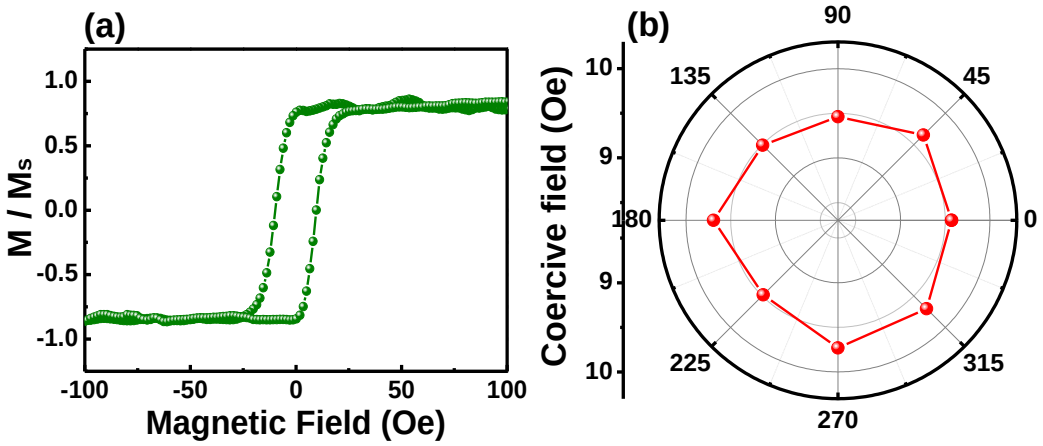

Figure 8.1: (a) Normalized magnetization-Magnetic field plot showing hysteresis behaviour of Permalloy film (b) Coercive field as a function of azimuthal angle of applied magnetic field for Permalloy film.

field in Fig. 8.1(a) shows that the Py film has a low coercive field (9.5 Oe) and no significant shift along the magnetic field axis. The latter confirms that the Py film contains no exchange bias effect due to possible surface oxidation. We have further measured the static MOKE loops at different azimuthal angles (φ) of the in-plane magnetic field. The plot of extracted coercive field vs. φ is shown in fig. 8.1 (b), which confirms negligible in-plane magneto-crystalline anisotropy in the Py(20 nm)/Al_2O_3(3 nm) film.

8.2 Micromagnetic Simulations by Introducing Edge Roughness

In order to understand the effects of edge roughness and deformations we have performed test simulations on the square and the hexagonal lattice introducing the precise edge profiles of the basis antidots as obtained from the scanning electron micrographs while keeping all other simulation parameters unchanged. However, the simulated spectra reveal that introduction of real edge profiles does not cause any significant modification in the spin-wave dynamics. Typical such simulated spin-wave spectra at $\varphi = 0°$ and 45° for square and hexagonal DADLs

are shown in fig. 8.2(a). The corresponding power and phase profiles of the spin-wave modes are shown in fig. 8.2(b). In both these DADLs, we have obtained three prominent spin-wave modes at $\varphi = 0°$ and two modes at $\varphi = 45°$.

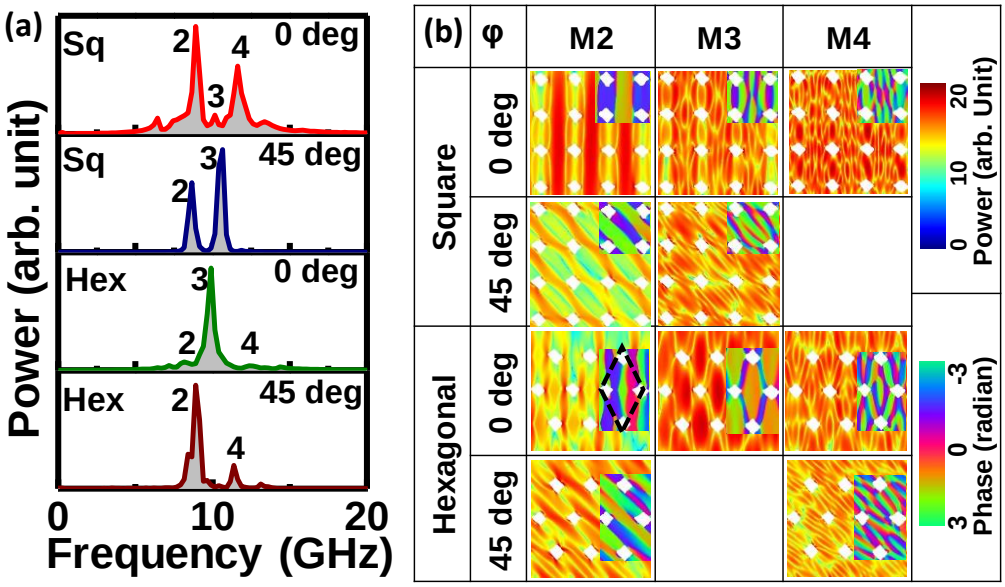

Figure 8.2: (a) Simulated spin-wave spectra of the DADLs arranged in square and hexagonal lattices after introducing edge roughness mimicked from the SEM images at $\varphi = 0°$ and 45°. (b) Corresponding power-phase profiles of the spin-wave modes. The colour maps for power and phase profiles are shown at the right side of the figure.

For the square lattice, at $\varphi = 0°$, M2 shows an extended nature through the Py channel in the y-direction. However, it converts into a pseudo-extended mode at $\varphi = 45°$. M3 is a quantized mode at both the angles $\varphi = 0°$ and 45° with n =5. M4 only shows its existence at $\varphi = 0°$ with higher quantization number (n =7). On the other hand, M2 in the hexagonal lattice is an edge-mediated extended mode in the vertical channel but showing a BV-like quantization in the x-direction with n =3 at $\varphi = 0°$, which also displays pseudo-extended behaviour at $\varphi = 45°$. At $\varphi = 0°$, M3 is a quantized mode with n = 3 and. M4 is also a quantized mode with n = 5 for both $\varphi = 0°$ and 45°.

8.3 Simulated Internal Magnetostatic Field Profiles for 3 × 3 Arrays

In Fig. 4.6(c) of the thesis, we have shown the simulated internal magnetostatic field profiles around a single diamond antidot extracted from a larger array for the sake of visual clarity. Here, we present the contour plots of the same for the 3 × 3 arrays of square and hexagonal DADLs in fig. 8.3. For the square lattice at $\varphi = 0°$, the field lines are only concentrated around the sharp corners of the antidots. However, a strong nearest neighbour interaction with dense

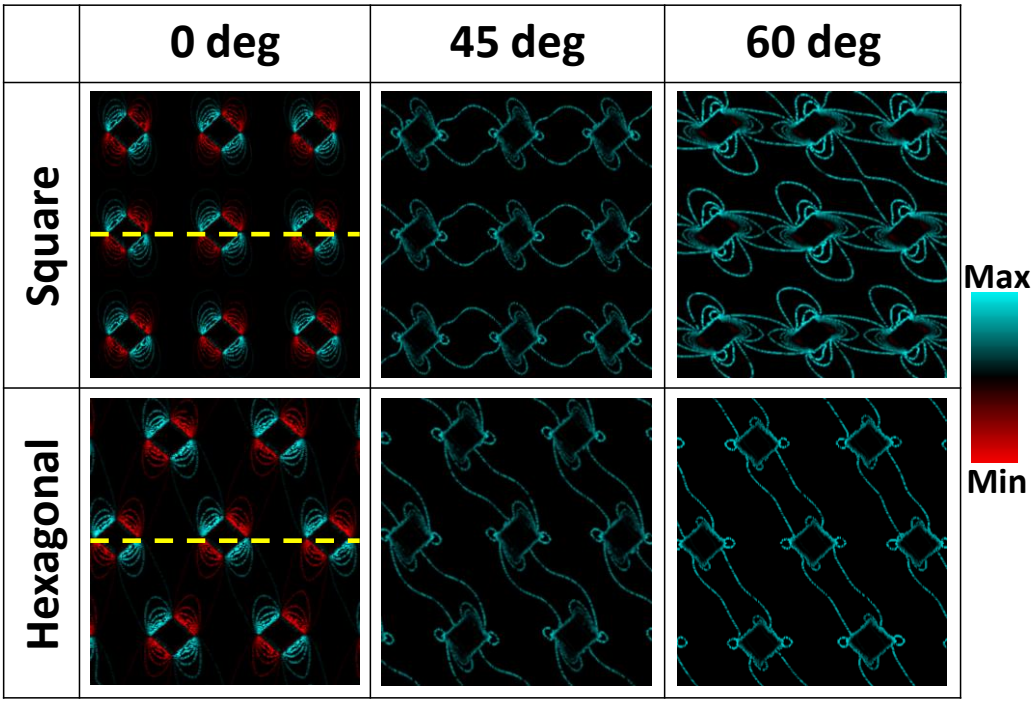

Figure 8.3: Variation of strength of internal magnetostatic field for (a) square & (b) hexagonal DADL. (c) Internal magnetostatic field distribution at different azimuthal orientation of bias field. The colour map for internal field is shown at the right side of the figure.

internal field lines is observed for this lattice along the x-direction for both $\varphi = 45°$ and 60°. On the other hand, for the hexagonal lattice, a weak nearest neighbour interaction is observed along the diagonal direction at $\varphi = 0°$, which enhances at $\varphi = 45°$ and 60°, confirming the presence of the diagonal channel for the hexagonal lattice.

9. Appendix B: Chapter 5

9.1 Extraction of fractional change in Pt lattice constant from X-ray diffraction

To gain insight about the degree of strain relaxation for different samples, we have calculated the lattice constant of the platinum from the position of Pt (100) peak using Bragg's law. The fractional changes of the lattice parameter from its natural value (0.392 nm) which can be regarded as a qualitative metric to understand the lattice microstrain, is plotted as a function of both the CFMS and Pt layer thicknesses.

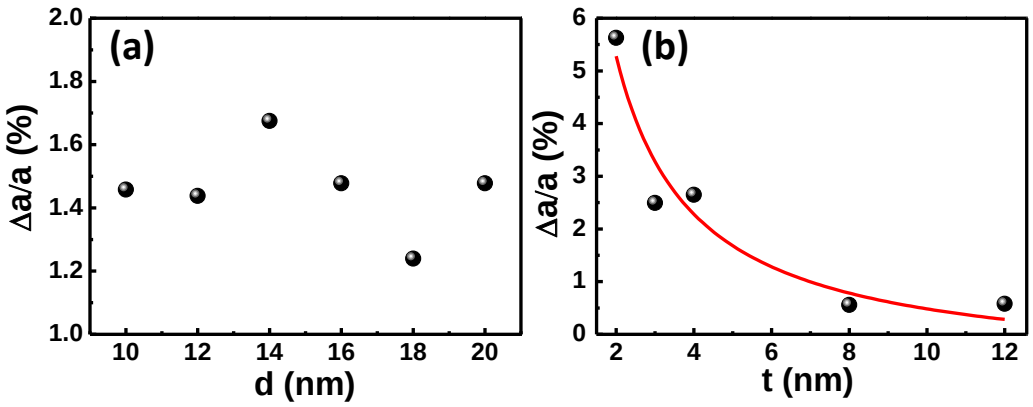

Figure 9.1: Fractional change in the lattice constant of Pt which is related to the lattice microstrain plotted as a function of (a) CFMS layer thickness and (b) Platinum layer thickness.

With enhancement of CFMS layer thickness from 10 nm to 20 nm, no significant change is observed in the fractional misfit. However, this value decreases from 5.62% to 0.57% with Pt layer thickness increasing from 2 nm to 12 nm showing a (1/t) dependence of strain. Therefore, a mild strain relaxation effect is expected in samples with higher Pt thickness. However, as we have obtained very sharp streak lines in the RHEED images, the dislocation density at the interfaces will not be significant to introduce high degree of strain relaxation.

9.2 Extraction of thickness and interfacial roughness values from X-ray reflectivity measurement

In the heterostructure, along with the total surface roughness, roughness for each constituting layer becomes important factor in altering the nature of spin transport across the layers. A large interlayer roughness between the FM and HM layer might hinder the spin angular momentum transfer and eventually lower the interfacial spin transparency. X-ray reflectivity (XRR) can be

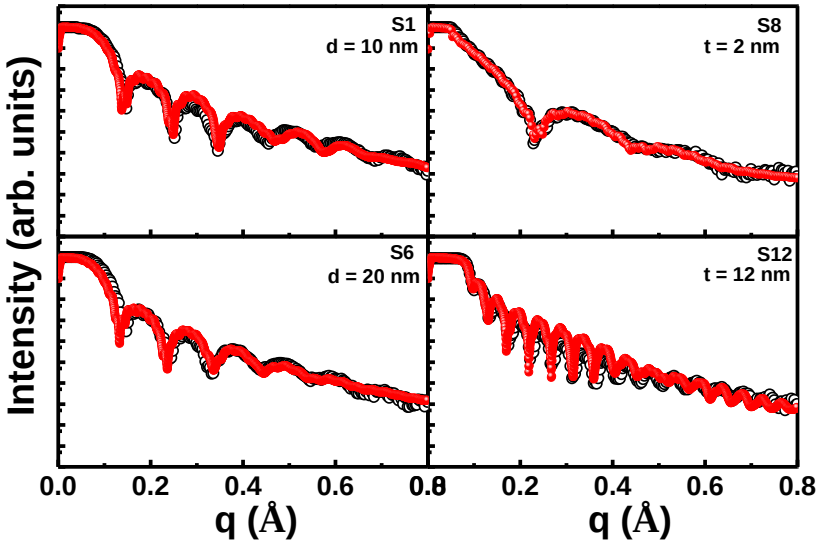

Figure 9.2: Normalized intensity vs q plot showing the Kiessig oscillations obtained from XRR measurement for sample S1, S6, S8 and S12. Black hollow spheres represents the experimental data points where red solid spheres denote the simulated points.

a very effective non-destructive tool to measure the thickness and roughness of the individual layers. Here we have performed XRR measurement for the CFMS/Pt heterostructures and the normalized intensity vs qz data is reproduced in simulation using MATLAB based program "Reflex" [G. Vignaud, & A. Gibaud, *J. Appl. Cryst*. **52**, 201 (2019)] to extract the inter-layer roughness information. In fig. 9.2, we show some representative Kiessig fringes from the samples S1, S6, S8 and S12 and the extracted roughness parameters for the CFMS, Pt and the capping layer have been listed in the table 9.1. We have observed that the thickness values

Table 9.1: Interfacial roughness values for individual layers extracted from XRR

Sample	σ (nm) for Cr buffer layer	σ (nm) for CFMS layer	σ (nm) for Pt layer	σ (nm) for Al layer
S1	0.60	0.21	0.39	0.30
S2	0.30	0.40	0.36	0.60
S3	0.50	0.28	0.44	0.60
S4	0.30	0.22	0.45	2.10
S5	0.59	0.33	0.53	0.50
S6	0.30	0.21	0.45	0.60
S7	0.29	0.39	0.33	0.69
S8	0.33	0.27	0.47	0.68
S9	0.42	0.31	0.48	0.48
S10	0.22	0.21	0.35	0.38
S11	0.30	0.32	0.45	0.35
S12	0.20	0.29	0.45	0.26

obtained from simulation are very close to the nominal thickness values for CFMS and Pt layers. However, from the table 9.1 we see that CFMS layers have an average roughness value~0.28 nm whereas average roughness values estimated for Pt layer is ~0.39 nm. The small inter-layer roughness promotes the spin transport lowers the interfacial effects like two-magnon scattering.

9.3 Extraction of different anisotropy contributions from field dependent precessional dynamics

The Kittel formula is employed to extract the effective magnetization from the field dependence of the precessional dynamics. Here θ_H and θ_M are angles made by the effective magnetic field and magnetization with the easy axis of magnetization which is in the direction of CFMS [110] axis. In the epitaxial relationship we have discussed that the CFMS (110) and MgO (100) crystallographic planes are parallel to each other which means CFMS unit cell makes an azimuthal angle of 45° with MgO unit cell i.e. easy axis lies along the diagonal of sample substrate. In the experiment, we applied the magnetic field along the plane of the sample with slight tilt in order to induce precession. The change in the θ_M due to this configuration has been assumed negligible in the fitting. Additionally, following the easy axis of cubic anisotropy (along CFMS [110] direction) and the applied field orientation, we have considered θ_H to be 45±1°. The extracted values of the in-plane uniaxial (*K2*), bi-axial (*K4*) and the out of plane anisotropy (*Kz*) constants are presented in the table-ST3. We observed a strong four-fold anisotropy mixed with a comparatively weaker uniaxial and out-of-plane anisotropy signatures

Table 9.2: Extracted values of the in-plane uniaxial (*K2*), bi-axial (*K4*) and the out of plane anisotropy (*Kz*) constants from the Kittel fit

Sample	*K2* (erg/cm^3)	*K4* (erg/cm^3)	*Kz* (erg/cm^3)
S1	1.62×10^4	-1.00×10^5	3.65×10^4
S2	1.86×10^4	-2.47×10^5	5.69×10^4
S3	3.50×10^4	-1.81×10^6	4.84×10^4
S4	4.59×10^4	-9.75×10^4	1.61×10^4
S5	5.36×10^4	-2.35×10^5	1.08×10^4
S6	3.27×10^4	-5.15×10^5	3.53×10^4
S7	5.91×10^4	-6.51×10^5	1.90×10^4
S8	2.29×10^4	-4.44×10^5	5.42×10^4
S9	3.81×10^4	-7.32×10^4	4.23×10^4
S10	2.50×10^4	-1.77×10^5	2.61×10^4
S11	1.60×10^4	-2.30×10^5	2.23×10^4
S12	5.30×10^4	-9.56×10^5	3.53×10^4